Summer 2011

Receiver function studies of crustal structure, composition, and evolution beneath the Afar Depression, Ethiopia

Sattam A. Almadani

Department: Geosciences and Geological and Petroleum Engineering

RECEIVER FUNCTION STUDIES OF CRUSTAL STRUCTURE, COMPOSITION, AND EVOLUTION BENEATH THE AFAR DEPRESSION, ETHIOPIA

by

SATTAM ABDULKAREEM ALMADANI

A DISSERTATION

Presented to the Faculty of the Graduate School of the

MISSOURI UNIVERSITY OF SCIENCE AND TECHNOLOGY

In Partial Fulfillment of the Requirements for the Degree

DOCTOR OF PHILOSOPHY

in

GEOLOGY AND GEOPHYSICS

2011

Approved by

Dr. Stephen Gao (Co-Advisor)

Dr. Kelly Liu (Co-Advisor)

Dr. Mohamed Abdelsalam

Dr. Leslie Gertsch

Father: What you wished for becomes true.

ABSTRACT

The dissertation utilizes a set of sophisticated computer programs developed at the Geophysics group at Missouri S&T to characterize crustal properties beneath the Afar Depression in Ethiopia where extensional tectonics dominates. In this study, measurements of crustal thickness (H), crustal mean V_p/V_s [which is related to Poisson's ratio (σ)], and the sharpness of the Moho (R) were determined using teleseismic data from 18 broadband seismic sensors that we deployed along a profile of 250 km long with a station spacing of ~ 10 km. The stations had been recording continuously for an entire year from December 2009 until December 2010. The measurements were determined by stacking P-to-S converted waves (PmS) and their multiples (PPmS and PSmS). Results suggest that the average crustal thickness beneath the Afar Depression is about 28.56±0.28 km and the crust is characterized by large V_p/V_s of 1.93±0.017 and smaller-than-normal overall stacking amplitude of the P-to-S converted phases beneath most stations. Our results suggest that the crust beneath the entire study area is significantly thinned and extensively intruded by mafic dikes, representing a transitional stage between continental and ocean crust. The Tendaho Graben has the thinnest and most mafic crust, which is also supported by the observation of gravity data which suggest that the active magmatic areas are characterized by higher gravity anomalies while the thicker crusts have smaller and negative anomalies. Thus, the crust beneath the center of the Tendaho Graben is likely to be oceanic-type, and becomes progressively more continental away from the center.

ACKNOWLEDGEMENTS

I would like to express my appreciation and thankfulness to Professor Steve Gao and Professor Kelly Liu for their extended support, guidance, advice and great help throughout the period of this study. Without their assistance, I would not be able to complete my research. Also, I would like to thank Professor Mohamed Abdelsalam and Dr. Leslie Gertsch for their encouragement and valuable discussions. My ultimate, and most heartfelt, acknowledgment goes to my wife Noha. She makes my journey during my study into a dream come true.

TABLE OF CONTENTS

Page

LIST OF ILLUSTRATIONS

LIST OF TABLES

LIST OF SYMBOLS

Symbol	Description
V_p	Primary wave (compressional wave)
V_s	Secondary wave (shear wave)
Φ	The ratio between V_p and V_s ($\Phi=V_p/V_s$)
σ	Poisson's ratio ($\sigma=0.5[1-1/(\Phi^2-1)]$)
H	Crustal thickness
R	The amplitude of the converted Moho sharpness
RFs	Receiver functions
R-R-R	Rift-Rift-Rift
Hz	Hertz
Ma	Million years
PmS	Direct converted phase
PPmS & PSmS	Crustal reverberations (multiples phases)
M	Magnitude
$V_{p(z)}$	Reference crustal velocity
p	P-wave ray parameter
$t_1^{(i,j)}$	Moveout of PmS
$t_2^{(i,j)}$	Moveout of PPmS
$t_3^{(i,j)}$	Moveout of PSmS
$t_3^{(i,j)}$	Moveout of PSmS
w_1, w_2, and w_3	Weighting factors

1. INTRODUCTION

Seismological observations have offered valuable information to our understanding of the nature of the Earth's crust and of the processes by which it evolved. In particular, studying the variation in crustal thickness and other characteristics such as crustal Poisson's ratio and the sharpness of the Moho provides important clues to the geologic and tectonic processes that have been dominant in the region [Zhu and Kanamori, 2000; Gao et al., 2004; Al-Damegh et al., 2005; Nair et al., 2006; Liu and Gao, 2010]. Although the understanding of the structure of the crust has been improved significantly over the last decade, the origin and evolution of the Earth's crust remain an unsettled topic among scholars [Storey et al., 1995; Windley, 1995; Kearey and Vine, 1996; Moores, 1998; Rudnick, 1995; Kerrich and Polat, 2006; Kearey et al., 2009].

One of the most widely-used techniques to determine and understand crustal structure and evolution on a regional scale is receiver function analysis. A receiver function (RF) is a time series that isolates the response of the earth's structure near the receiver [Burdick and Langston, 1977; Langston, 1977; Owens et al., 1984; Ammon, 1990]. It is routinely used to obtain detailed layered structures of the crust and mantle. A typical RF is the result of deconvolving the vertical component from the radial component for a given event [Langston, 1979; Ammon, 1990; Sheehan et al., 1995]. The radial component of a receiver function is an important source for determining earth structure under isolated receivers [Ammon, 1990].

This study represents the latest attempt in the understanding of crustal evolution and composition beneath the Afar Depression by determining the crustal thickness (H), Poisson's ratio (σ) and the amplitude of the converted phases from the Moho (R), which is a measure of Moho sharpness. The measurements were obtained by taking advantage of a robust suite of computer programs developed at the Geophysical group at Missouri S&T [Gao et al., 2002; Liu et al., 2003; Gao et al., 2004; Liu and Gao, 2006; Nair et al., 2006; Liu and Gao, 2010]. Thousands of receiver functions were computed and visually checked and were used to measure H, V_p/V_s, and R. The Poisson's ratio (σ) was calculated using the formula $\sigma=0.5[1-1/(\Phi^2-1)]$, where Φ is the P and S wave velocity ratio [Tarkov and Vavakin, 1982; Christensen, 1996; Chevrot and van der Hilst, 2003]. The bootstrap method [Efron and Tibshirani, 1986; Press et al., 1992] was used to estimate the standard deviations of the resulting parameters.

The Afar Depression represents the only emerged R-R-R triple junction in the world other than Iceland [McKenzie et al., 1970]. It is located at the junction of two propagating oceanic ridges (Gulf of Aden and Red Sea) and a continental rift (Main Ethiopian Rift), where plate separation and magmatic activity occur [Laughton, 1966; Gass and Gibson, 1969; Roberts, 1969]. In addition, some previous studies suggested that the Afar Depression is the site where a transitional stage from continental rifting to seafloor spreading takes place [Barberi and Varet, 1977; Varet, 1978; Schilling et al., 1992; Hoffman et al., 1997]. The combination of these features makes the Afar region one of the most tectonically significant settings on Earth for the

understanding of continental rifting and transition from continental to oceanic crust.

Continental rifts and passive margins have strong effects on modifying the shape of the Earth's surface. Understanding the mechanism of rift formation has been always an on-going debate among scientists [Milanovisky and Nikishin, 1984; McMullen and Mohraz, 1989; Zorin and Lepina, 1989; Buck, 2004; Lv et al., 2010; Lu et al., 2011]. The effect of the lithospheric structure on rifting has been highlighted by models of continental rift. The most accepted explanation is due to the uplifted heat flow coming from the mantle to the surface through flood basalt [Morgan, 1983; Liang-Ping et al., 1985; Poort and Polyansky, 2002; Anderson, 2005]. Ebinger [2005] has discussed that the relationship between the lithosphere and the asthenosphere in shaping the rift systems through magmatism. Furthermore, Buck [2004] noted the importance of magmatism in rift initiation by diking events in the Afar Depression. He assumed that magma has been intruded at the rift center where the lithosphere is the thinnest.

The nature of the crust and mantle beneath Afar has been a subject of controversy for decades [Berckhemer et al., 1975; Barberi and Varet, 1977; Vart, 1978; Makris and Ginzburg, 1987; Mammo, 2004, Dugda and Nyblade, 2006]. One group of researchers proposed that Afar represents a thin oceanic-type crust [Varet, 1973; Barberi and Varet, 1977]. A second group argued that the rift is in the proto-oceanic stages and does not represent typical oceanic crust since older continental rocks are found there [Vellutini, 1990]. A third group of researchers argued that it is simply a thin continental

crust due to the upwelling of hot material arriving from the upper-mantle beneath the Afar Depression [Berckhemer et al., 1975; Makris and Ginzburg, 1987; Dugda and Nyblade, 2006]. This study reports new estimates of crustal thickness, Poisson's ratio (σ), and the amplitude of the *P*-to-*S* converted waves from of the Moho (R) in order to examine the nature and origin of the crust in the Afar Depression using teleseismic data from 18 broadband seismic stations that we deployed along a 250 km profile.

2. GEOLOGICAL SETTING

2.1 REGIONAL TECTONICS

The Afar Depression (AD) has the shape of a triangle and covers an area of ~ 200,000 km^2 (Figure 2.1) [Beyene and Abdelsalam, 2005] and is a part of the Afro-Arabian rift system [Girdler, 1991; Prodehl et al., 1997]. The depression is located at the northeast side of Africa between 10^o to 15^oN and 40^o to 43^oE [Mammo, 2004]. The Afar Depression is one of two locations (the other being Iceland) where a rift-rift-rift triple junction found [McKenzie and Morgan, 1969]. The region is located at the junction of two propagating oceanic ridges (Gulf of Aden and Red Sea) and a continental rift (Main Ethiopian Rift). It is surrounded by the Ali-Sabieh and Danakil Blocks on the east and northeastern sides and by the Nubian and Somalian plates on the south and the northeastern sides. It is commonly believed that AD represents a transitional stage from continental rifting to seafloor spreading [Barberi et al., 1972; Berckhemer et al., 1975; Hayward and Ebinger, 1996], and that the undergoing interactions between the Red Sea and Gulf of Aden rifts are responsible for the deformation pattern within the Afar Depression [Mohr, 1972; Tapponier et al., 1990; Manighetti et al., 2001].

2.2 GEOLOGY OF THE AFAR DEPRESSION

Surface rocks of the Afar Depression can be divided into four groups (Figure 2.2): (1) Pre-rift assemblage consisting of Neoproterozoic crystalline rocks, Mesozoic sedimentary rocks, and pre-Miocene volcanic and igneous rocks (2) Miocene igneous rocks covering the Mesozoic sedimentary rocks (3) Pliocene - Quaternary volcanic rocks covering most of the region and (4)

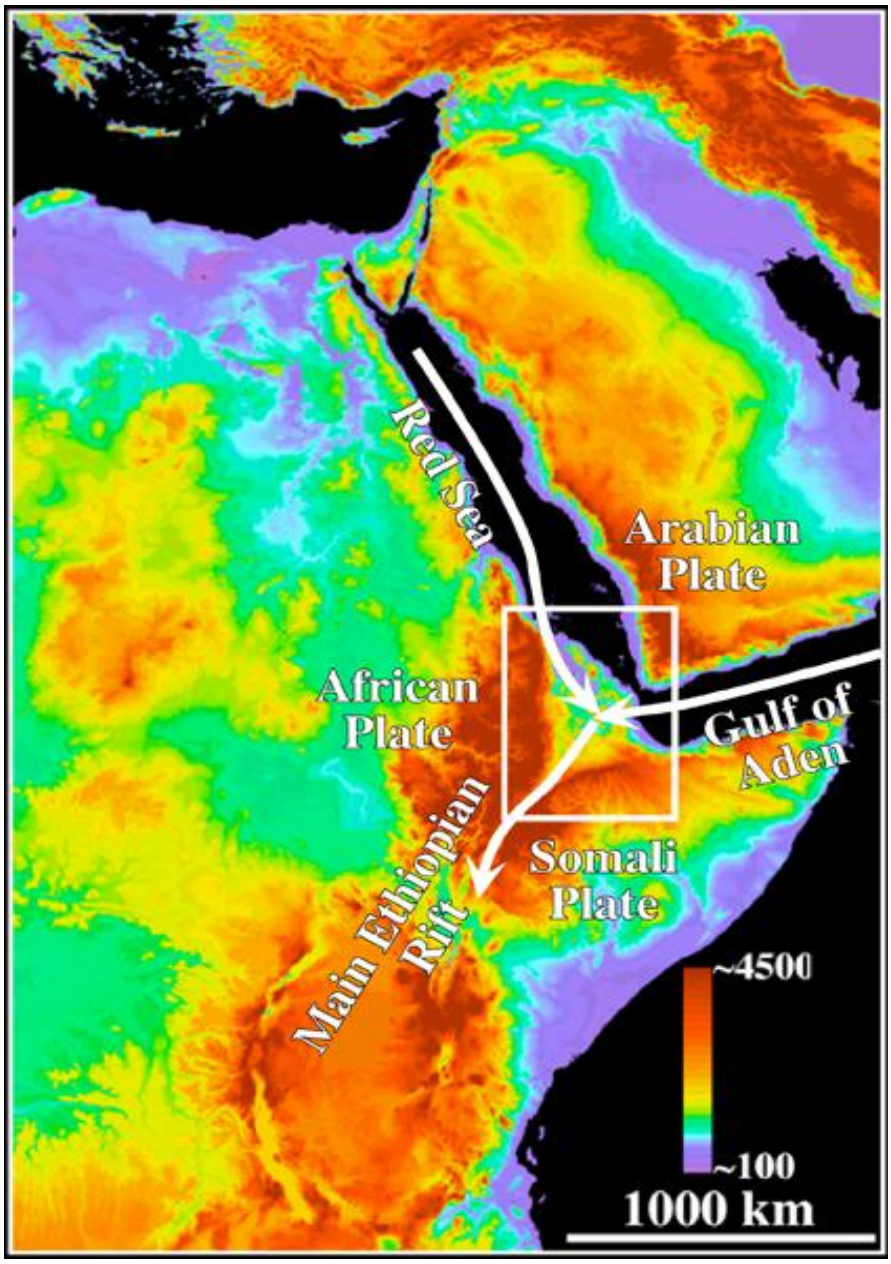

Figure 2.1. Map of the Afar Depression showing the three main rifts [after Beyene and Abdelsalam, 2005]

Quaternary volcanic and sedimentary rocks [Barberi and Varet, 1977; Varet, 1978; Tefera et al., 1996; Acton et al., 2000; Beyene and Abdelsalam, 2005; Mazzarini, 2007]. The oldest volcanic rocks (>4 Ma) crop out in the Ali-Sabieh block and south of the Danakil block [Barberi and Varet, 1977; Audin et al., 2004]. Afar is floored by dominantly basaltic volcanic rocks that are related to rifting [Pilger and Rösler, 1975]. The oldest Miocene igneous rocks consist of deeply weathered and intensely faulted flood basalts occurring around the Gulf of Tajura and Ali - Sabieh Blocks [Varet, 1978; Vellutini, 1990; Beyene and Abdelsalam, 2005]. Afar was covered by a thick sequence of flood basalts (Afar Stratoid Series) during Pliocene and Pleistocene (~ 2.4-0.8 Ma) [Barberi et al, 1972; Barberi et al., 1975; Christiansen et al., 1975; CNR-CNRS, 1975; Varet, 1978; Courtillot et al., 1984].

2.2.1 Northern Afar. The northern Afar, well-known as the Danakil Depression (Figure 2.3), is a province with low altitude. The region turns out to be narrower towards the Gulf of Zula and dominated by NNW-trending structure [Beyene and Abdelsalam, 2005]. To the south, the region joins with the southwestern and east-central Afar. Gibson et al. [1970] linked the volcanic activity in the region to the NNW fracture pattern. Redfiled et al. [2003] said that the Danakil Depression represents an area of extremely weak crust. At Dallol, the central part of the region, the elevation goes down to -120 m below sea level [CNR-CNRS, 1973]. The Quaternary volcanic rocks in the region are characterized by shield volcanoes [Beyene and Abdelsalam, 2005].

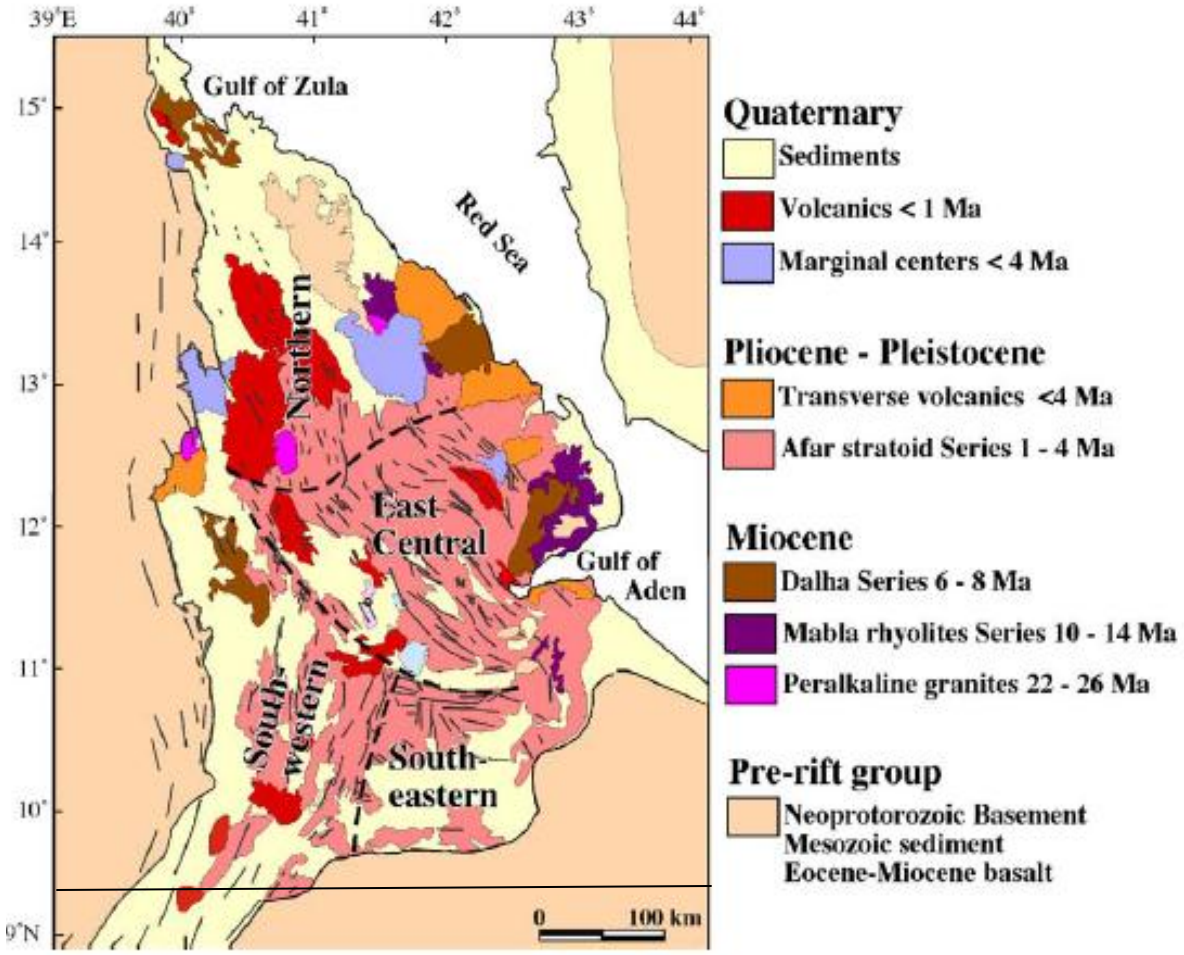

Figure 2.2. Geological map of the Afar Depression [after Beyene and Abdelsalam, 2005]

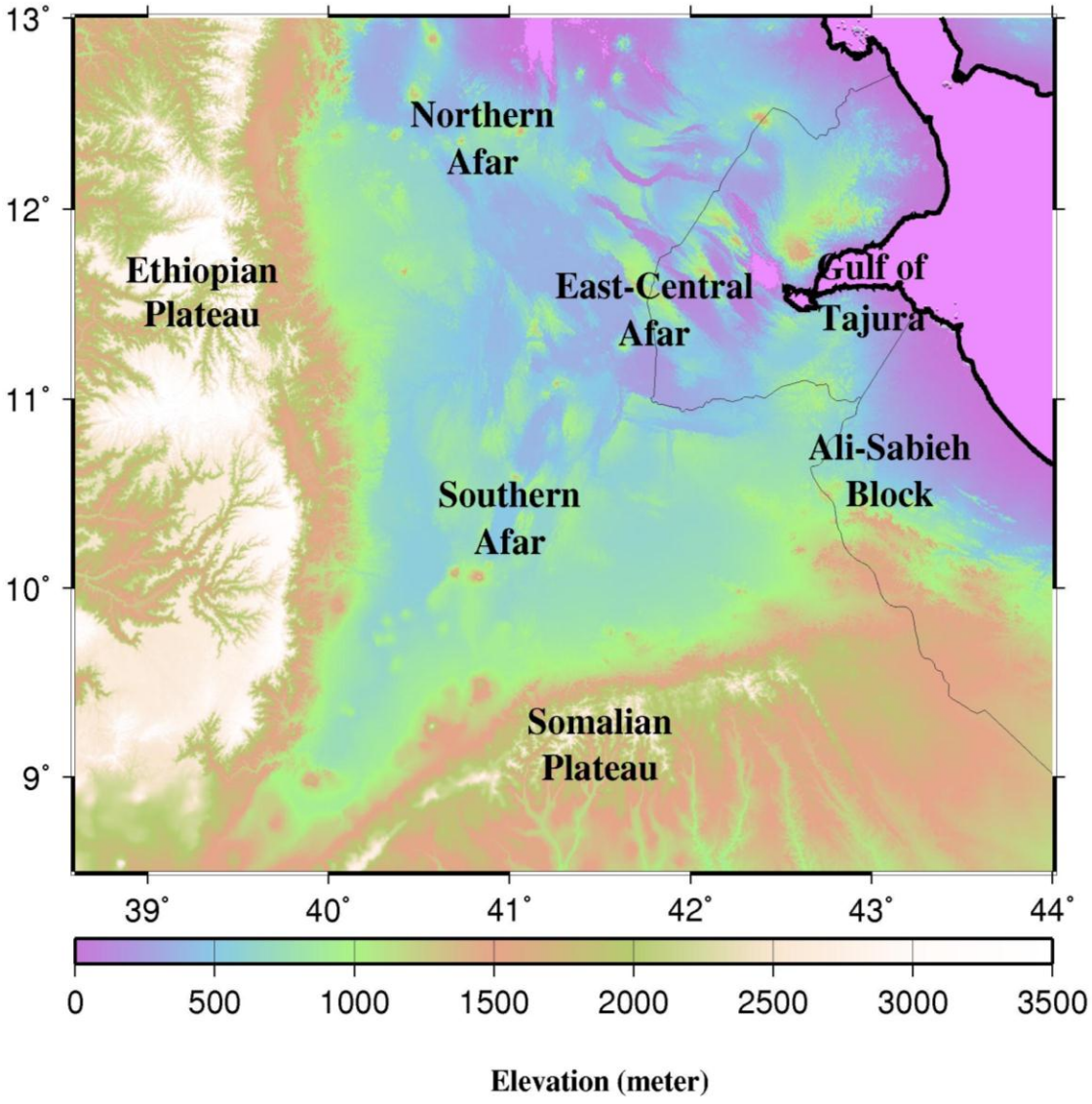

Figure 2.3. The Afar main structural divisions

2.2.2 Southern Afar. The southwestern part is dominated by N to NE-trending structure, while the southeastern part is dominated by prominent E-W trending grabens and horsts [Beyene and Abdelsalam, 2005]. Next to the Somalian Plateau, the region has no marginal basins [Beyene and Abdelsalam, 2005]. Chernet et al. [1998] proposed that the Trap Series in this region had occurred at ~ 24 Ma.

2.2.3 Danakil Block. The Danakil Block has a length of ~ 500 km and a width of ~ 100 km [Le Pichon and Francheteau, 1978; Sichler, 1980; Courtillot et al., 1984; Vellutini, 1990; Souriot and Brun, 1992; Chu and Gordon, 1998; Boccaletti et al., 1999; Collet et al., 2000; Eagles et al., 2002; Manighetti et al., 2001; Tesfaye et al., 2003; Beyene and Abdelsalam, 2005]. It becomes wider from the Gulf of Tajura in the southeast to the Gulf of Zula in the northwest and forms the highest topography in the central part of it (~ 2130 m above sea level) [Beyene and Abdelsalam, 2005]. Chu and Gordon [1998] interpreted that the Danakil Block is similar to a micro-plate that has been pulled out into the Red Sea.

2.2.4 Ali-Sabieh Block. The Ali-Sabieh Block, sometimes referred as the Aysha-Ali-Sabieh [Rouby et al., 1996], is the end of the boundary of the Somalia Plateau located at the southeast of the Afar Depression. The Gulf of Tajura separates the Danakil and the Ali-Sabieh Blocks [Beyene and Abdelsalam, 2005]. The block is assumed to have rotated 90^{o} clockwise over the last 20 Ma for the duration of the opening of the Afar Depression [Manighetti et al., 2001]. Part of the region is occupied by Neoproterozoic rocks [Beyene and Abdelsalam, 2005], while flood basalts of 25-15 Ma occur

in limited parts of the block [Varet, 1978; Vellutini, 1990; Acton et al., 1991].

2.3 GEOLOGY OF THE STUDY AREA

The 18 broadband seismic stations that we deployed lie between 11.31° to 12.05°N and 40.57° to 41.92°E and are located in the NE end of the Main Ethiopian Rift (MER), the Tendaho Graben (TG), and the Dobi Graben (DG).

2.3.1. The Main Ethiopian Rift (MER). The Main Ethiopian Rift is a part of the East African Rift System and located between 5° to 9°N and 37°30´ to 40°E [Woldegabriel et al., 1990; Kusky, 2005]. It connects the Afar Depression to the Kenya Rift [Agostini, 2010]. The MER started to develop during the Miocene [Davidson and Rex, 1980; WoldeGabriel et al., 1990]. Generally, the region is characterized by NE trending structure across the Ethiopian Plateau [Abebe et al., 2007; Keranen and Klemperer, 2008]. The opening rate across the Main Ethiopian Rift is ~ 4 mm/year [Bilham et al., 1999]; this slow rate might be the outcome of rift opening by upwelling mantle plume [Beyene and Abdelsalam, 2005]. The MER can be divided into three divisions based on the surface geology: Northern MER, Central MER and Southern MER [Keranen and Klemperer, 2008].

2.3.1.1 Northern Main Ethiopian Rift. Most of the northern Main Ethiopia Rift is equipped with Mid-Miocene border faults [WoldeGabriel et al., 1990; Wolfenden et al., 2004]. The NMER is underlain by Trap Series and occupied by Late Miocene and Pliocene-Pleistocene sediments [Chernet et al., 1998; McCoy and Heiken, 2000]. The initial extension started at 11 Ma

[Wolfenden et al., 2004]. The boundary faults in this region are inactive and mostly eroded [Casey et al., 2006; Keir et al., 2006; Wolfenden et al., 2004]. Magmatic segments in the area are consisting of volcanoes, basaltic fissure, and young fault belts [Keranen and Klemperer, 2008].

2.3.1.2 Central Main Ethiopian Rift. The CMER is mainly composed of rift segments surrounded by decline extended faults [Keranen and Klemperer, 2008]. The region occurred in the Late Miocene-Early Pliocene (~ 6-8 Ma) [Bonini et al., 2005; Woldegabriel et al., 1991]. Bonini et al. [2005] suggested that most tectonic activity in CMER occurred after 5 Ma from the Miocene-Pliocene boundary. The oldest rocks found are basaltic ~ 29 Ma [Bonini et al., 2005].

2.3.1.3 Southern Main Ethiopian Rift. Faulting in the SMER is believed to be established by ~ 18 Ma [Ebinger et al., 1993]. Rift development in the region is interconnected with the eruption occurred between 19 and 11 Ma [George et al., 1998; George and Rogers, 2002]. The motions of the Nubian and Somali plates effect the current extension of the SMER [Acocella and Korme, 2002; Bilham et al., 1999]. The age of the oldest volcanic rocks dated at 45 Ma [Davidson and Rex, 1980; George, 1997; George et al., 1998; Ebinger et al., 2000].

2.3.2. The Tendaho Graben (TG). The Tendaho Graben, considered being the largest depression of Central Afar, is ~ 150 km long and 25-50 km wide and has been formed ~ 1.8 Ma [Barberi et al., 1975; Acton et al., 1991]. It is considered to be a part of the southern extension of the Red Sea structure connecting the Ethiopian Rift that is filled with Quaternary volcanics

mainly basalts and fluvio-lacustrine sediments [Gianelli et al., 1998]. The TG is characterized by normal and strike-slip faults and bordered by NW-SE-trending faults that dip away from its axis [Abbate et al., 1995; Gresta et al., 1997; Acocella, 2010]. Stratoid deposits cover most of the bedrock of the graben [Lahitte et al., 2003b; Kidane et al., 2003]. The rift is filled with lacustrine, alluvial deposits, and basalt flows [Aquater, 1996; Lemma et al., 2010].

2.3.3. The Dobi Graben (DG). The Dobi Graben, a narrow and deep basin, is ~ 50 km long and ~ 12 km wide and characterized by NW-SE-trending normal faults structure [Tesfay et al., 2008; Acocella, 2010; Beyene and Abdelsalam, 2005]. The DG is located at the east-central block of the Afar Depression and dominated by flood basalts [Beyene and Abdelsalam, 2002]. The DG bedrock consists of stratoids and the development of it is of the same period of the Tendaho Graben [Acton et al., 2000]. Moreover, DG is smaller and has a steeper inclination than the TG [Ali, 2001].

3. PREVIOUS GEOPHYSICAL STUDIES OF THE AFAR CRUST

3.1 REFRACTION DATA

Previous seismic refraction data described the southern part of Afar as having a crustal thickness between 28-30 km whereas it is merely about 15 km in the Danakil depression (Figure 3.1) [Berckhemer et al., 1975; Prodehl and Mechie, 1991; Prodehl, et al., 1997]. An earlier seismic refraction profile across southeastern Afar shows a thin oceanic-type crust, with increase of V_p from 6.8 km/sec at 6-10-km depth up to 7.3 km/sec at 20-km depth [Ruegg and Lepine, 1973]. Ruegg [1975] proposed that the upper lithosphere beneath the Djibouti region is an oceanic type. Berckhemer et al. [1975] conducted deep seismic refraction surveys to estimate the crustal structure in Afar, and found that the crustal thickness varies from 14 to 26 km and that the bulk of the Afar crust has seismic velocity ranging from 6.6 to 6.8 km/s. They also reported that crustal thickness thins from 26 to 23 km towards the Red Sea. Their interpretation suggests a crustal thinning as well as upwelling of hot material arriving from the upper-mantle beneath Afar.

3.2 GRAVITY DATA

Gouin [1970] found out, using seismic and gravity data, that the total anomalies of the free-air gravity are just about zero over Afar and that the Bouguer values are, in general, negative and proportional to elevation. He suggested a typical continental crustal thickness structure under the Afar Depression. Makris et al. [1972, 1975] proposed the existence of an attenuated continental crust beneath Afar. The results of the seismic and gravity data collected by Makris and Ginzburg [1987] clarified that Afar is

underlined by a thin transitional lithosphere. They also observed low seismic velocities structure. By using gravity and topography data, Mammo [2004] concluded that the crustal of Afar is thin and it is intermediate-crustal-type. He also noticed that the crust happens to be thinner towards the north and east directions. Results from Bouguer gravity data point out crustal thinning in Afar region with an average thickness of ~ 25 km [Makris and Ginzburg, 1987; Woldetinsae and Gotze, 2005]. In addition, by using inverse modeling of gravity data, Tiberi et al. [2005] estimated a low crustal thickness of 23 km in Afar Depression and 24 km south of it.

3.3 SEISMIC DATA

Niazi [1968] has suggested, using data from teleseismic earthquakes, a continental-crust model for the Afar Depression. His crustal model includes a normal, double-layers continental crust of 35 km thickness covered by 0.5 km thick unconsolidated sediments. From the analysis of surface waves, Searle [1975] found out that Poisson's ratio varies from 0.25 to 0.29 within the crust beneath Afar, whereas Ruegg [1975] characterized the eastern division of Afar, from deep seismic sounding studies, by an exceedingly high value of Poisson's ratio that reaches 0.33. Dugda et al. [2005] revealed, using receiver function analysis from seismic data, that the crust beneath Afar is just about 25 km thick. They also reported, from a temporary broadband station located at Tendaho area, a high crustal Poisson's ratio of 0.36. By applying receiver function analysis, Stuart et al. [2006] interpreted a mafic crust along with the presence of partial melt (where $V_p/V_s > 1.95$) near the Afar Depression. Dugda and Nyblade [2006] characterized the crust

beneath Afar by fairly uniform thickness varying between 20-25 km. Their method of receiver function analysis verified a high Poisson's ratio throughout most of the crust and is an indication of a mafic composition. They interpreted the presence of new igneous rock in the crust as a part of the extensional process in the region. Benoit et al. [2006] revealed that a low wave speed anomaly aligns with the Afar Depression and the Main Ethiopian Rift in the uppermost mantle by using P-wave tomography. They also proposed a shift of the low wave speed anomaly to the west with depth. Dugda et al. [2007] obtained shear velocity models from the joint inversion of Rayleigh Wave Group Velocities and Receiver functions and showed crustal thickness ranging from 25 to 35 km beneath the Main Ethiopian Rift and the Afar Depression. They also observed that the lithospheric mantle has a maximum shear wave velocity of 4.1-4.2 km/s and extends to a depth of at most 50 km. Hansen et al. [2009] estimated the lithospheric thickness beneath station ATD and found that it is 34 km by using S-Wave receiver functions. They found that this thin lithosphere, observed at this station, is consistent with the transition from continental to oceanic rifting at the Afar Depression. They linked their findings with the presence of the mantle plume which is the reason for the thin lithosphere. Most of the above conclusions pointed out that the crust beneath Afar is mainly thin and it has been modified by both magmatic processes and the accumulation of mafic rock in the mid-to-lower crust.

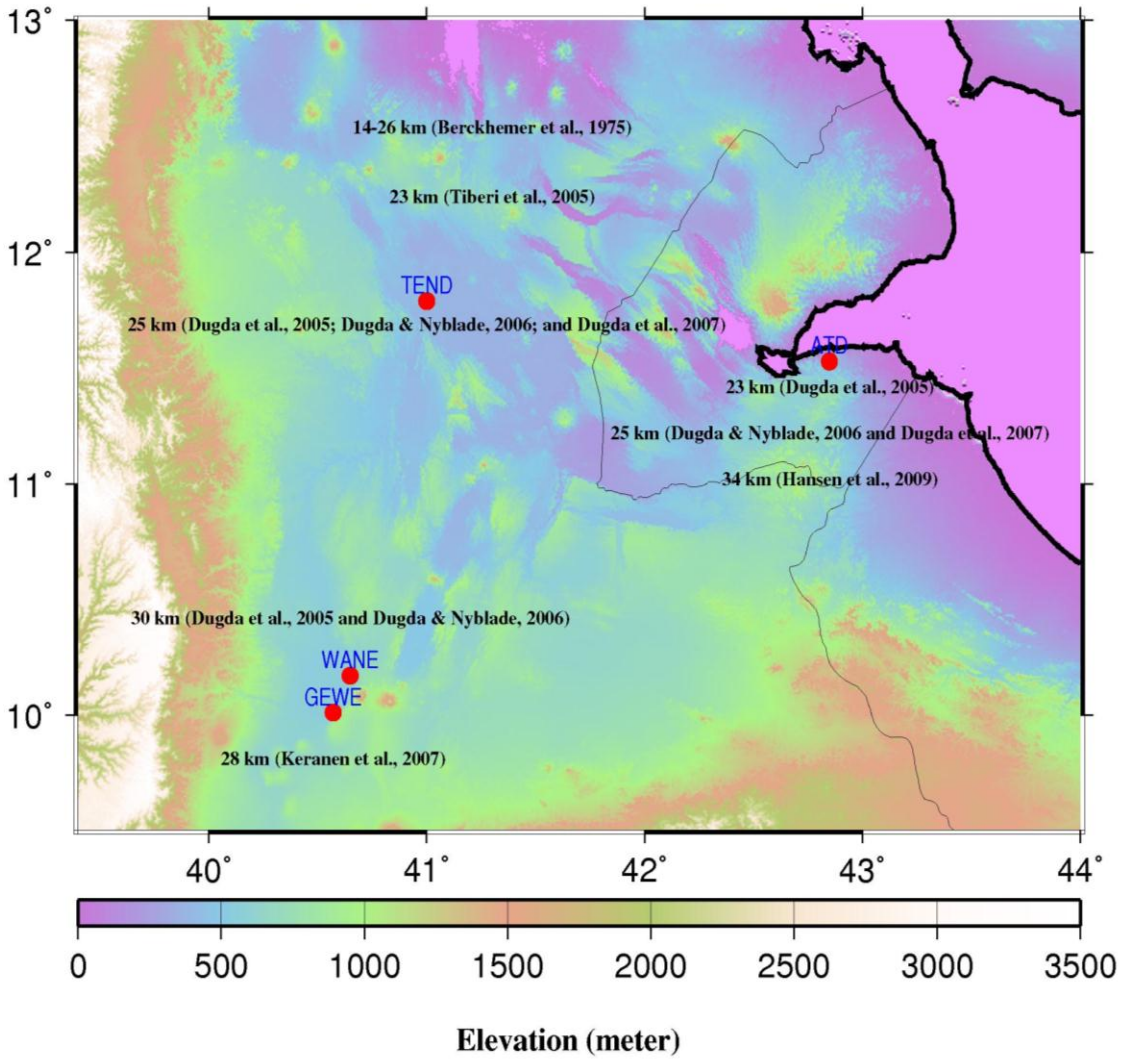

Figure 3.1. Topographic map of the Afar Depression showing previous determinations of crustal thickness

4. RECEIVER FUNCTION ANALYSIS

Receiver function analysis is a robust method used to determine the Earth's crustal structure (Figure 4.1) [Langston, 1977; Vinnik, 1977; Clouser and Langston, 1995; Liu et al., 2003; Gao et al., 2004; Liu and Gao, 2006; Nair et al., 2006; Liu and Gao, 2010]. It utilizes the teleseismic earthquake waveforms, recorded at a three components seismometer, to image the crustal structures beneath isolated seismic stations [Ammon, 1991]. The analysis detects the crustal/mantle boundary by identifying P-to-S converted waves and their multiples from the Moho. A receiver function can be calculated by deconvolving the vertical component from the radial component for a given event [Phinney, 1964; Langston, 1977; Ammon, 1991; Sheehan et al., 1995; Dueker and Sheehan, 1998; Ramesh et al., 2002; Gilbert et al., 2003; Wilson et al., 2005]. Primary conversion (PmS or Ps) and multiple phases (PPmS which is also called PpPs, and PSmS which is also called PpSs) can frequently be observed (Figure 4.2). Multiples phases are weaker than the Ps wave and therefore they are occasionally hard to recognize [Yuan et al., 2002]. Crustal thickness and the average crustal V_p/V_s ratio can be estimated by the identification of the crustal multiples [Zandt et al., 1995; Zhu and Kanamori, 2000]. The V_p/V_s ratio is a valuable measure of crustal composition (using its relation to Poisson's ratio) [Zandt et al., 2004; Behn and Kelemen, 2006].

In this study, a procedure based on the Zhu and Kanamori [2000] H-k stacking technique was applied, where H is the Moho depth and Φ is the ratio

between V_p and V_s. A series of candidate depth H_i in the range from 15-55 km in

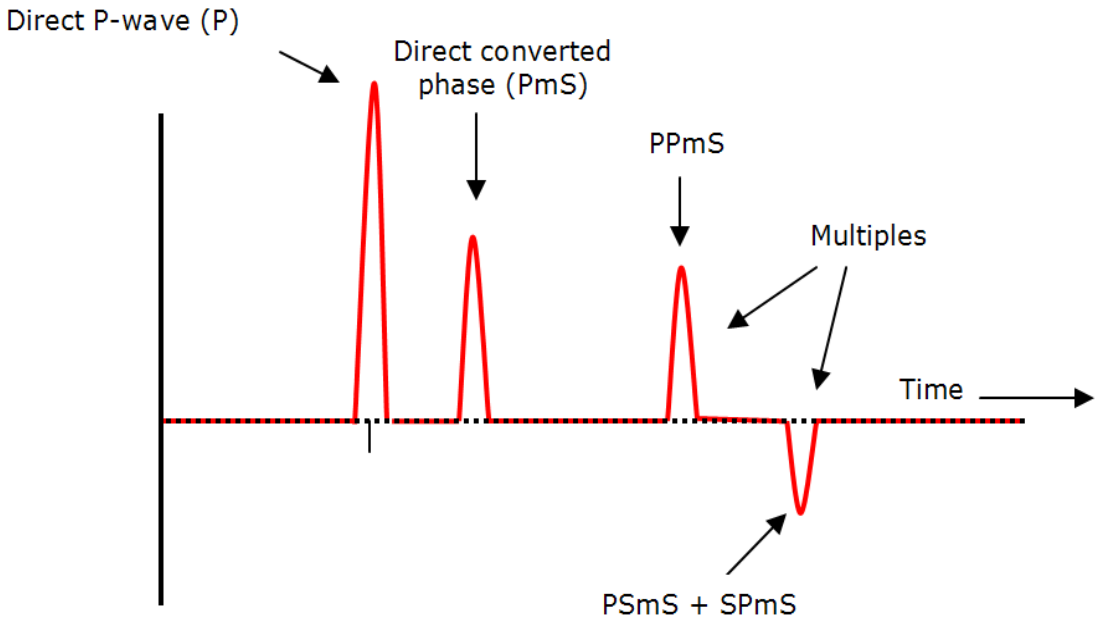

Figure 4.1. Diagram showing the major PmS converted and the multiples phases

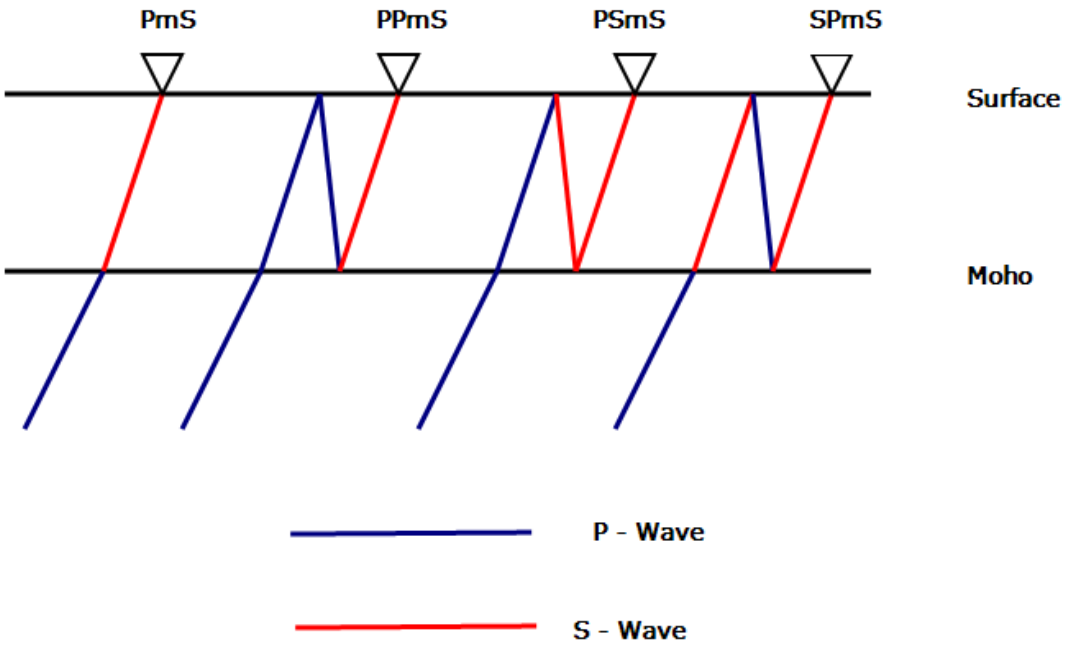

Figure 4.2. The ray paths of the converted PmS wave and the multiples phases

increments of 0.1 km and candidate Φ_j from 1.70 to 2.10 in increments of 0.0025 were used. For each (H_i, Φ_i) the moveout of PmS, PPmS and PSmS were calculated using the method of Nair et al. [2006]. The following equations (1-4) were used to calculate the moveout of PmS, $t_1^{(i,j)}$ [Sheriff and Geldart, 1993; Dueker and Sheehan, 1998; Nair et al., 2006].

$$t_1^{(i,j)} = \int_{-H_i}^{0} [\sqrt{(V_p(z)/\phi_j)^{-2} - p^2} - \sqrt{V_p(z)^{-2} - p^2}]dz \qquad (1)$$

Where p is the P wave ray parameter, H_i is the depth of the candidate discontinuity, Φ_j is the candidate V_p/V_s, and $V_p(z)$ is the P wave velocity at depth z.

The moveout, $t_2^{(i,j)}$ of PPmS is calculated using:

$$t_2^{(i,j)} = \int_{-H_i}^{0} [\sqrt{(V_p(z)/\phi_j)^{-2} - p^2} + \sqrt{V_p(z)^{-2} - p^2}]dz \quad (2)$$

And that of PSmS, $t_3^{(i,j)}$, is:

$$t_3^{(i,j)} = \int_{-H_i}^{0} 2\sqrt{(V_p(z)/\phi_j)^{-2} - p^2}\, dz \quad (3)$$

The receiver functions at each of the stations are then stacked using:

$$A(H_i, \phi_j) = \sum_{k=1}^{n} w_1 S_k(t_1^{(i,j)}) + w_2 S_k(t_2^{(t,j)}) - w_3 S_k(t_3^{(i,j)}) \quad (4)$$

where n is the number of radial receiver functions from the station, $S_k(t)$ is the amplitude of the point on the kth receiver function at time t after the first P arrival (where t = t_1, t_2 or t_3), and w_1, w_2, and w_3 are weighting factors that satisfy $w_1 + w_2 + w_3 = 1$ [Zhu and Kanamori, 2000 and Nair et al., 2006].

We used 0.5, 0.3, and 0.2 for the weighting factors, respectively. A reference crustal velocity Vp(z) of 6.3 km/s was chosen for the Afar Depression. Radial receiver functions from hundred of events were stacked along the travel time curves of the converted and reflected phases at the Moho. Position's ratio (σ) was calculated using the formula $\sigma=0.5[1-1/(\Phi^2-1)]$, where Φ is the P and S wave velocity ratio [Tarkov and Vavakin, 1982; Christensen, 1996; Chevrot and van der Hilst, 2000]. To determine the apparent sharpness of the Moho beneath a station, we measure R, which is the ratio between the stacking amplitude corresponding to the optimal pair of (H, Φ) and the mean amplitude of the direct P wave on the radial components. The sharpness of the Moho is associated with the thickness of the transition layer between the crust and the mantle. From the analysis of refracted seismic arrivals, the transition layer is not more than ½ km thick in stable areas [Nakamura and Howell, 1964]. To estimate the standard deviations of the resulting parameters, we used the bootstrap method [Efron and Tibshirani, 1986; Press et al., 1992]. The results were obtained by using the computer programs developed at the Geophysical group at Missouri S&T [Gao et al., 2002; Liu et al., 2003; Gao et al., 2004; Liu and Gao, 2006; Nair et al., 2006; Liu and Gao, 2008].

5. DATA

We deployed 18 Gűralp CMG-3T broad-band seismometers with the help of the Program for Array Seismic Studies of the Continental Lithosphere (PASSCAL) Instrument Center and the Geological Survey of Ethiopia (GSE) in December 2009. The stations we deployed were along a profile of 250 km long with a station spacing of ~ 10 km. Stations locations are shown in Figure 5.1 and listed in Table 5. The instruments recorded data at 100 samples per second for a 12-month period of operation from December 2009 to December 2010. The CMG-3T is a compact three-component broadband that consists of three sensors in a sealed case, which measure the north/south, east/west and vertical components of ground motion. Each sensor is sensitive to ground vibrations in the frequency range of 0.003 – 50 Hz [Güralp Systems Limited, 2009]. The stations have been visited and serviced twice, in June 2010 and December 2010. The dataset consists of approximately 1400 three-component seismograms from earthquakes in the epicentral distance range of 30^{o} – 180^{o} and have magnitude greater than 5.2 (Figure 5.2). Hundreds of earthquakes were recorded with great quality. Data from these events have been converted into radial and transverse receiver functions using the procedure of Ammon et al. [1990]. The seismograms were band pass filtered in the 0.05–1.5 Hz range to improve signal to noise ratio. Figure 5.3 shows some photos taken from the field.

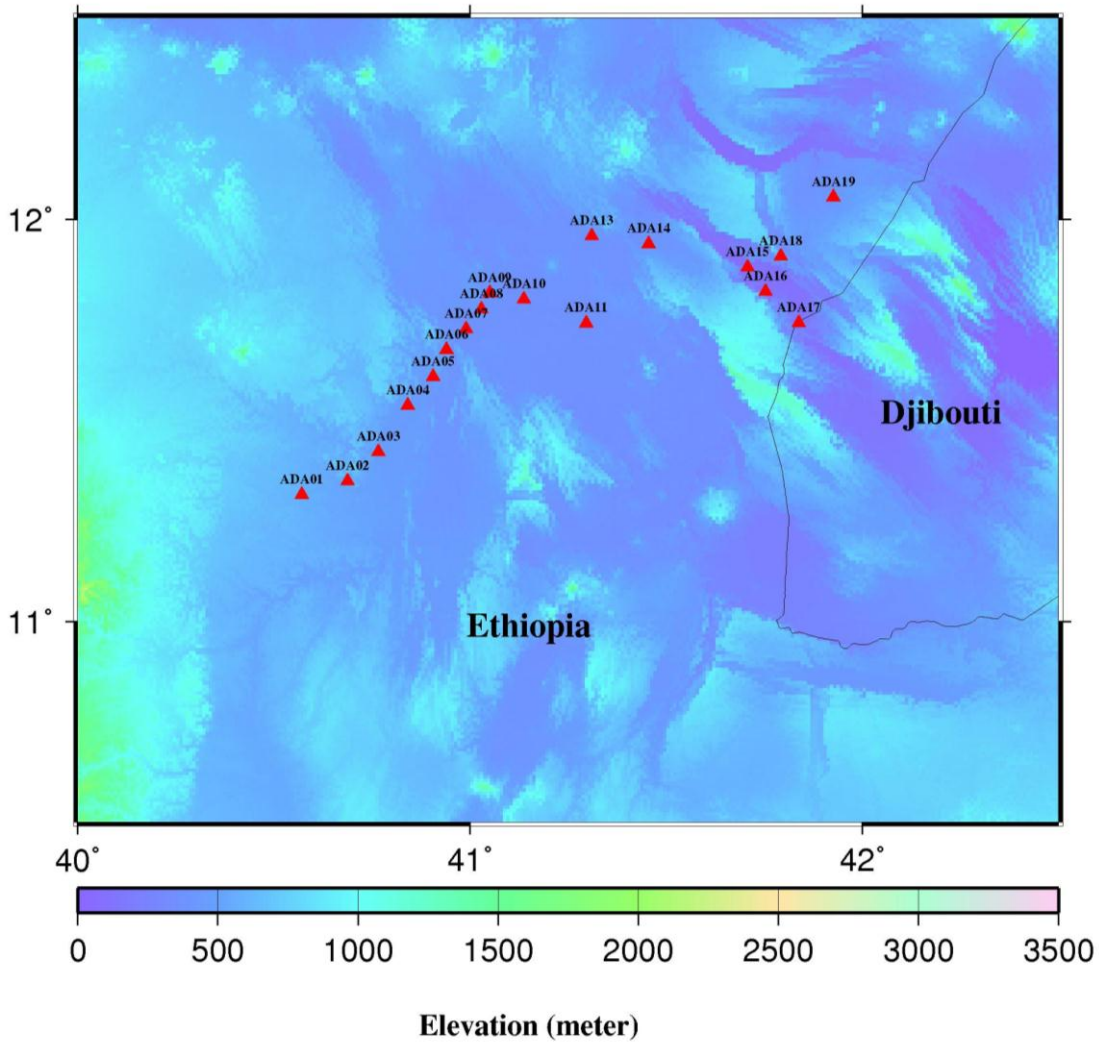

Figure 5.1 Locations of seismic stations in the Afar Depression

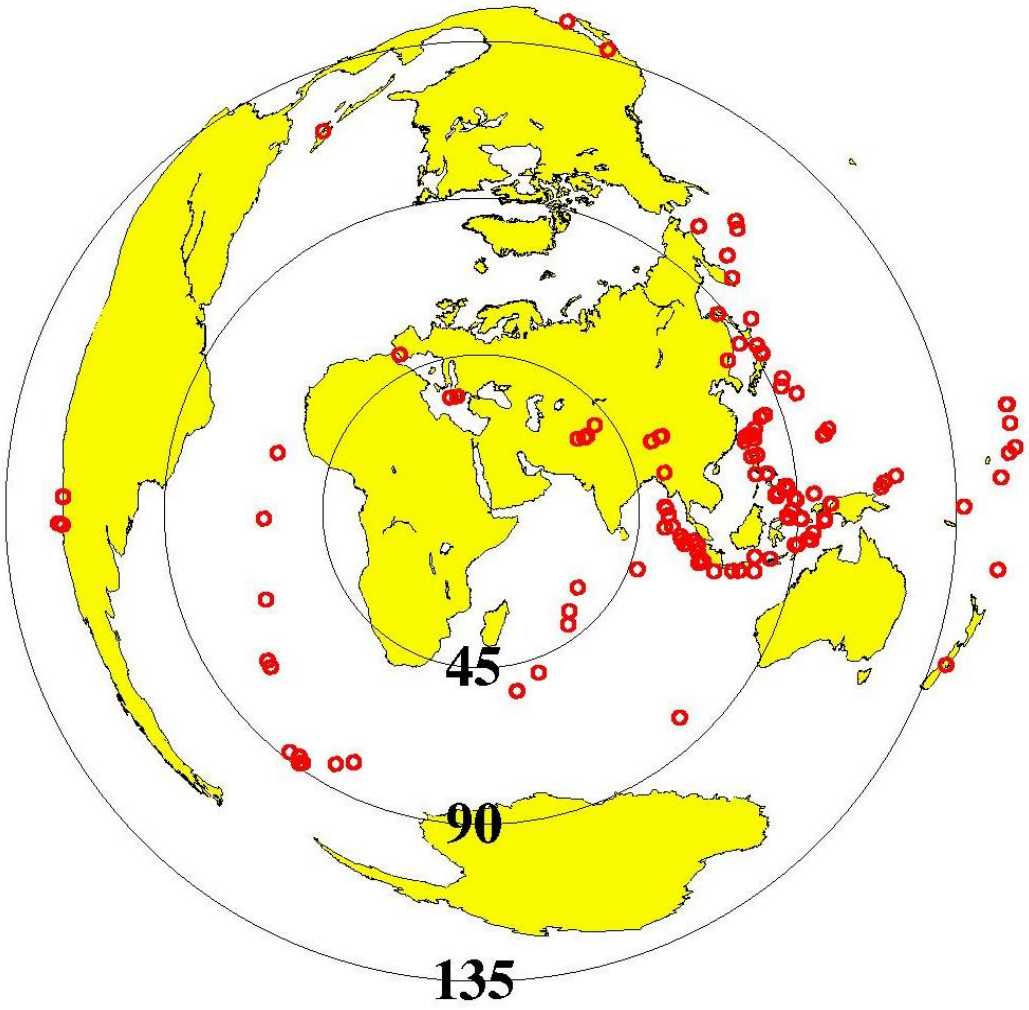

Figure 5.2 Locations of the seismic events used in the Afar Depression

Figure 5.3 Some photos taken from the field in the Afar Depression

6. RESULTS

Observations of H, R, and σ were obtained at most of the stations. P-to-S conversions from the Moho can be observed on the majority of the stations from stacked receiver functions. The results were organized into two categories (A and B) based on the quality of the H-k plots. Those in category A (AD01, AD02, AD03, AD04, AD05, AD08, AD13, AD15, AD16, AD17, and AD18) display a clearly defined single peak in the H-k plots, and therefore both H and Φ can be determined with high confidence. The arrival of PmS for category A, was in the time window of 3-4.5 s. Category B stations (AD06, AD07, AD09, AD10, AD11, AD14, and AD19) show clear PmS but not PPmS and PSmS. Thus an optimal pair of (H, k) cannot be determined. For those stations, an estimate of the crustal thickness (H_n) was obtained using a Φ of 1.85 which is approximately the averaged V_p/V_s found at category A stations. The results of the H-k stacking are divided into three divisions: Stations SW of TG (AD01-AD05), TG stations (AD06-AD13), DG and the adjacent horsts stations (AD14-AD19).

6.1 STATIONS SOUTHWEST OF THE TG

The crustal thickness beneath these stations ranging from 25.33±0.11 km (AD05) to 35.22±0.33 km at AD02. The Φ values range from 1.844 at AD03 to 1.988 at both AD05. The R values observed are from 0.069 (AD04) to 0.181 (AD01).

AD01: The station is located at 11.315°N and 40.571°E with elevation of 580 m and represents an A quality station. A total of 86 receiver functions have been stacked. The amplitude of the PmS phase is weak between the ranges

30°-100° with the arrival times from about 2.8 s to 3.2 s. The amplitude of the PmS phases increase for events from the northwest (320°-340°) of the station with arrival times vary from about 1 s to over 4 s. The back-azimuth range of 120°-180° shows a strong arrival of this phase that is observed at 3.8 s to 4.2 s after the direct P-wave (Figure 6.1.a). The ray-piercing points are mainly distributed in the east and northeast and some are in the northwest and southeast directions (Figure 6.1.b). From the H-k plot, a well defined peak can be observed which is marked by the black dot (Figure 6.1.c). The resulting optimal Moho depth is 31.77±0.19 km, the corresponding V_p/V_s is 1.937±0.013 and the resulting R value is 0.181±0.019.

AD02: The station is located at 11.35°N and 40.688°E with elevation of 523 m and represents an A quality station. A total of 134 receiver functions have been stacked. The first positive peak of PmS on the radial receiver function can be observed from ~ 1 s in the back-azimuth of 10° (Figure 6.2.a). The peak becomes weaker between the ranges of 40°-100° with the arrival times from 2 s to 3.5 s. The back-azimuth range of 190°-260° shows a strong arrival of PmS phase that is observed at 3.8 s to 5 s after the direct P-wave. Most of the events originated from the north-east, east and west, with few events back azimuth coverage from the northwest (Figure 6.2.b). From the H-k plot, a well defined peak can be observed which is marked by the black dot (Figure 6.2.c). The resulting optimal Moho depth is 35.23±0.1 km, the corresponding V_p/V_s is 1.852±0.007 and the resulting R value is 0.089±0.006.

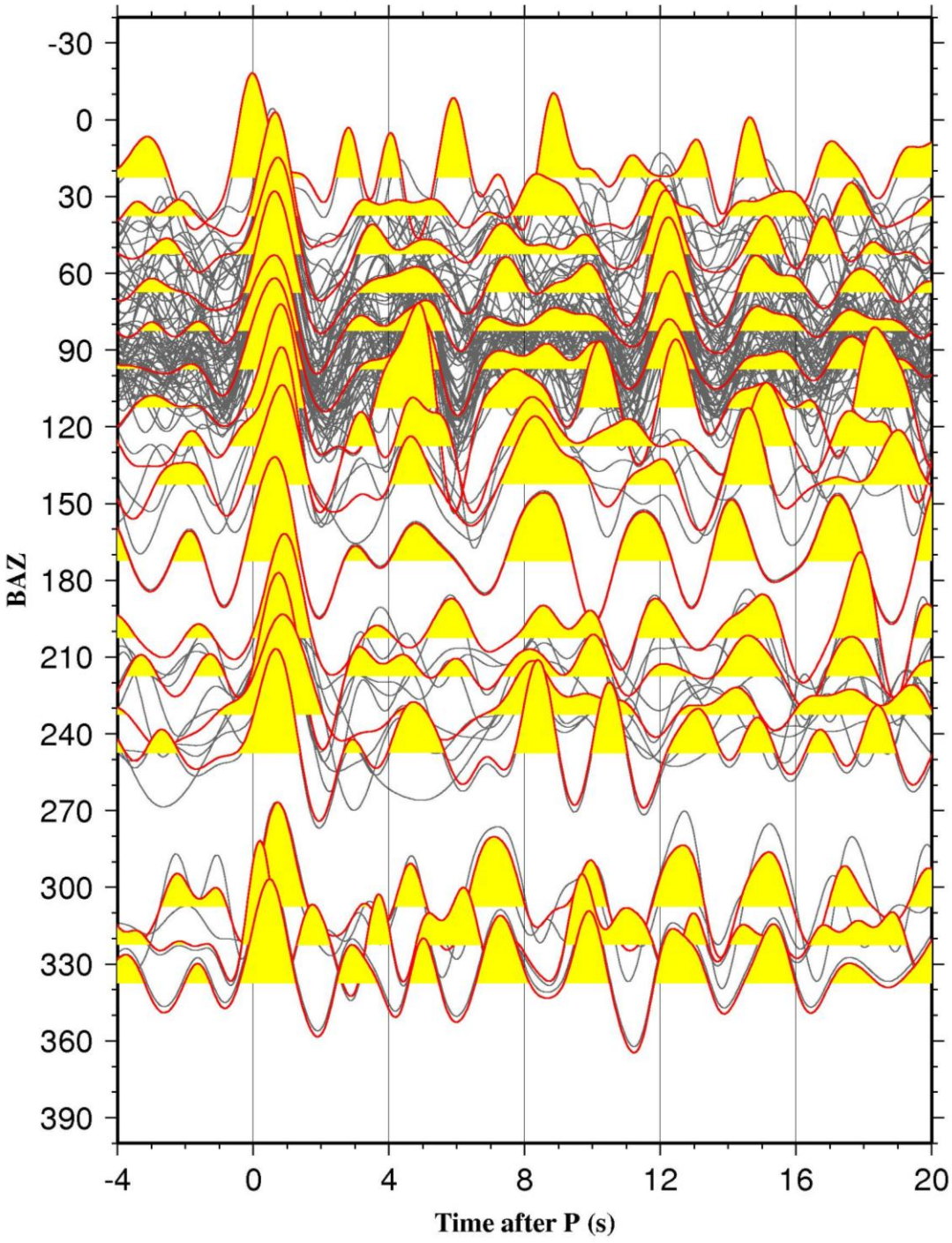

Figure 6.1. (a) Radial receiver functions plotted against the back-azimuth (BAZ) for AD01. Gray thin lines are individual RFs, and red thick lines are stacked RFs in 15° azimuthal bins.

b)

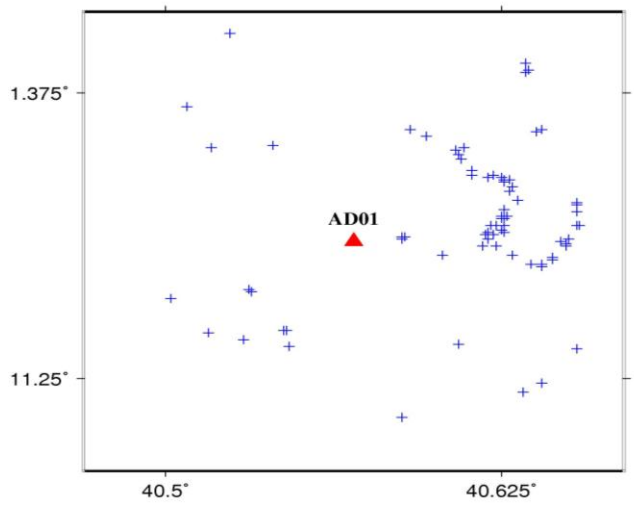

c)

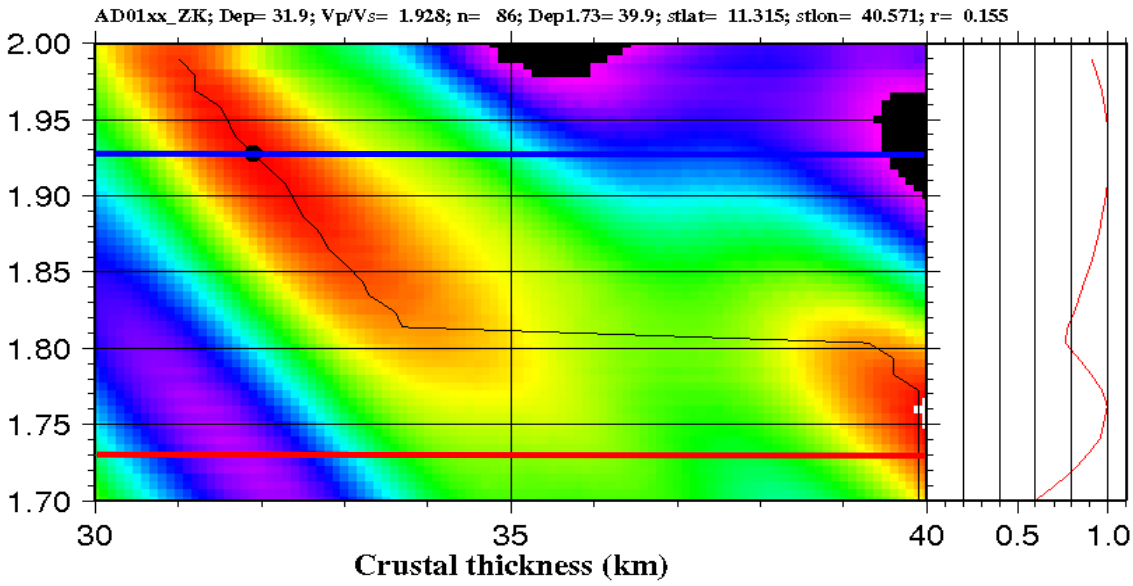

Figure 6.1. (Continued) (b) The distribution of ray-piercing points of the PmS phase for AD01. (c) H-k plots for station AD01. The red line shows the stacking amplitude for Φ=1.73. The blue line was obtained using the optimal Φ.

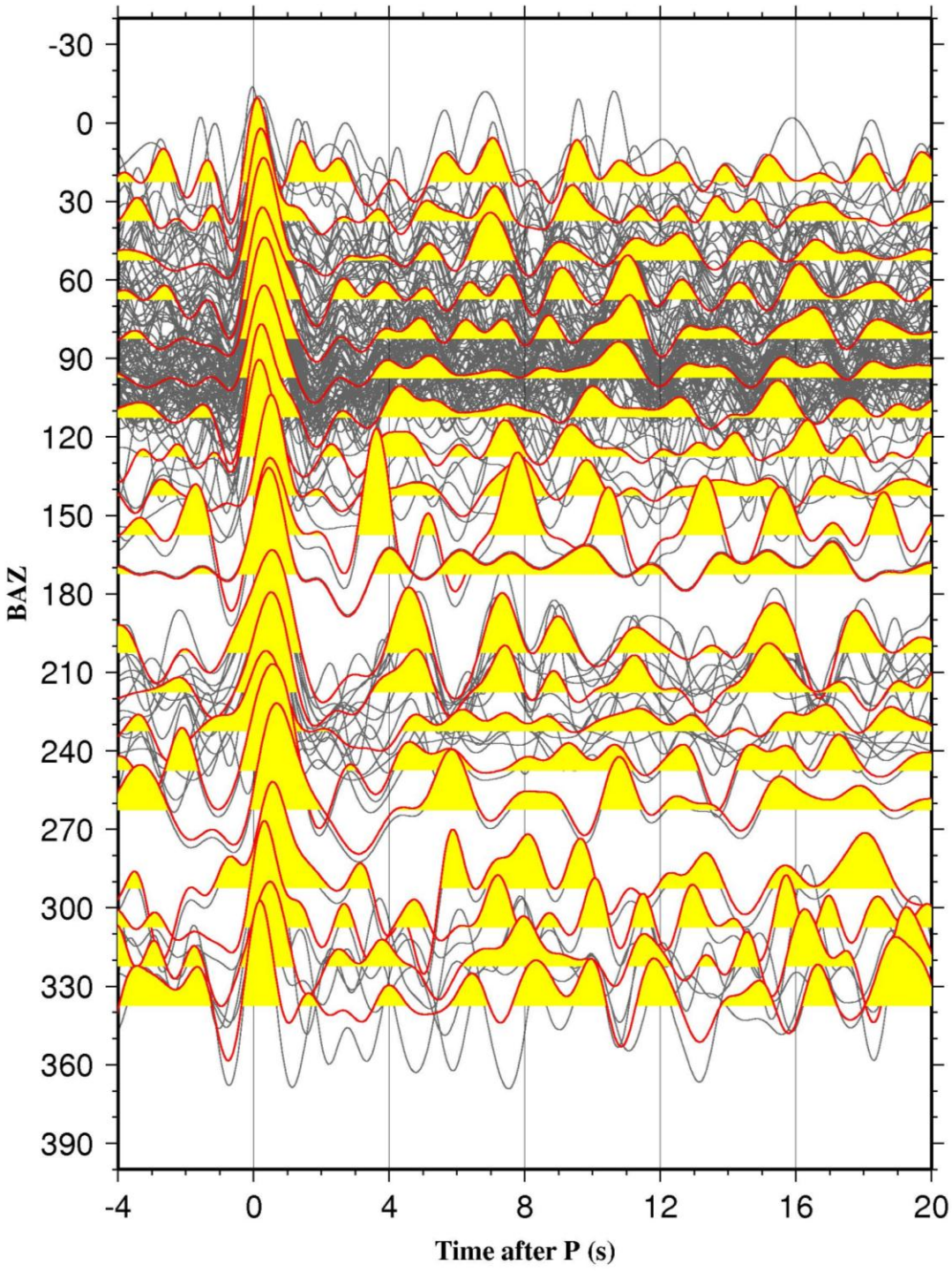

Figure 6.2. (a) Radial receiver functions plotted against the back-azimuth (BAZ) for AD02. Gray thin lines are individual RFs, and red thick lines are stacked RFs in 15° azimuthal bins.

b)

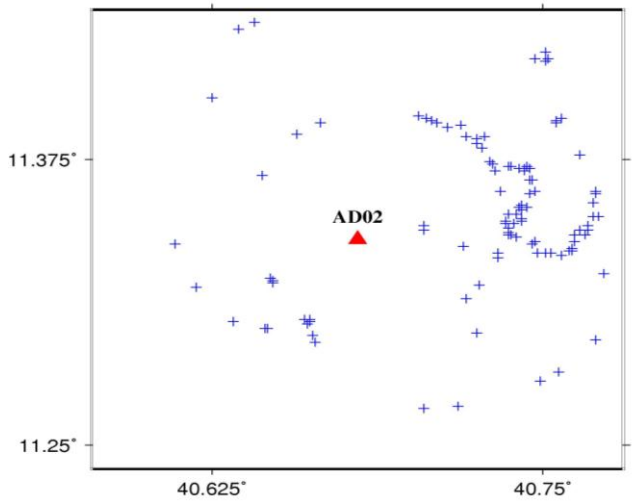

c)

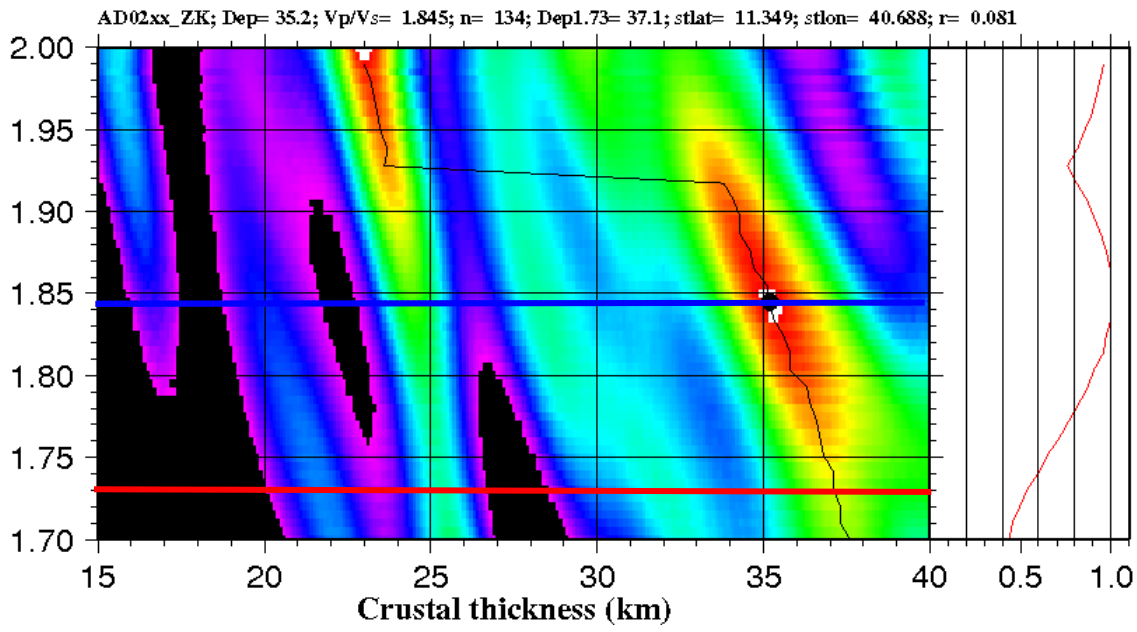

Figure 6.2. (Continued) (b) The distribution of ray-piercing points of the PmS phase for AD02. (c) H-k plots for station AD02. The red line shows the stacking amplitude for Φ=1.73. The blue line was obtained using the optimal Φ.

AD03: The station is located at 11.42°N and 40.77°E with elevation of 488 m and represents an A quality station. A total of 87 receiver functions have been stacked. Most of the back-azimuth ranging from 40°-90° shows arrivals of PmS phase that are observed at 4 s to 5.2 s after the direct P-wave (Figure 6.3.a). Most of the events originated from the north-east, east and west, with few events back azimuth coverage from the northwest (Figure 6.3.b). From the H-k plot, a well defined peak can be observed which is marked by the black dot (Figure 6.3.c). The resulting optimal Moho depth is 32.58±0.33 km, the corresponding V_p/V_s is 1.844±0.024 and the resulting R value is 0.078±0.013.

AD04: The station is located at 11.54°N and 40.841°E with elevation of 483 m and represents an A quality station. A total of 62 receiver functions have been stacked. The amplitude of PmS phase is show small amplitudes between the ranges of 60°-100° with the arrival times from about 2 s to 2.5 s (Figure 6.4.a). For the same back-azimuth ranges, strong Pms phases arrival are observed at 4.7 s to 5 s. The small-amplitude phases that arrive before the Pms phases might represent P-to-S conversions within the crust. The amplitude of the PmS phases increase for events from the northwest (160°-270°) of the station with arrival times vary from about 2.8 s to over 3.3 s. The ray-piercing points are mainly distributed in the east and northeast and some are in the southeast directions (Figure 6.4.b). The resulting optimal Moho depth is 30.93±0.15 km, the corresponding V_p/V_s is 1.987±0.005 and the resulting R value is 0.069±0.009.

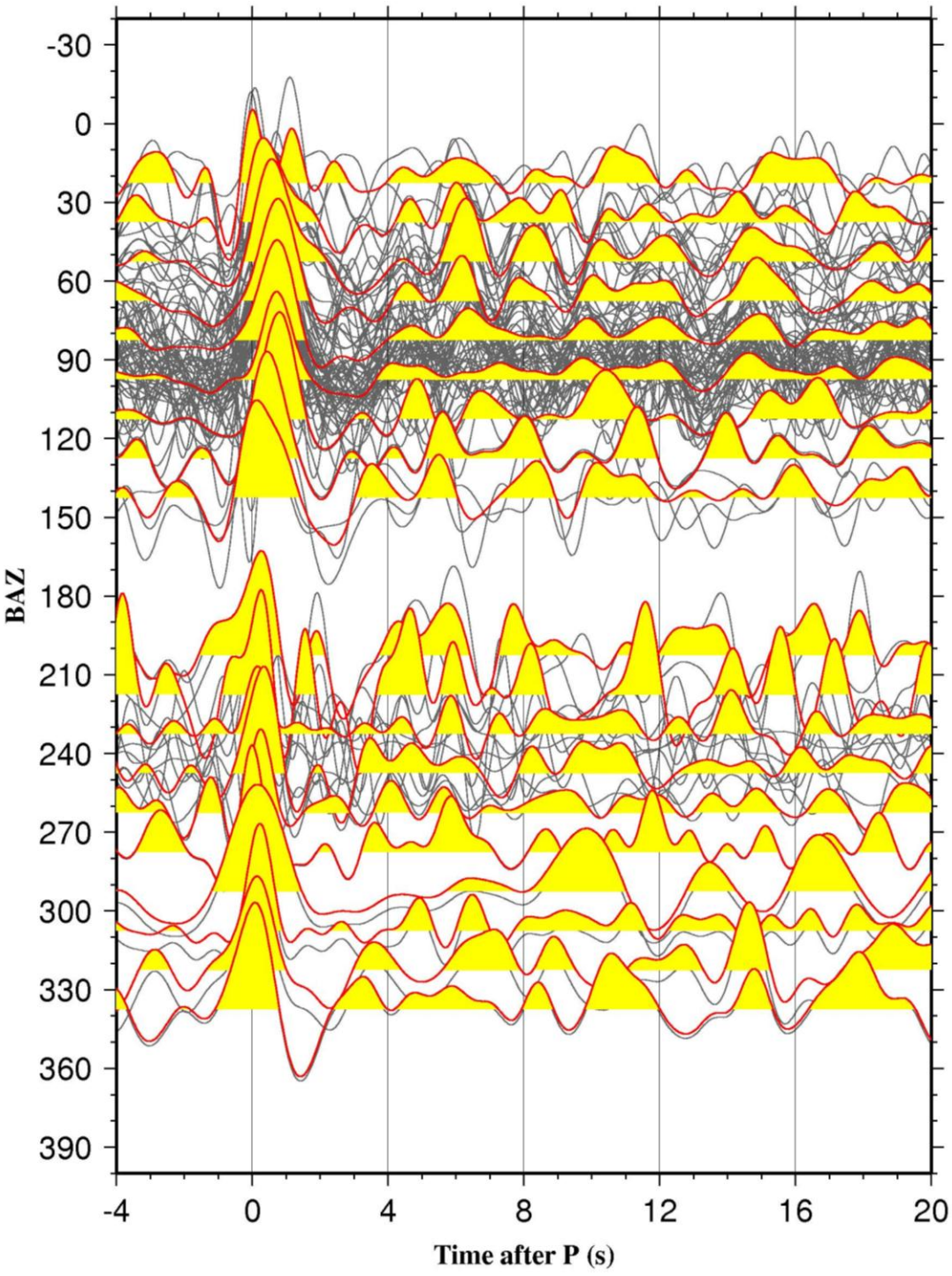

Figure 6.3. (a) Radial receiver functions plotted against the back-azimuth (BAZ) for AD03. Gray thin lines are individual RFs, and red thick lines are stacked RFs in 15° azimuthal bins.

b)

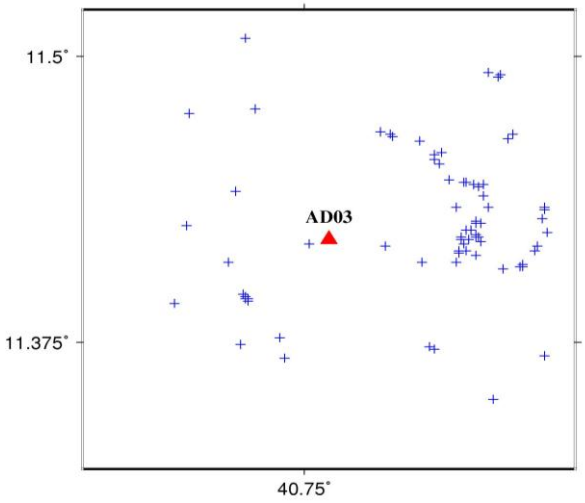

c)

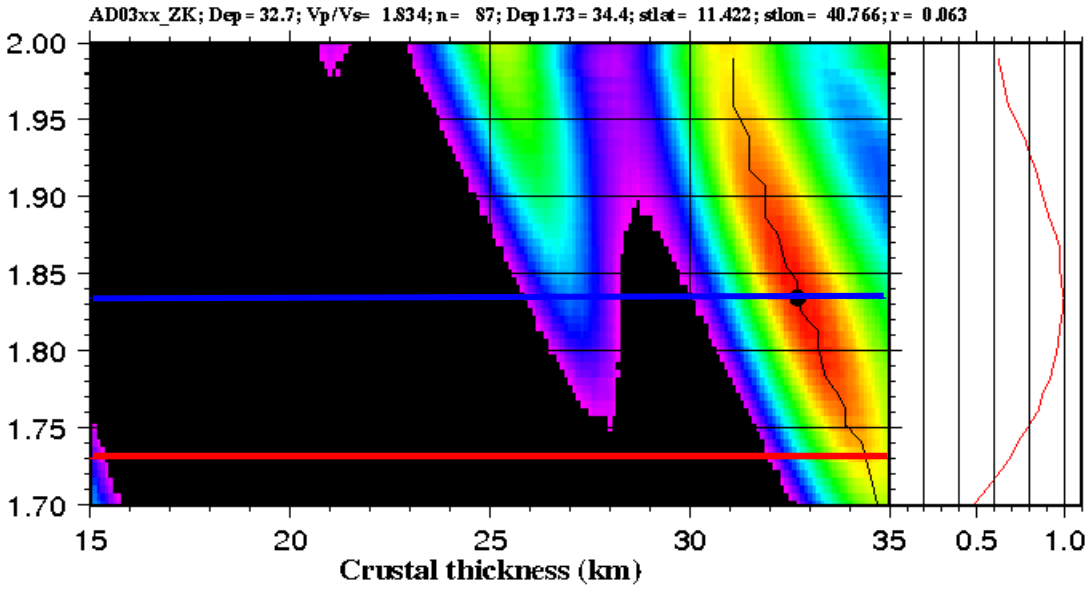

Figure 6.3. (Continued) (b) The distribution of ray-piercing points of the PmS phase for AD03. (c) H-k plots for station AD03. The red line shows the stacking amplitude for Φ=1.73. The blue line was obtained using the optimal Φ.

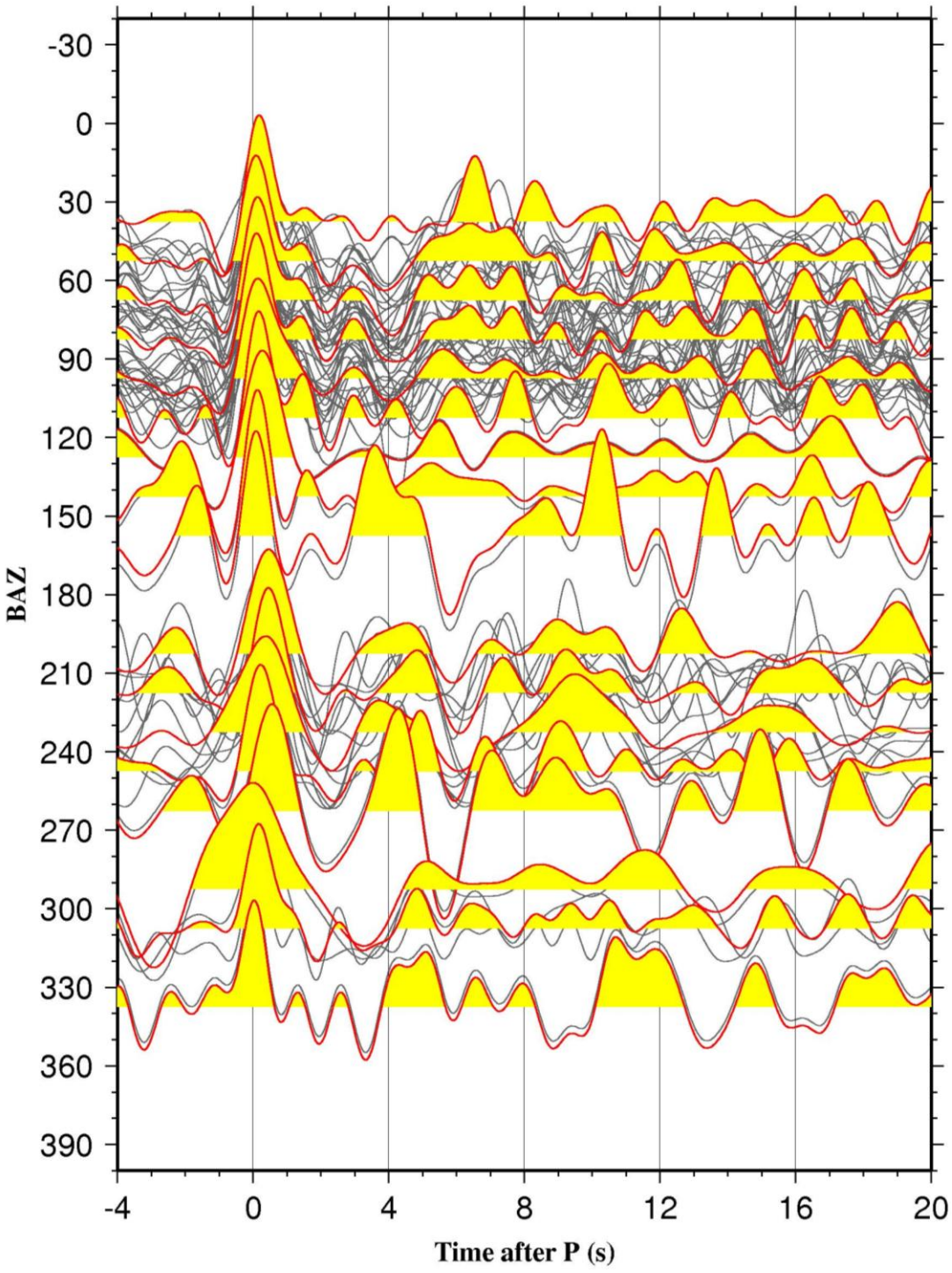

Figure 6.4. (a) Radial receiver functions plotted against the back-azimuth (BAZ) for AD04. Gray thin lines are individual RFs, and red thick lines are stacked RFs in 15° azimuthal bins.

b)

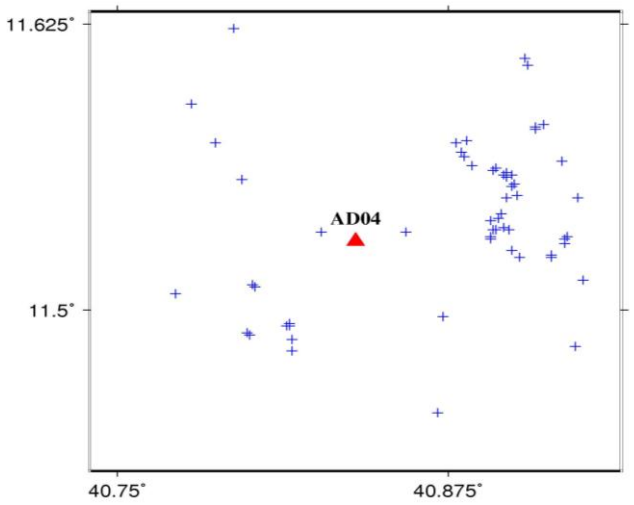

c)

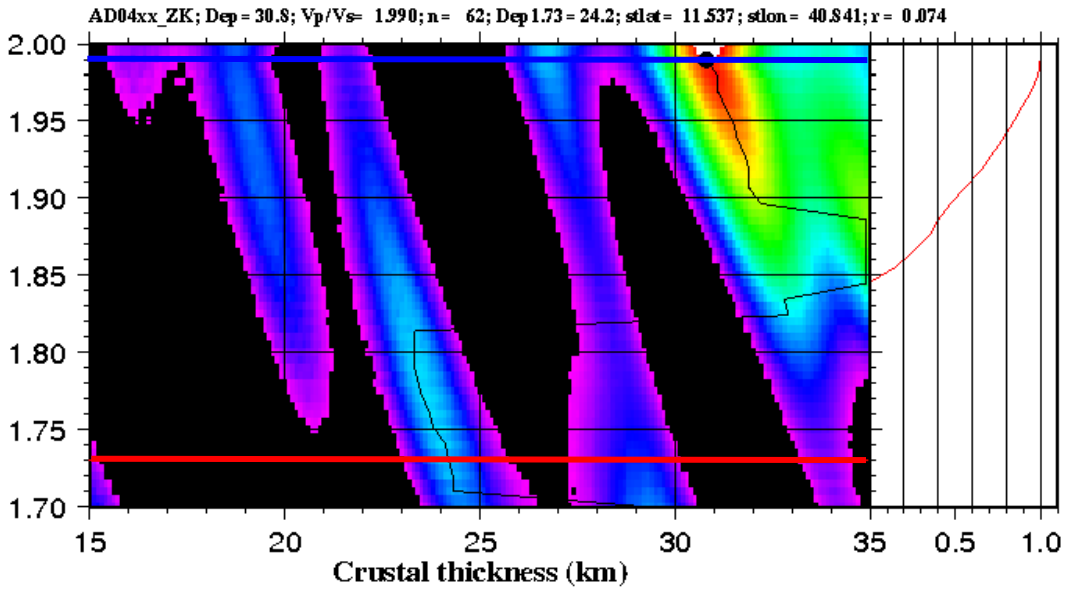

Figure 6.4. (Continued) (b) The distribution of ray-piercing points of the PmS phase for AD04. (c) H-k plots for station AD04. The red line shows the stacking amplitude for Φ=1.73. The blue line was obtained using the optimal Φ.

AD05: The station is located at 11.61°N and 40.906°E with elevation of 451 m and represents an A quality station. A total of 155 receiver functions have been stacked. There is a clear positive phase at ~ 5 s in the back-azimuth of 30° (Figure 6.5.a). The peak becomes weaker between the ranges of 40°-100° with the arrival times from 3.2 s to 3.5 s. The back-azimuth range of 190°-260° shows a strong arrival of PmS phase that is observed at 3.5 s to 3.8 s after the direct P-wave. Most of the events originated from east with few events back azimuth coverage from the northwest (Figure 6.5.b). From the H-k plot, a well defined peak can be observed which is marked by the black dot (Figure 6.5.c). The resulting optimal Moho depth is 25.33±0.11 km, the corresponding V_p/V_s is 1.988±0.004 and the resulting R value is 0.128±0.01.

6.2 THE TG STATIONS

The crustal thickness beneath these stations ranging from 23.49±0.17 km (AD08) to 27.40±0.47 km at AD09. The Φ values range from 1.921 at AD06 to 2.071 at AD08, both are A category stations. The R values observed are from 0.017 (AD09) to 0.302 (AD10).

AD06: The station is located at 11.68°N and 40.94°E with elevation of 460 m and represents a B quality station. A total of 86 receiver functions have been stacked. The amplitude of PmS phase is weak between the ranges of 40°-110° with the arrival times from about 3 s to 3.2 s. The amplitude of the PmS phases increase for events from the southwest (120°-150°) of the station with arrival times vary from about 2.5 s to over 3.7 s. The back-azimuth range of 200°-260° shows an arrival of this phase that is observed at 3.5 s to

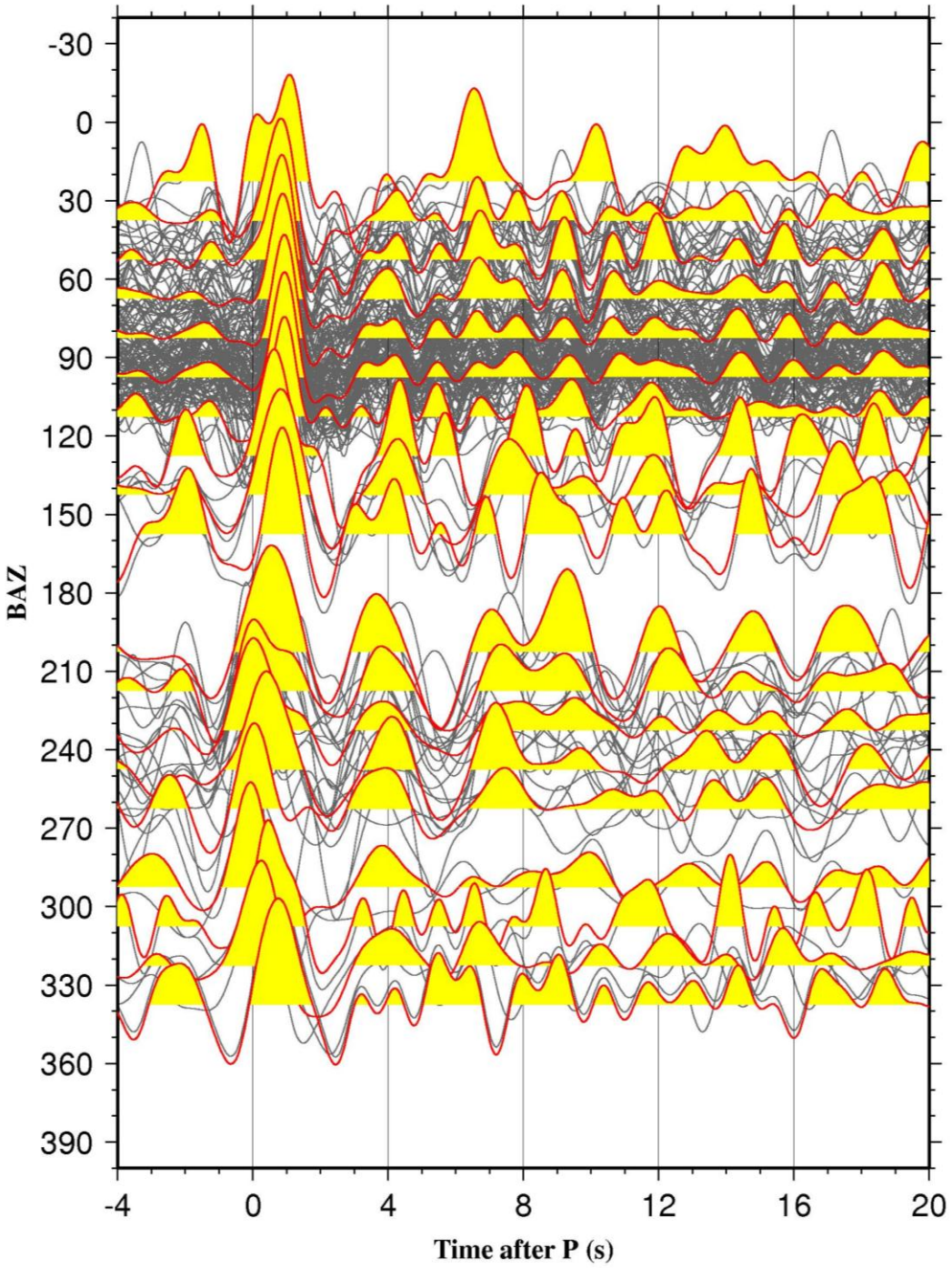

Figure 6.5. (a) Radial receiver functions plotted against the back-azimuth (BAZ) for AD05. Gray thin lines are individual RFs, and red thick lines are stacked RFs in 15° azimuthal bins.

b)

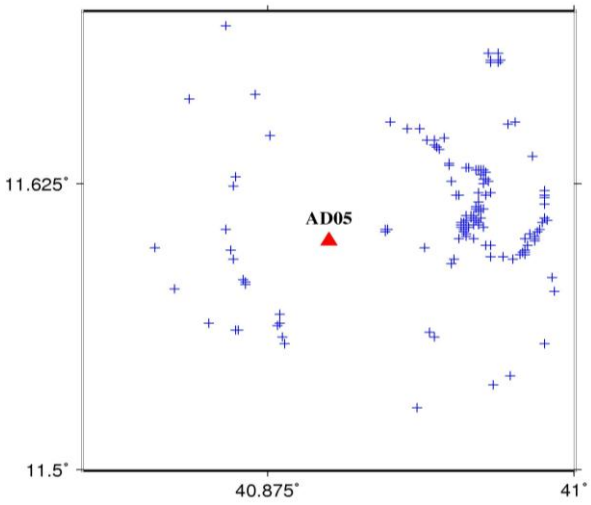

c)

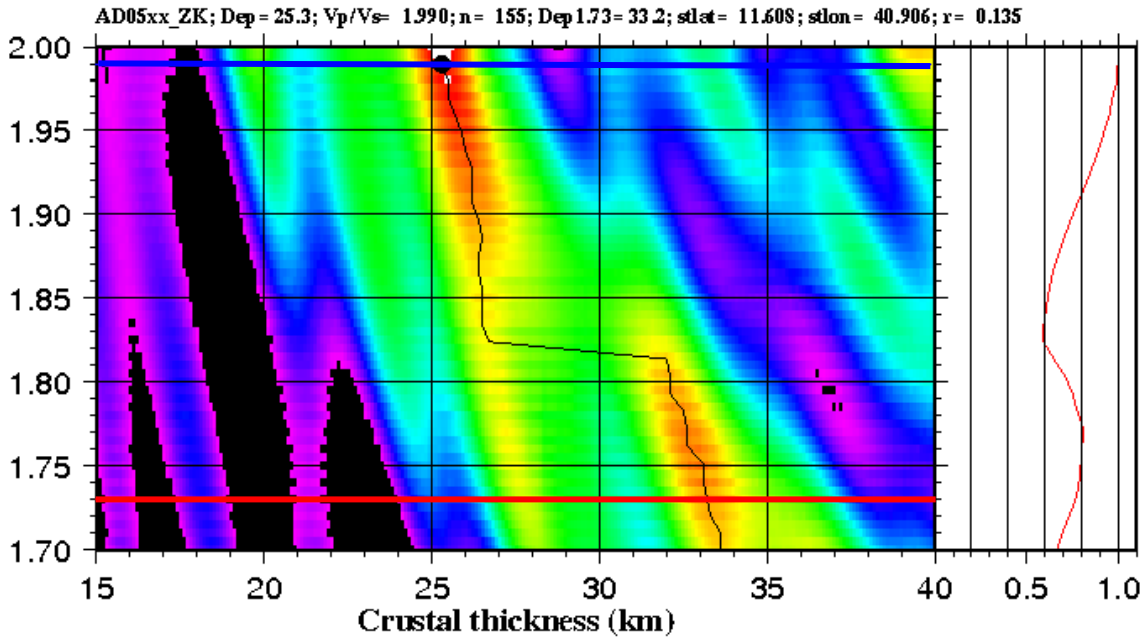

Figure 6.5. (Continued) (b) The distribution of ray-piercing points of the PmS phase for AD05. (c) H-k plots for station AD05. The red line shows the stacking amplitude for Φ=1.73. The blue line was obtained using the optimal Φ.

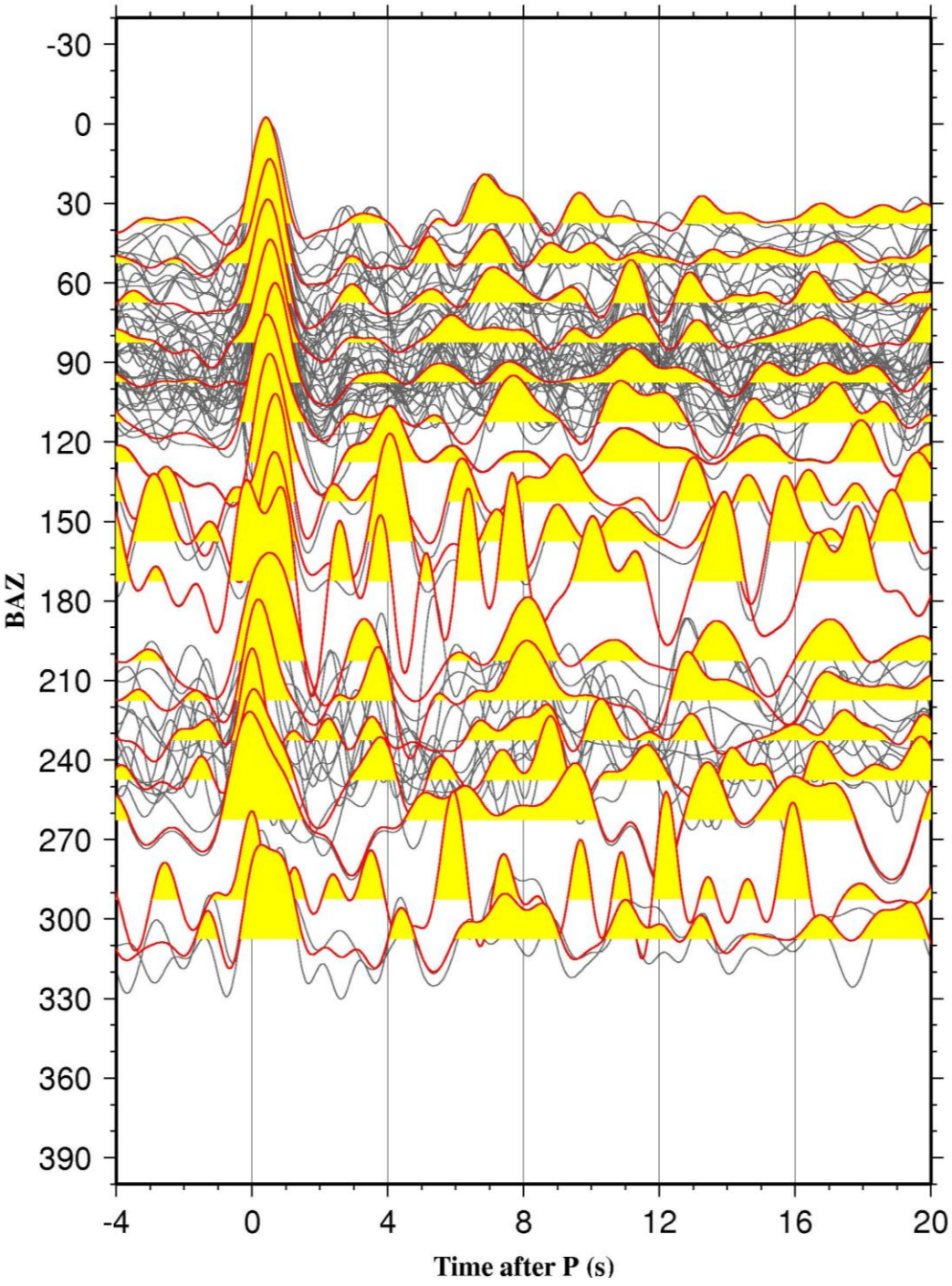

Figure 6.6. (a) Radial receiver functions plotted against the back-azimuth (BAZ) for AD06. Gray thin lines are individual RFs, and red thick lines are stacked RFs in 15° azimuthal bins.

b)

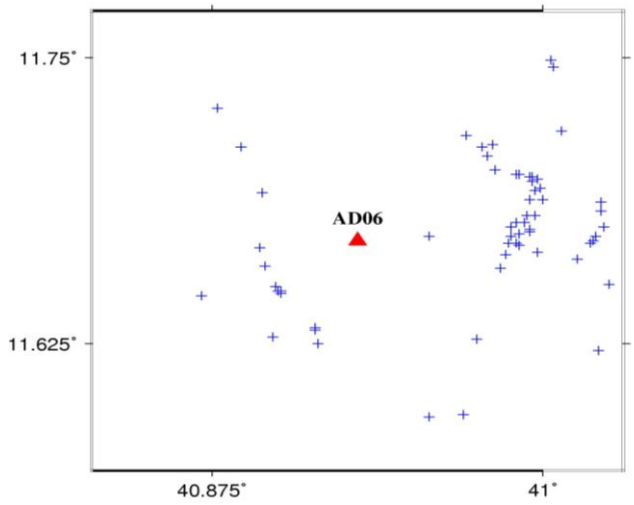

c)

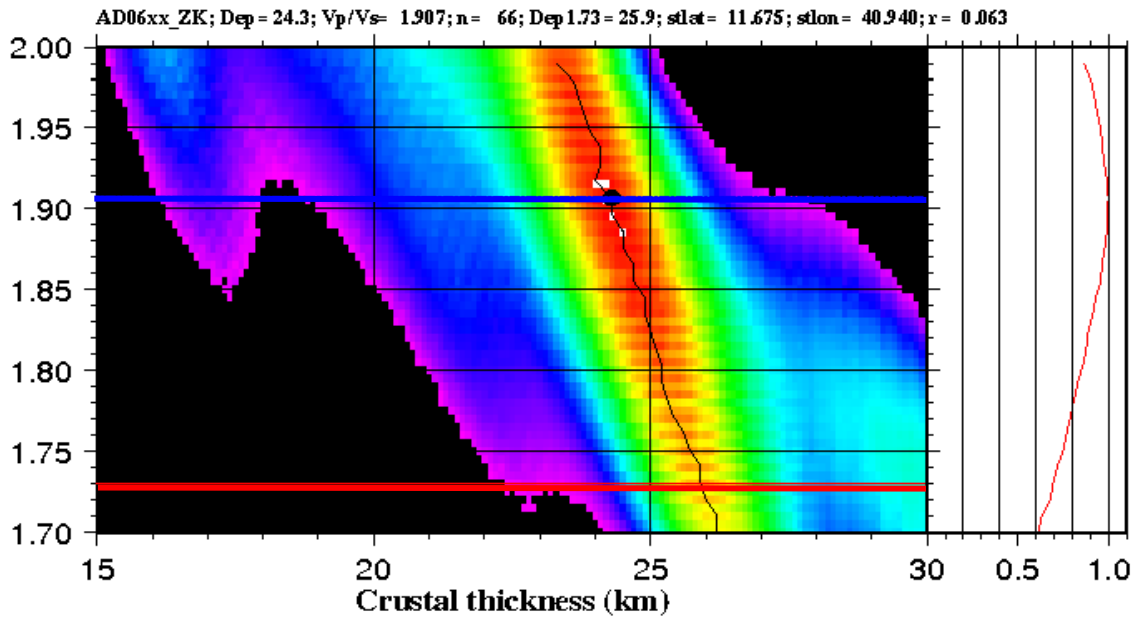

Figure 6.6. (Continued) (b) The distribution of ray-piercing points of the PmS phase for AD06. (c) H-k plots for station AD06. The red line shows the stacking amplitude for Φ=1.73. The blue line was obtained using the optimal Φ.

3.7 s after the direct P-wave (Figure 6.6.a). The ray-piercing points are mainly distributed in the east and northeast and some are in the northwest directions (Figure 6.6.b). From the H-k plot, a well defined peak can be observed which is marked by the black dot (Figure 6.6.c). The resulting optimal Moho depth is 24.15±0.33 km and the resulting R value is 0.066±0.015.

AD07: The station is located at 11.73°N and 40.99°E with elevation of 395 m and represents a B quality station. A total of 90 receiver functions have been stacked. The first positive peaks of PmS phase on the radial receiver function can be observed from ~ 3 s and 3.3 s in the back-azimuth of 40°-155° (Figure 6.7.a). The amplitude becomes larger between the ranges of 200°-245° with the arrival times from 3.1 s to 3.3 s. The back-azimuth range of 190°-260° shows a strong arrival of PmS phase that is observed at 3.8 s to 5 s after the direct P-wave. Most of the events originated from the north-east with few events back azimuth coverage from the northwest (Figure 6.7.b). From the H-k plot, a well defined peak can be observed which is marked by the black dot (Figure 6.7.c). The resulting optimal Moho depth is 24.29±0.21 km and the resulting R value is 0.32±0.021.

AD08: The station is located at 11.78°N and 41.03°E with elevation of 391 m and represents an A quality station. We have been able to stack 604 receiver functions using data from this and two other seismic stations belong to YZ and ZE networks. A strong arrival of PmS phase is observed clearly along most of the back-azimuth range for this station. The arrival times are mainly observed in the range of 3.5 s and 3.7 s (Figure 6.8.a). Most of the events

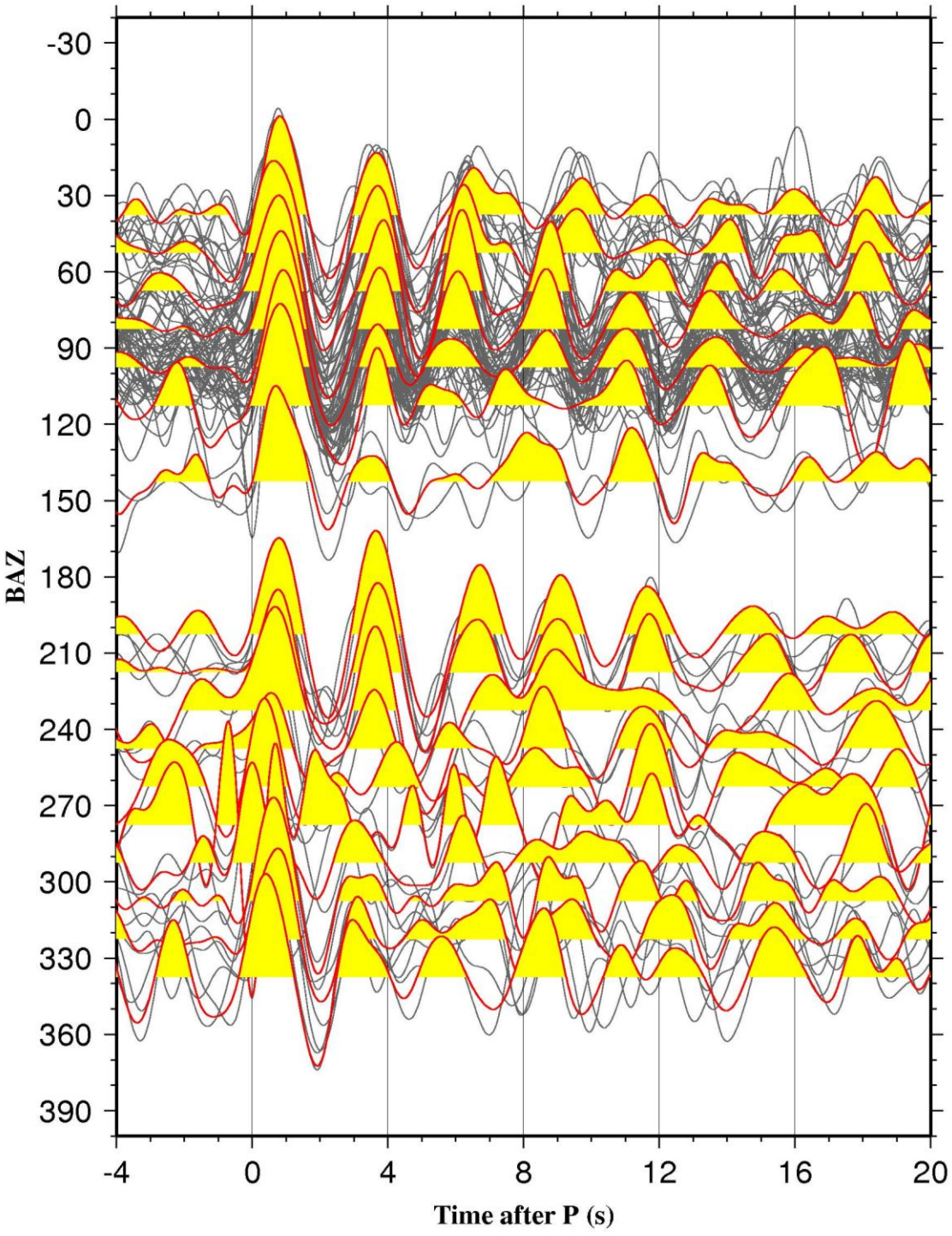

Figure 6.7. (a) Radial receiver functions plotted against the back-azimuth (BAZ) for AD07. Gray thin lines are individual RFs, and red thick lines are stacked RFs in 15° azimuthal bins.

b)

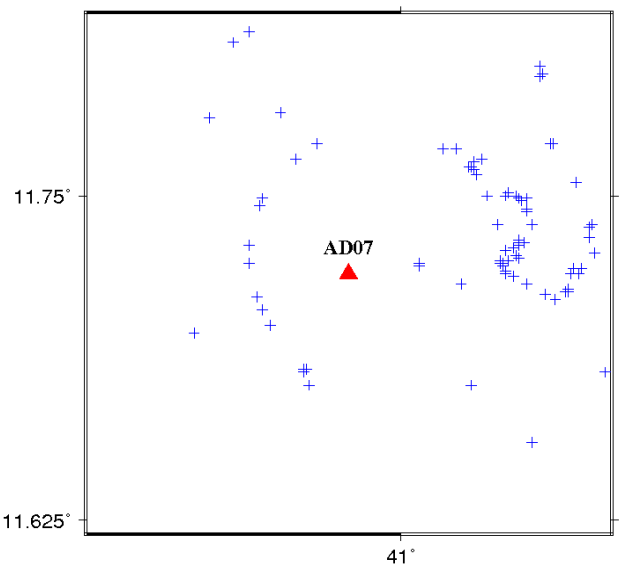

c)

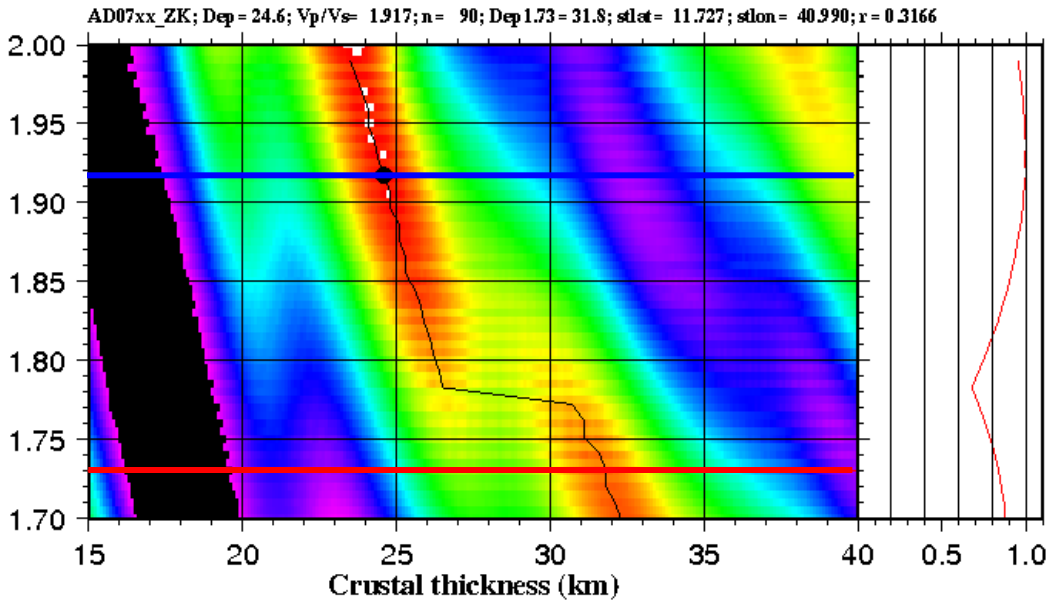

Figure 6.7. (Continued) (b) The distribution of ray-piercing points of the PmS phase for AD07. (c) H-k plots for station AD07. The red line shows the stacking amplitude for Φ=1.73. The blue line was obtained using the optimal Φ.

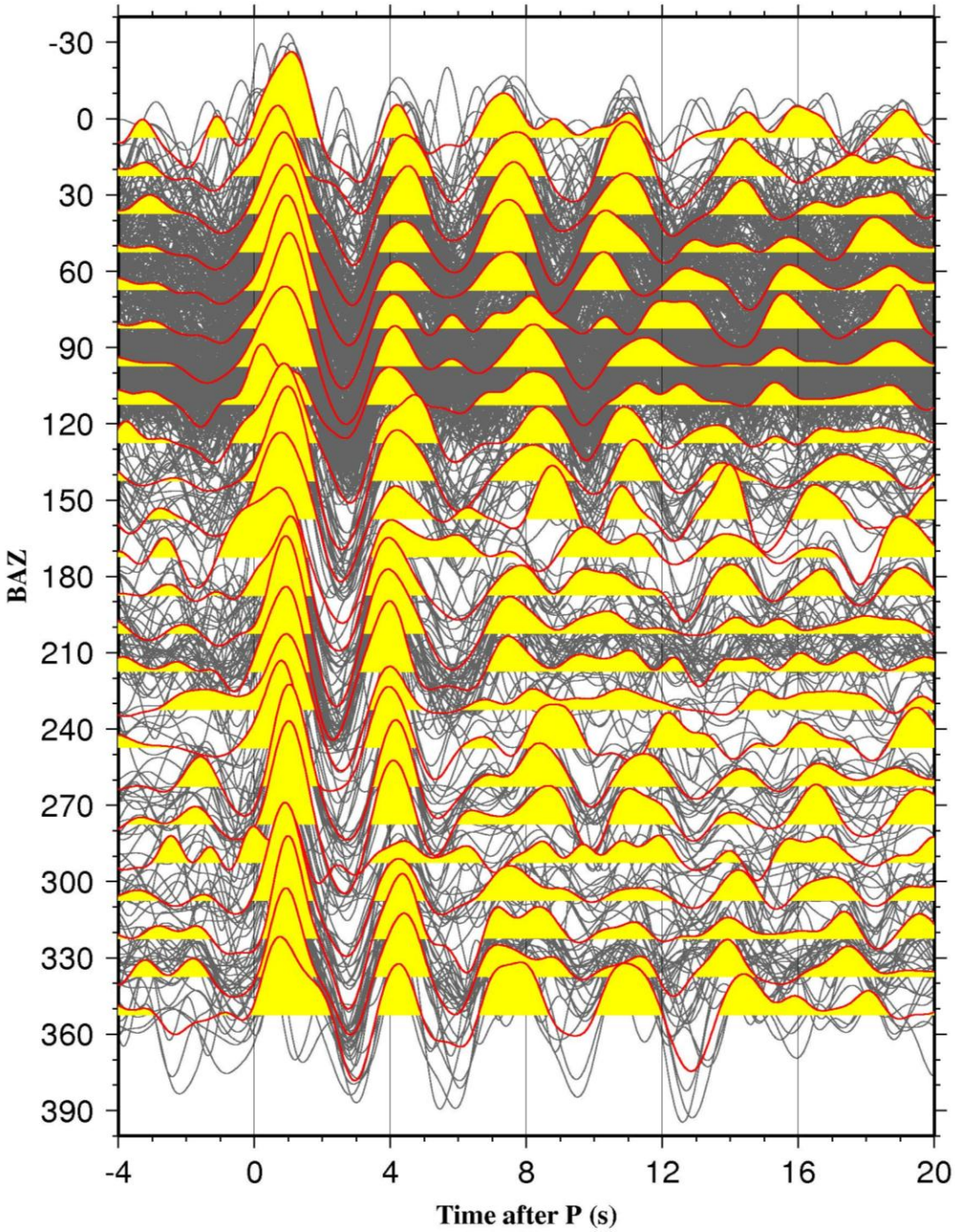

Figure 6.8. (a) Radial receiver functions plotted against the back-azimuth (BAZ) for AD08. Gray thin lines are individual RFs, and red thick lines are stacked RFs in 15° azimuthal bins.

b)

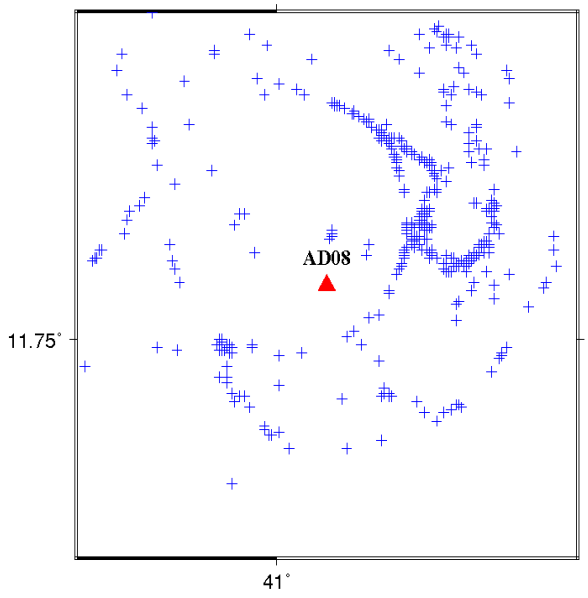

c)

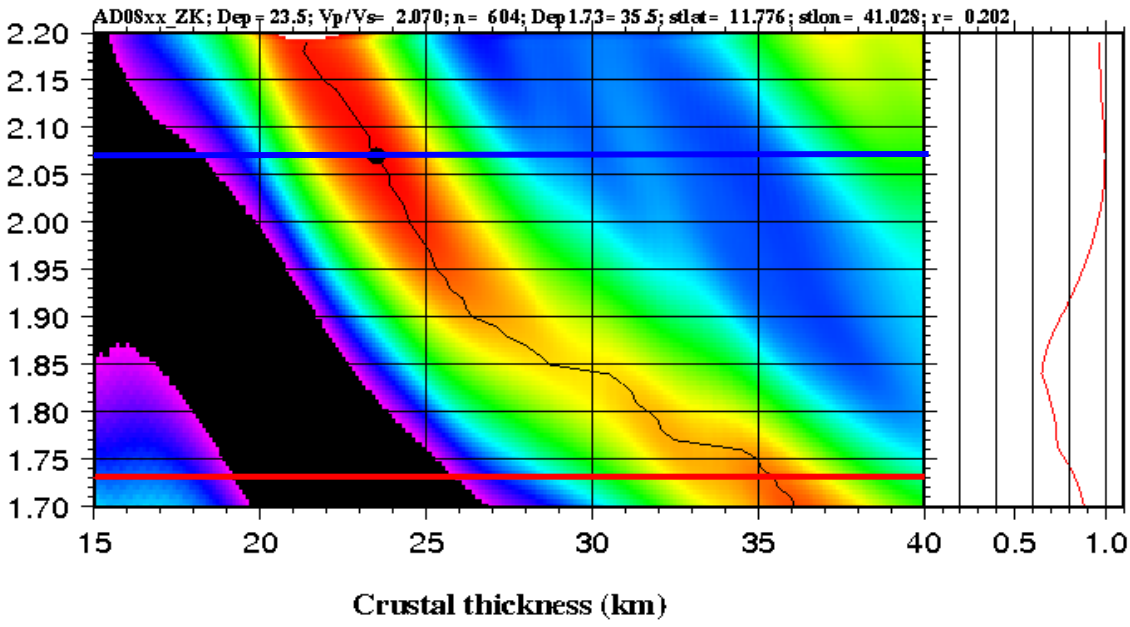

Figure 6.8. (Continued) (b) The distribution of ray-piercing points of the PmS phase for AD08. (c) H-k plots for station AD08. The red line shows the stacking amplitude for Φ=1.73. The blue line was obtained using the optimal Φ.

originated from the northeast and others are from the northwest, southeast, and southwest (Figure 6.8.b). From the H-k plot, a well defined peak can be observed which is marked by the black dot (Figure 6.8.c). The resulting optimal Moho depth is 23.49±0.1 km, the corresponding V_p/V_s is 2.071±0.009 and the resulting R value is 0.20±0.005.

AD09: The station is located at 11.82°N and 41.05°E with elevation of 385 m and represents a B quality station. A total of 90 receiver functions have been stacked. The amplitude of PmS phase is weak between the ranges of 45°-95° with the arrival times from about 3.5 s to 3.8 s (Figure 6.9.a). For the back-azimuth ranges 110°-140°, the amplitude of this phase become larger and can be observed at 3.7 s to 4 s. The ray-piercing points are mainly distributed in the east and northeast (Figure 6.9.b). From the H-k plot, a well defined peak can be observed which is marked by the black dot (Figure 6.9.c). The resulting optimal Moho depth is 27.40±0.47 km and the resulting R value is 0.017±0.009.

AD10: The station is located at 11.80°N and 41.14°E with elevation of 370 m and represents a B category station. A total of 50 receiver functions have been stacked. There is a clear positive phase at ~ 3 s in the back-azimuth of 30°-95° (Figure 6.10.a). The back-azimuth range of 210°-240° shows an arrival of PmS phase that is observed at 2 s to 3.3 s after the direct P-wave. Most of the events originated from the north and the northwest (Figure 6.10.b). From the H-k plot, a well defined peak can be observed which is marked by the black dot (Figure 6.10.c). The resulting optimal Moho depth is 25.95±0.37 km and the resulting R value is 0.301±0.015.

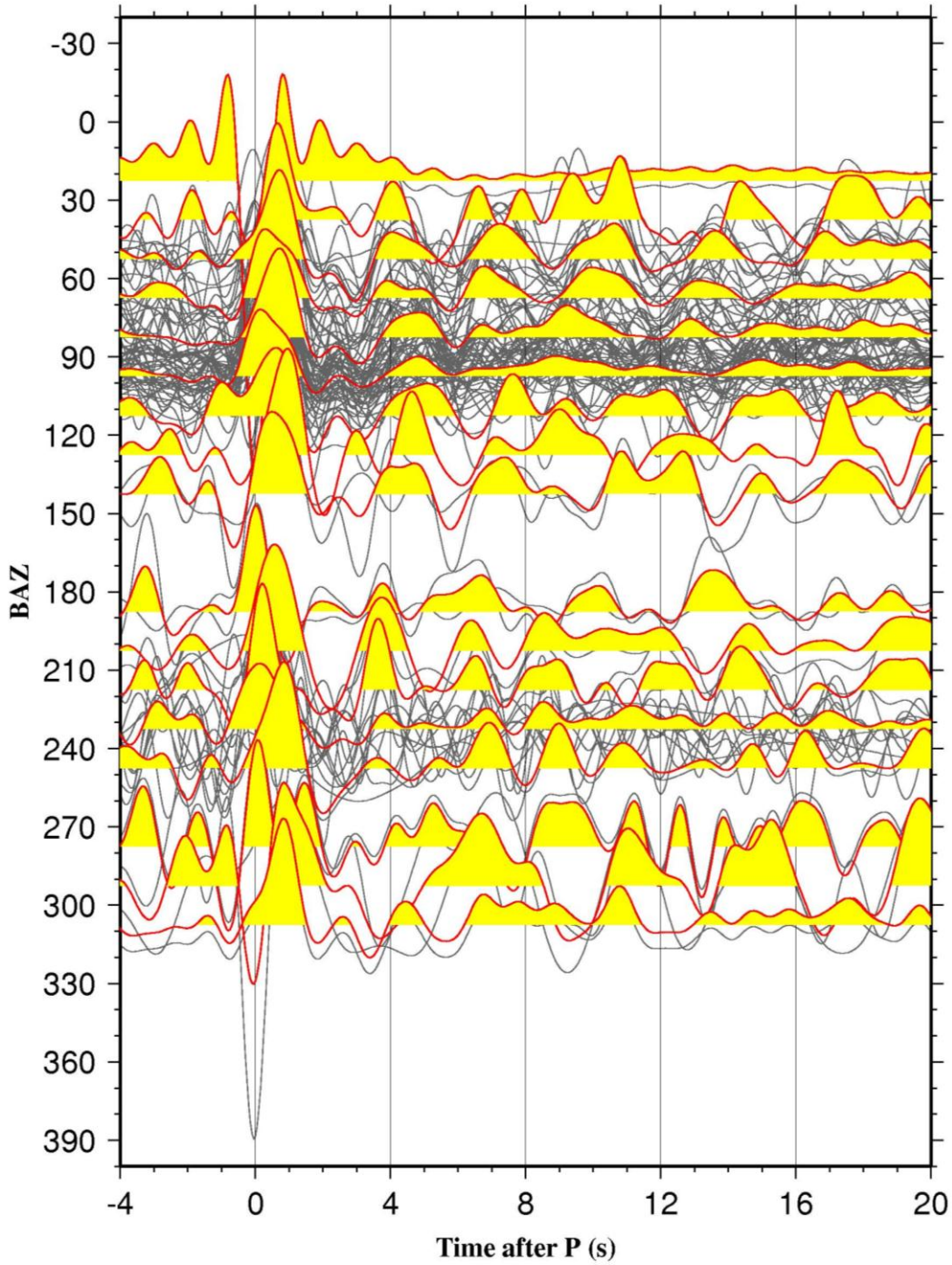

Figure 6.9. (a) Radial receiver functions plotted against the back-azimuth (BAZ) for AD09. Gray thin lines are individual RFs, and red thick lines are stacked RFs in 15° azimuthal bins.

b)

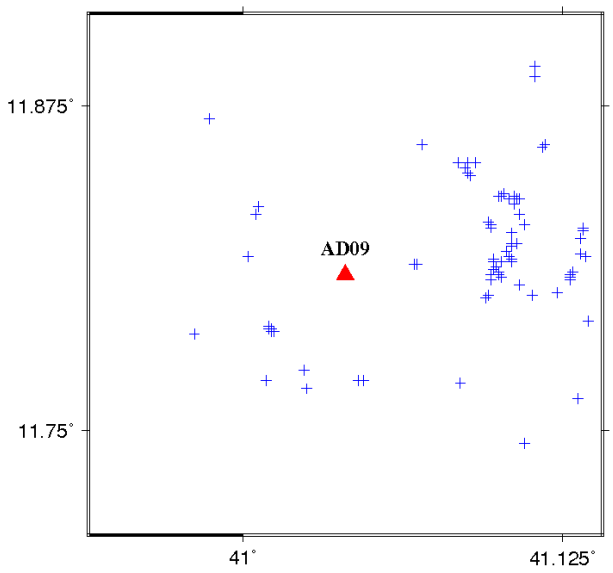

c)

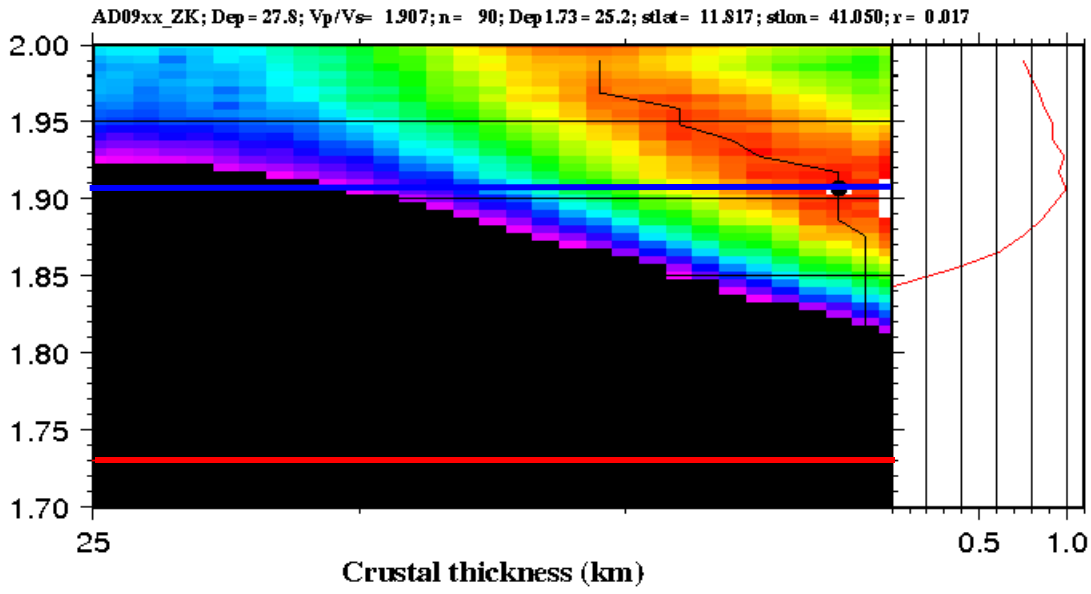

Figure 6.9. (Continued) (b) The distribution of ray-piercing points of the PmS phase for AD09. (c) H-k plots for station AD09. The red line shows the stacking amplitude for Φ=1.73. The blue line was obtained using the optimal Φ.

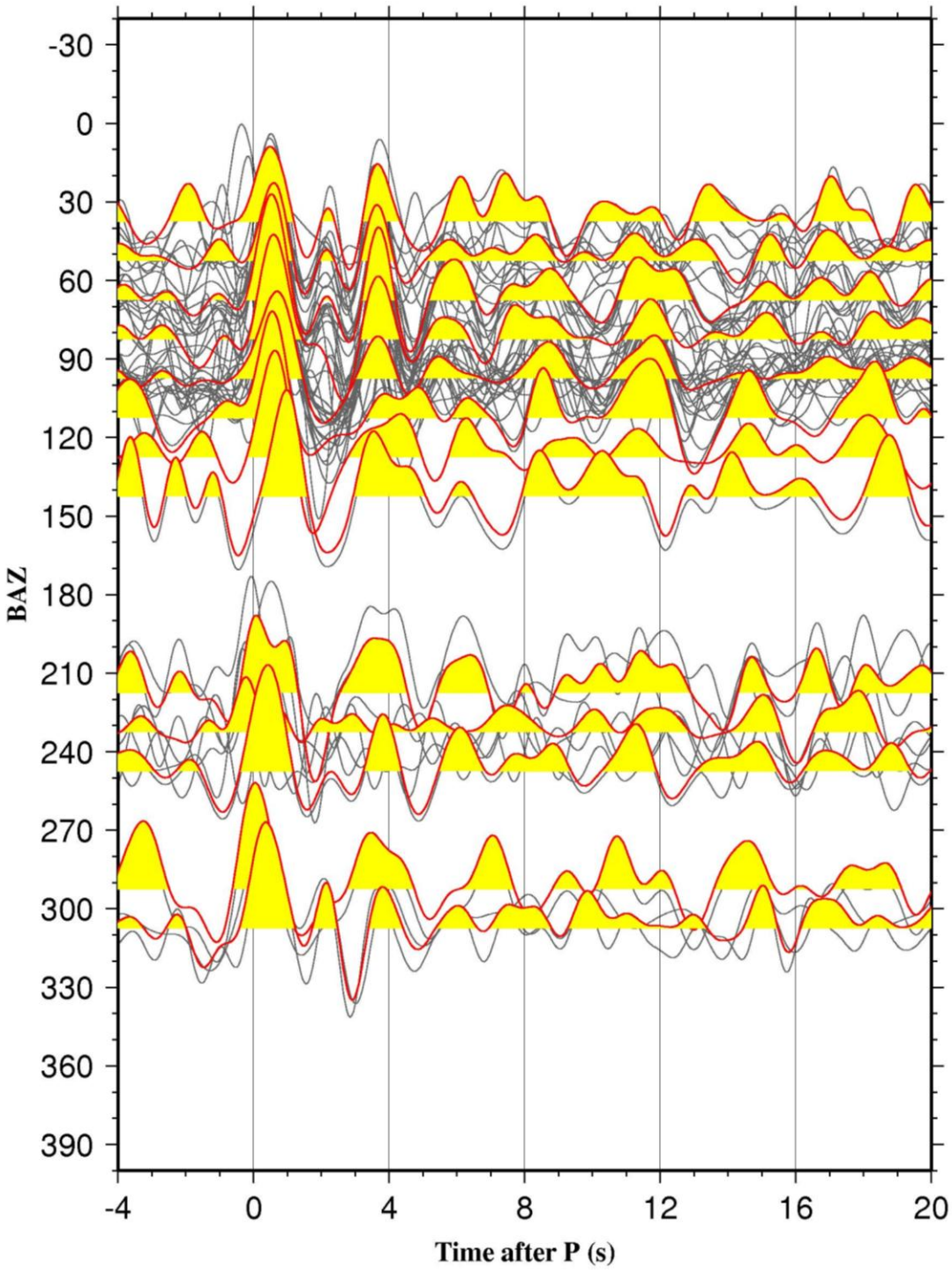

Figure 6.10. (a) Radial receiver functions plotted against the back-azimuth (BAZ) for AD10. Gray thin lines are individual RFs, and red thick lines are stacked RFs in 15° azimuthal bins

b)

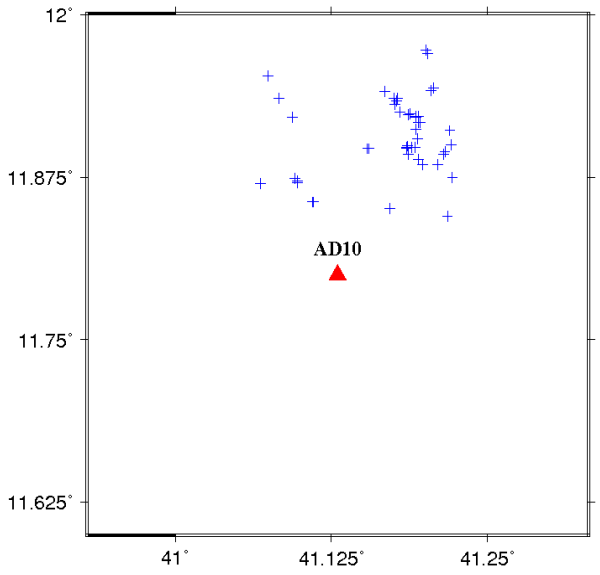

c)

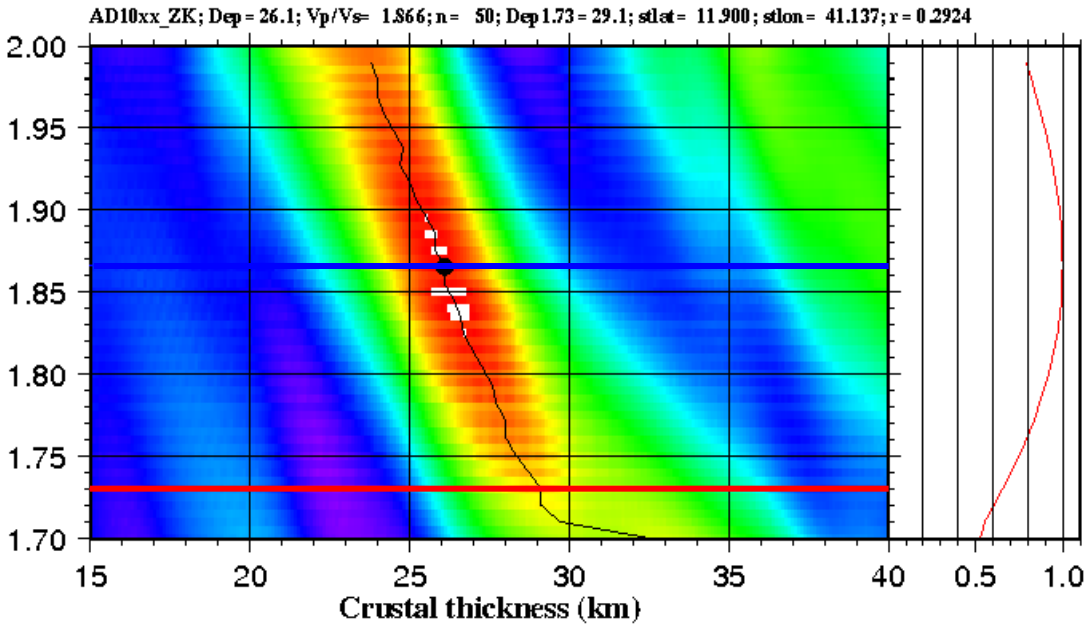

Figure 6.10. (Continued) (b) The distribution of ray-piercing points of the PmS phase for AD10. (c) H-k plots for station AD10. The red line shows the stacking amplitude for Φ=1.73. The blue line was obtained using the optimal Φ.

AD11: The station is located at 11.74°N and 41.30°E with elevation of 370 m and represents a B category station. A total of 109 receiver functions have been stacked. The amplitude of PmS phase can be observed between the ranges of 40°-90° with the arrival times from about 3.7 s to 4 s (Figure 6.11.a). The amplitude of this phase was difficult to identify for events from the southwest and the northwest (210°-320°). The ray-piercing points are mainly distributed in the east and northeast and some are in the northwest (Figure 6.11.b). From the H-k plot, a well defined peak can be observed which is marked by the black dot (Figure 6.11.c). The resulting optimal Moho depth is 27.37±0.15 km and the resulting R value is 0.257±0.023.

AD13: The station is located at 11.96°N and 41.31°E with elevation of 352 m and represents an A quality station. A total of 97 receiver functions have been stacked. The peak of PmS phases are weak between the ranges of 20°-50° (Figure 6.12.a). The same phase can be observed clearly from 3 s to 3.5 s in the back-azimuth range of 70°-110°. Most of the events originated from the north-east, east with few events back azimuth coverage from the southwest (Figure 6.12.b). From the H-k plot, a well defined peak can be observed which is marked by the black dot (Figure 6.12.c). The resulting optimal Moho depth is 25.37±0.68 km, the corresponding V_p/V_s is 1.948±0.027 and the resulting R value is 0.127±0.011.

6.3 THE DG AND THE ADJACENT HORSTS STATIONS

The stations are characterized by crustal thickness between 27.64 (AD14) and 31.99 (AD18) km and Φ values between 1.870 (AD19) and 1.984

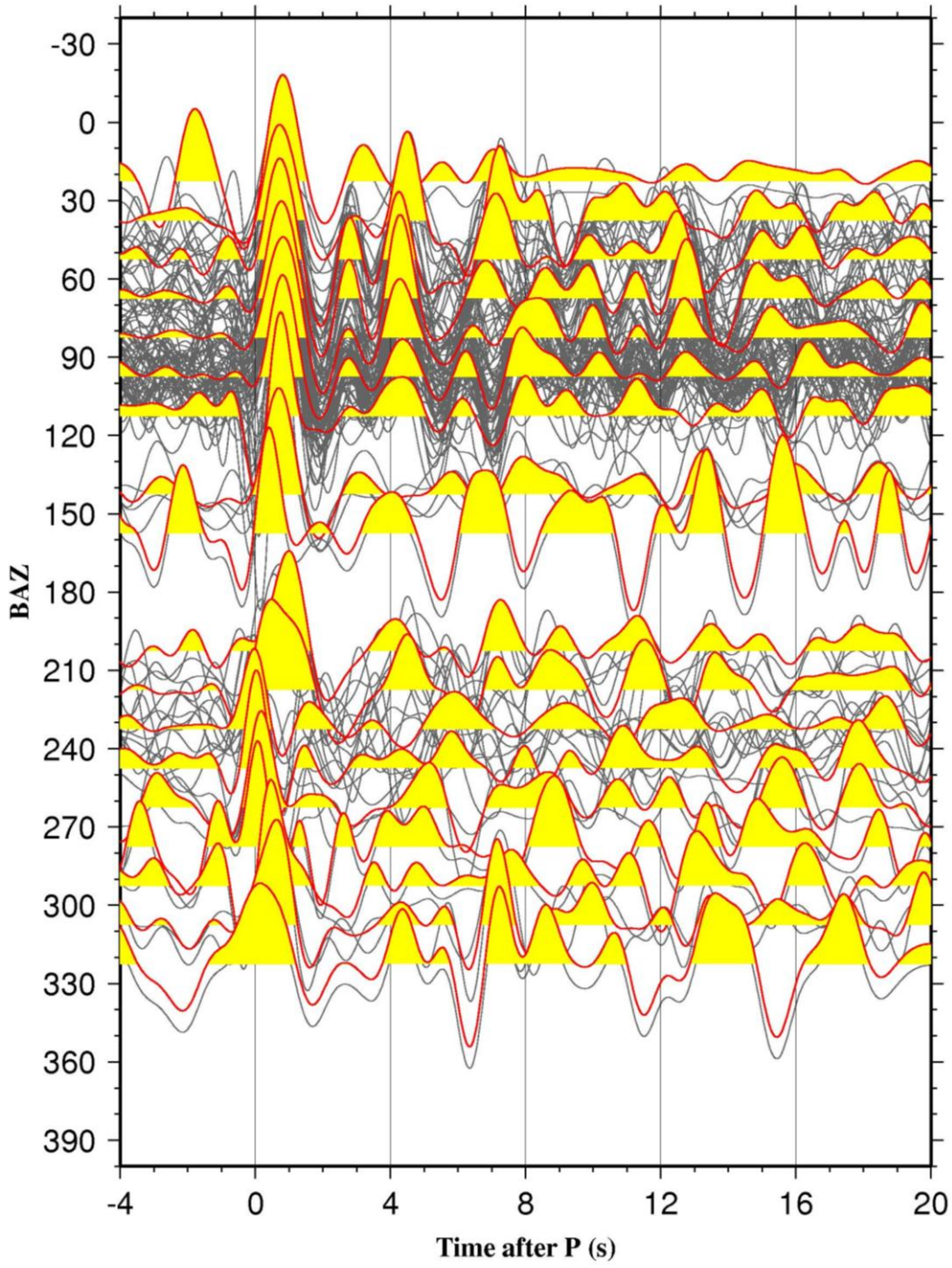

Figure 6.11. (a) Radial receiver functions plotted against the back-azimuth (BAZ) for AD11. Gray thin lines are individual RFs, and red thick lines are stacked RFs in 15° azimuthal bins.

b)

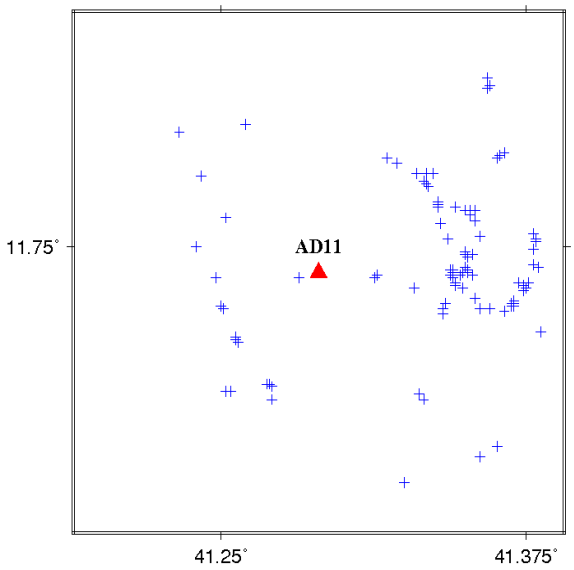

c)

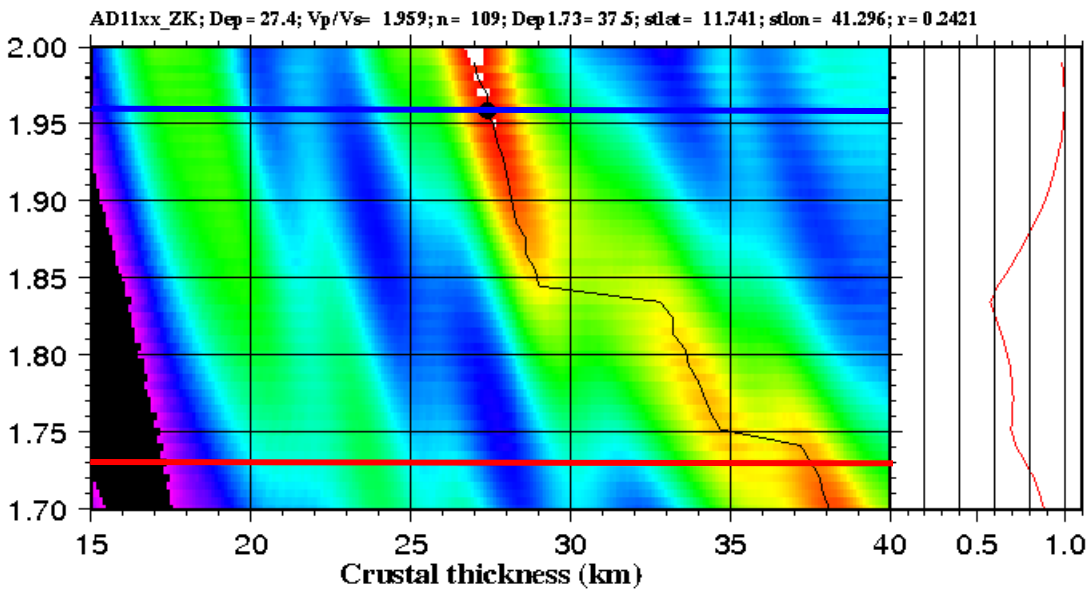

Figure 6.11. (Continued) (b) The distribution of ray-piercing points of the PmS phase for AD11. (c) H-k plots for station AD11. The red line shows the stacking amplitude for Φ=1.73. The blue line was obtained using the optimal Φ.

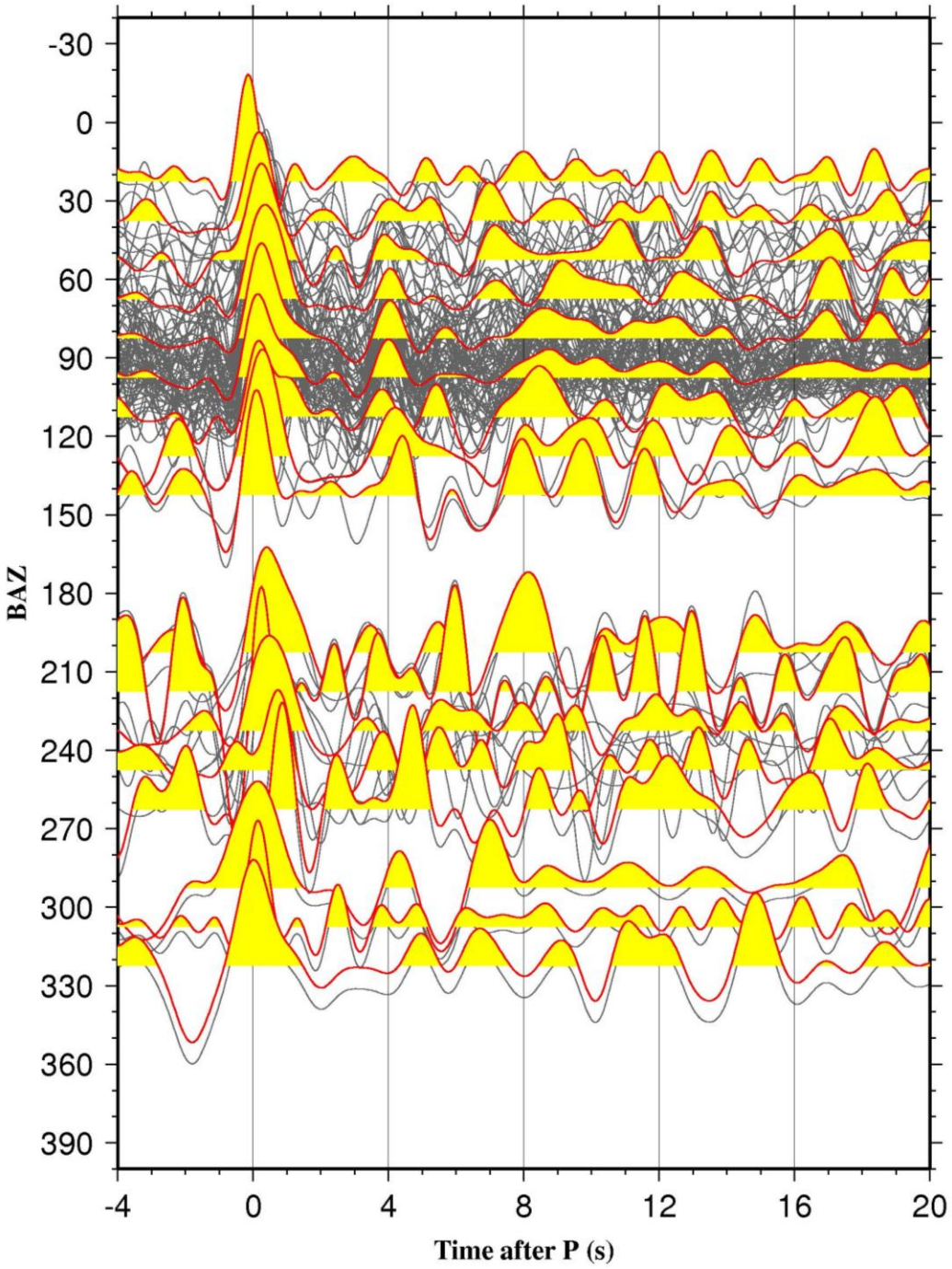

Figure 6.12. (a) Radial receiver functions plotted against the back-azimuth (BAZ) for AD13. Gray thin lines are individual RFs, and red thick lines are stacked RFs in 15° azimuthal bins.

b)

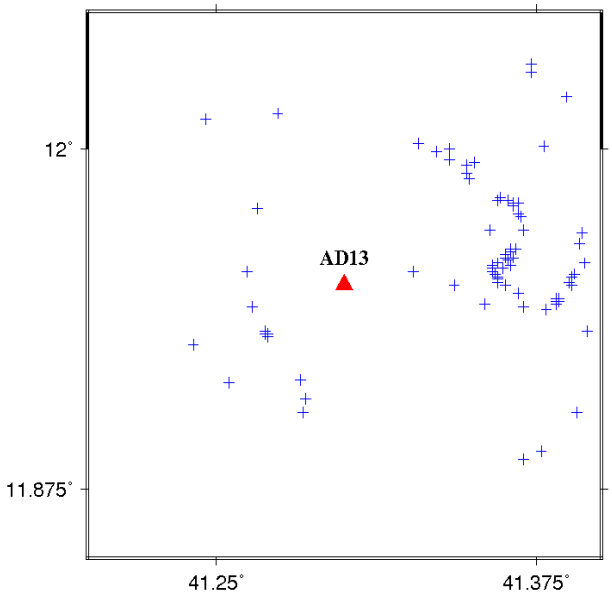

c)

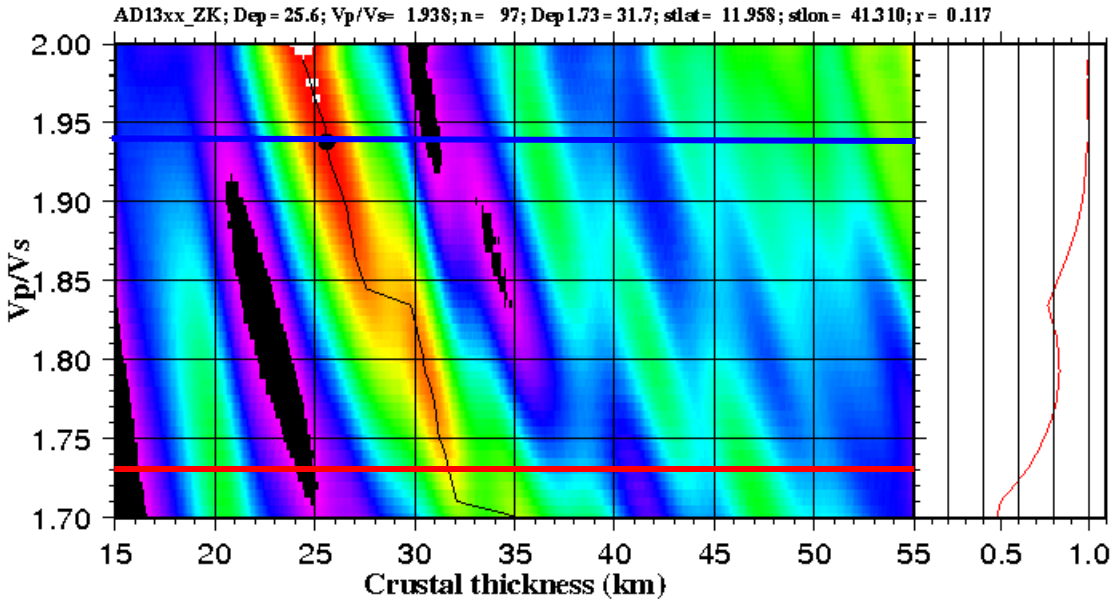

Figure 6.12. (Continued) (b) The distribution of ray-piercing points of the PmS phase for AD13. (c) H-k plots for station AD13. The red line shows the stacking amplitude for Φ=1.73. The blue line was obtained using the optimal Φ.

(AD14). The amplitude ratios (R) ranging from 0.068 (AD19) to 0.265 (AD17).

AD14: The station is located at 11.94°N and 41.45°E with elevation of 422 m and represents a B quality station. A total of 72 receiver functions have been stacked. Most of the back-azimuth ranging from 40°-100° shows small arrivals of PmS phase that are observed at 4 s to 5.2 s after the direct P-wave (Figure 6.13.a). The amplitude of the same phases increases after ~ 4 s, for the same back azimuth range. Most of the events originated from the north-east, east with few events back azimuth coverage from the northwest (Figure 6.13.b). From the H-k plot, a well defined peak can be observed which is marked by the black dot (Figure 6.13.c). The resulting optimal Moho depth is 27.64±0.25 km and the resulting R value is 0.13±0.011.

AD15: The station is located at 11.88°N and 41.71°E with elevation of 88 m and represents an A quality station. A total of 28 receiver functions have been stacked. The first positive peak of PmS on the radial receiver function can be observed from ~ 3-3.8 s in the back-azimuth of 40°-110° (Figure 6.14.a). The peak becomes weaker between the ranges of 220°-290°. Most of the events originated from the east and southwest (Figure 6.14.b). From the H-k plot, a well defined peak can be observed which is marked by the black dot (Figure 6.14.c). The resulting optimal Moho depth is 30.46±0.4 km, the corresponding V_p/V_s is 1.878±0.033 and the resulting R value is 0.12±0.021.

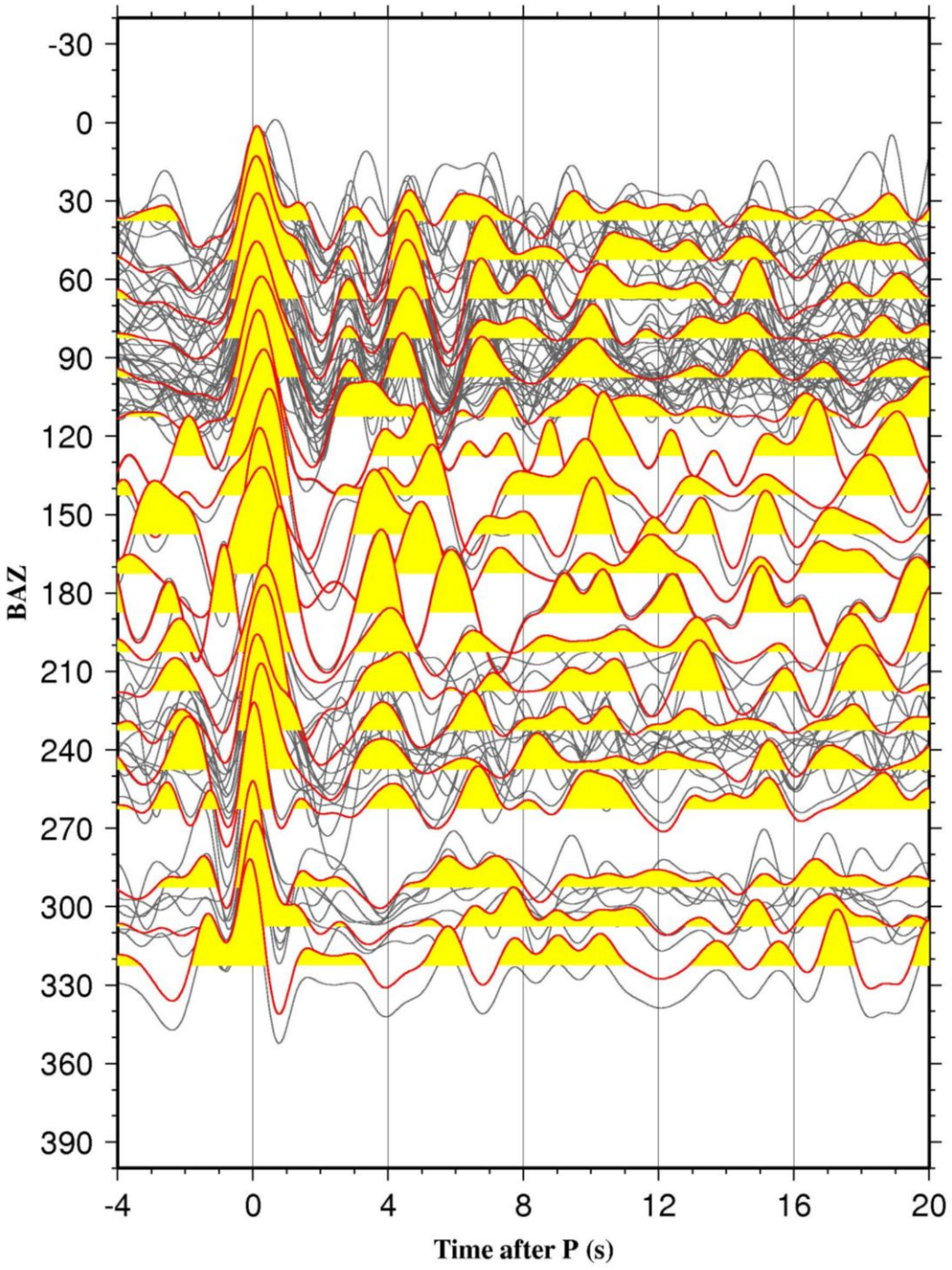

Figure 6.13. (a) Radial receiver functions plotted against the back-azimuth (BAZ) for AD14. Gray thin lines are individual RFs, and red thick lines are stacked RFs in 15° azimuthal bins

b)

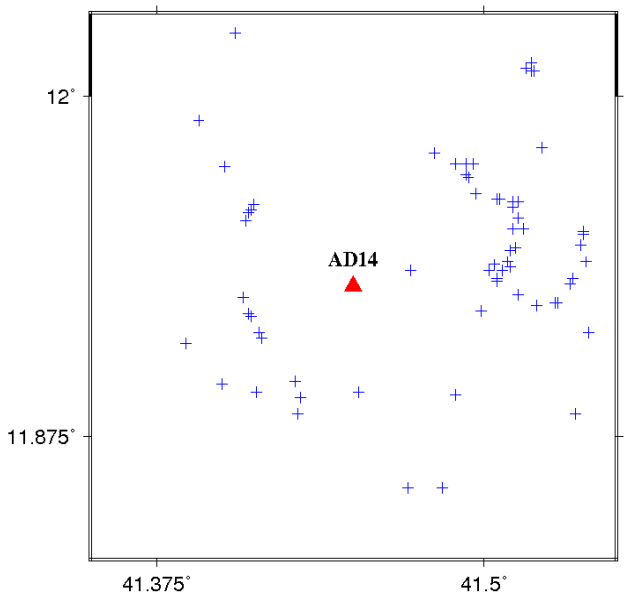

c)

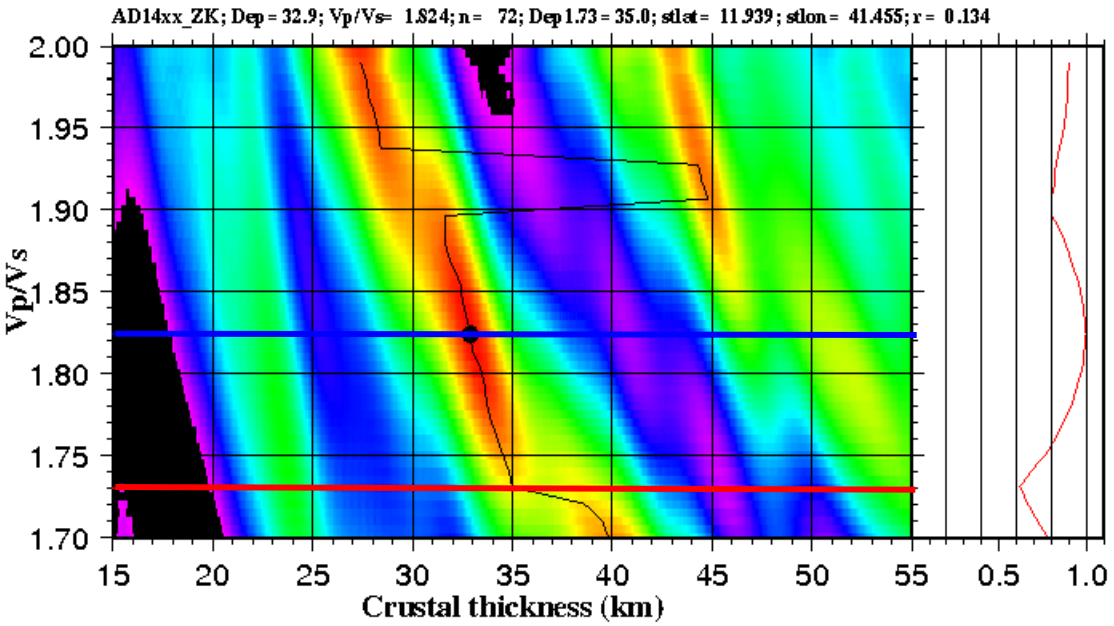

Figure 6.13. (Continued) (b) The distribution of ray-piercing points of the PmS phase for AD14. (c) H-k plots for station AD14. The red line shows the stacking amplitude for Φ=1.73. The blue line was obtained using the optimal Φ.

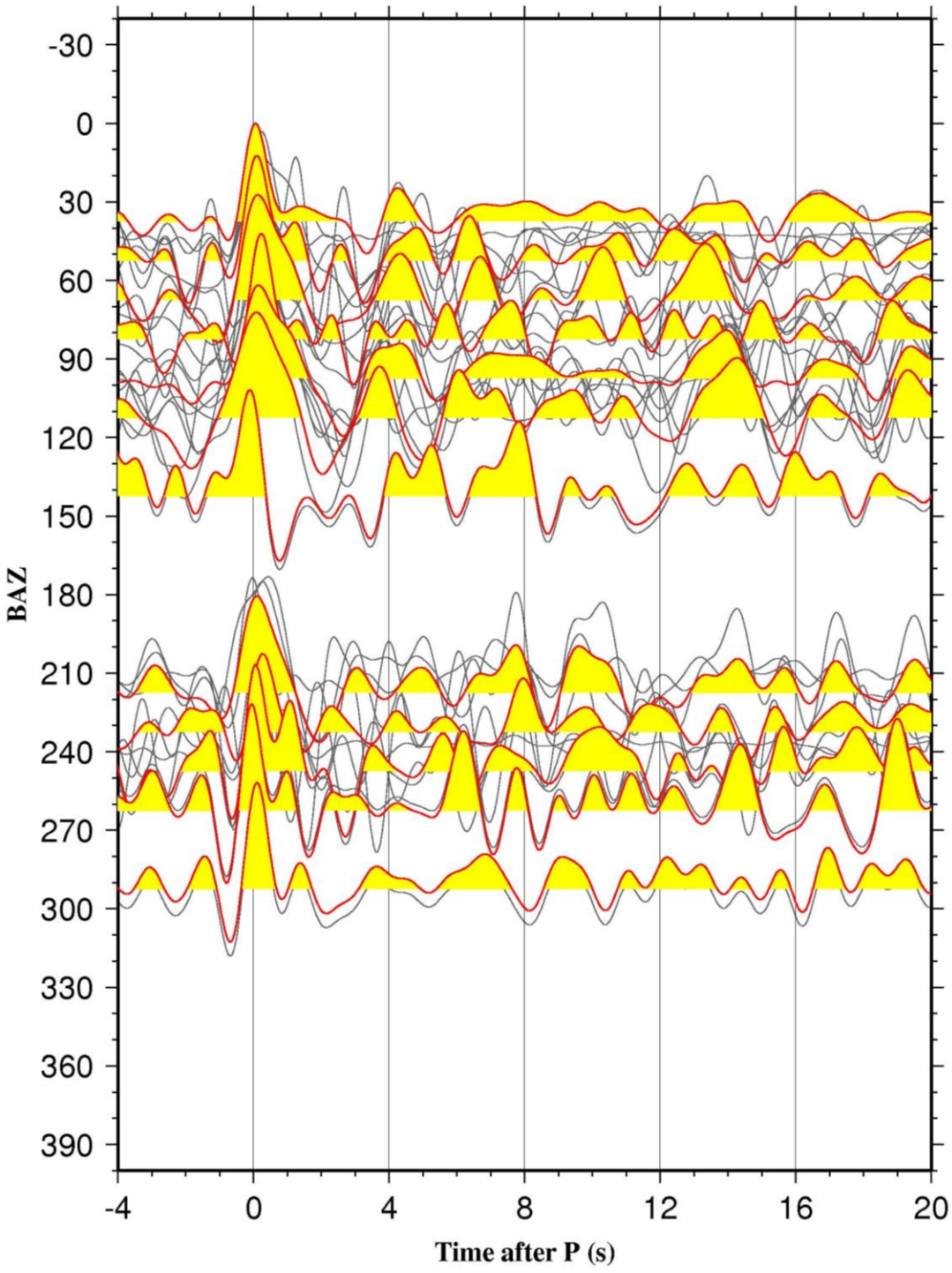

Figure 6.14. (a) Radial receiver functions plotted against the back-azimuth (BAZ) for AD15. Gray thin lines are individual RFs, and red thick lines are stacked RFs in 15° azimuthal bins

b)

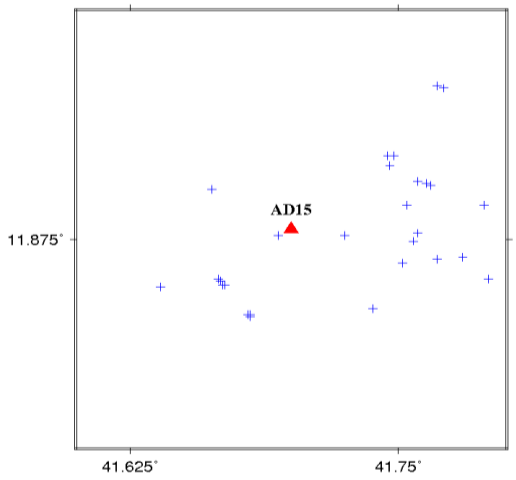

c)

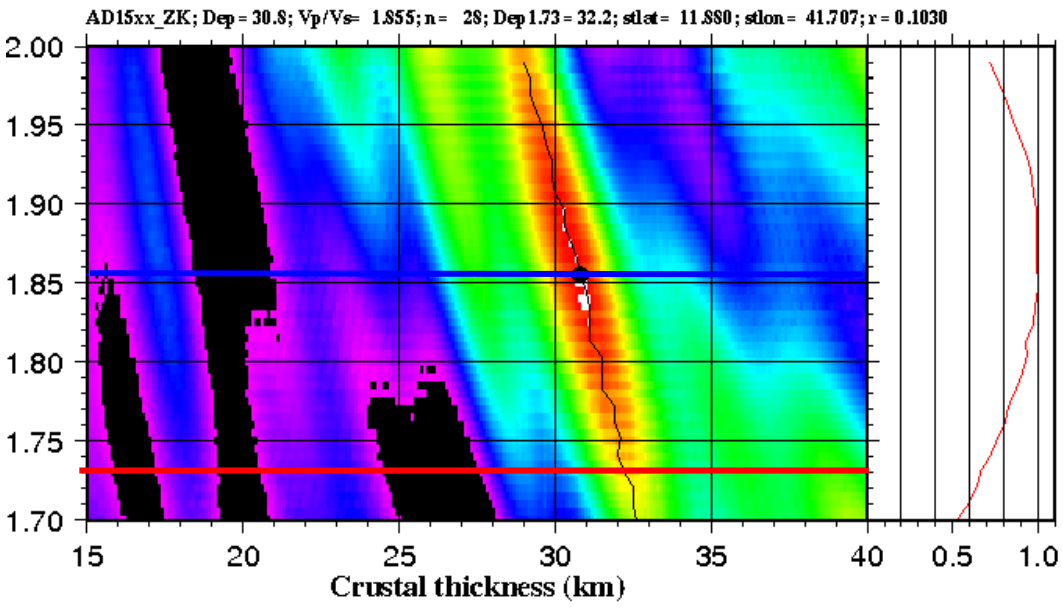

Figure 6.14. (Continued) (b) The distribution of ray-piercing points of the PmS phase for AD15. (c) H-k plots for station AD15. The red line shows the stacking amplitude for Φ=1.73. The blue line was obtained using the optimal Φ.

AD16: The station is located at 11.82°N and 41.75°E with elevation of 118 m and it represents an A quality station. A total of 62 receiver functions have been stacked. Most of the back-azimuth ranging from 55°-150° shows arrivals of PmS phase that are observed at 3 s to 5 s after the direct P-wave (Figure 6.15.a). Most of the events originated from the east and the northeast (Figure 6.15.b). From the H-k plot, a well defined peak can be observed which is marked by the black dot (Figure 6.15.c). The resulting optimal Moho depth is 30.68±0.28 km, the corresponding V_p/V_s is 1.895±0.018 and the resulting R value is 0.146±0.013.

AD17: The station is located at 11.74°N and 41.84°E with elevation of 150 m and represents an A quality station. A total of 54 receiver functions have been stacked. The amplitude of PmS phase is show small amplitudes between the ranges of 40°-140° with the arrival times from about 2 s to 2.5 s (Figure 6.16.a). For the same back-azimuth ranges, strong Pms phases arrival are observed at 3.7 s to 5 s. The small-amplitude phases that arrive before the Pms phases might represent P-to-S conversions within the crust. The amplitude of the PmS phases for events from the southwest (200°-235°) of the station arrive between 2 s to 3 s. The ray-piercing points are mainly distributed in the east and the southwest directions (Figure 6.16.b). From the H-k plot, a well defined peak can be observed which is marked by the black dot (Figure 6.16.c). The resulting optimal Moho depth is 29.04±0.12 km, the corresponding V_p/V_s is 1.981±0.006 and the resulting R value is 0.256±0.026.

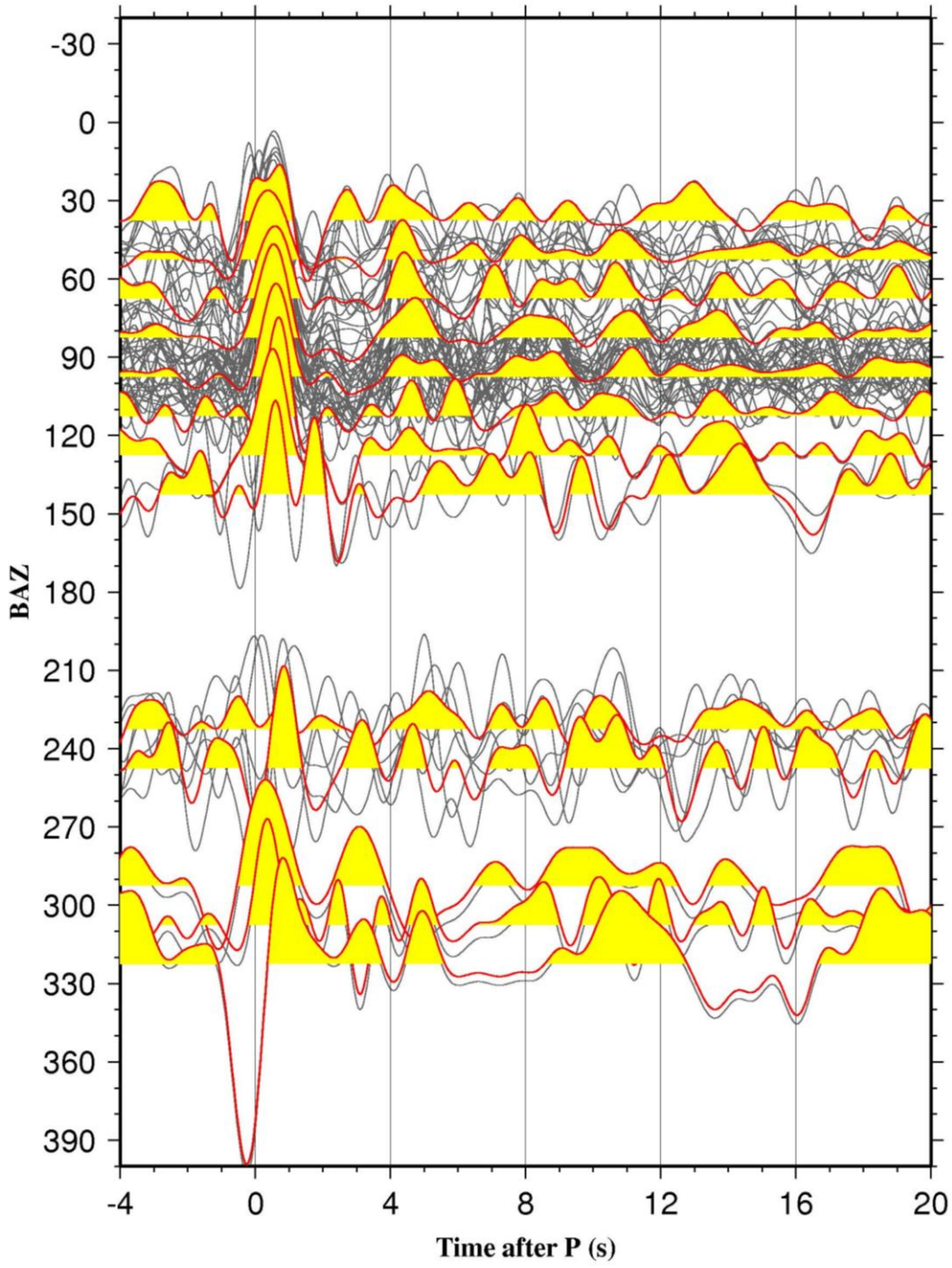

Figure 6.15. (a) Radial receiver functions plotted against the back-azimuth (BAZ) for AD16. Gray thin lines are individual RFs, and red thick lines are stacked RFs in 15° azimuthal bins

b)

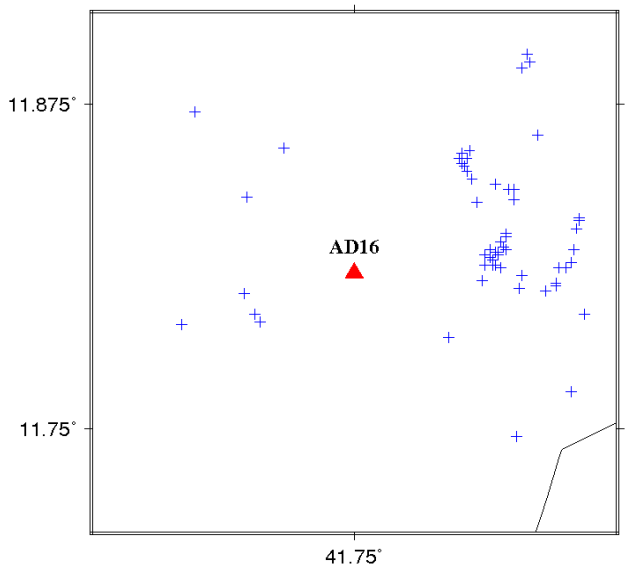

c)

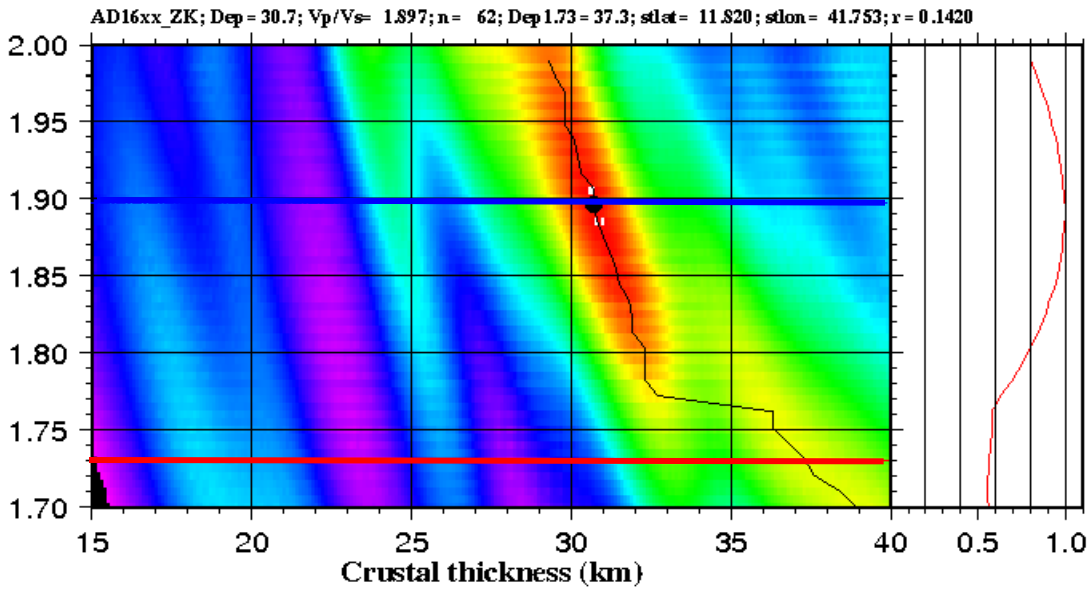

Figure 6.15. (Continued) (b) The distribution of ray-piercing points of the PmS phase for AD16. (c) H-k plots for station AD16. The red line shows the stacking amplitude for Φ=1.73. The blue line was obtained using the optimal Φ.

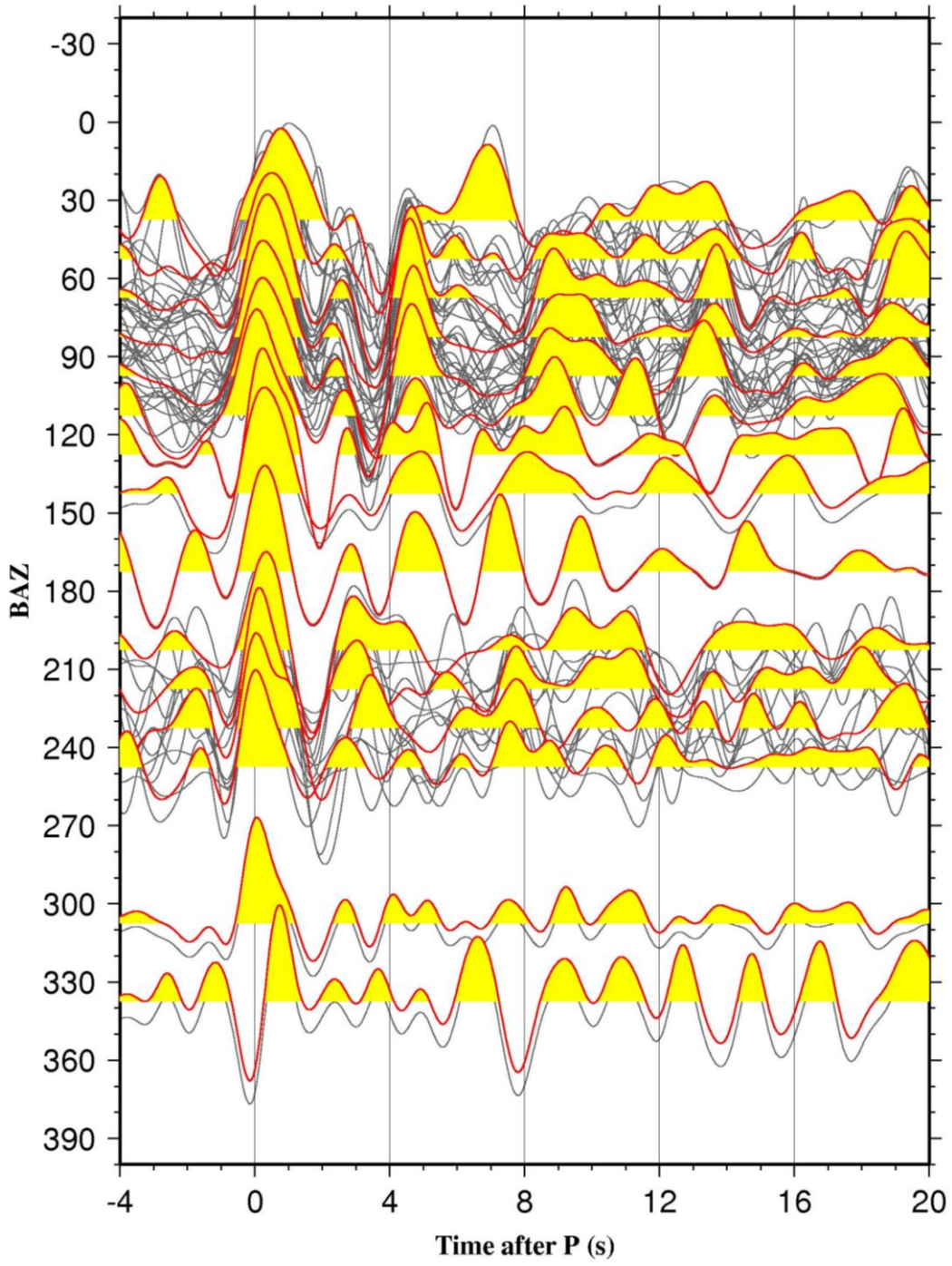

Figure 6.16. (a) Radial receiver functions plotted against the back-azimuth (BAZ) for AD17. Gray thin lines are individual RFs, and red thick lines are stacked RFs in 15° azimuthal bins.

b)

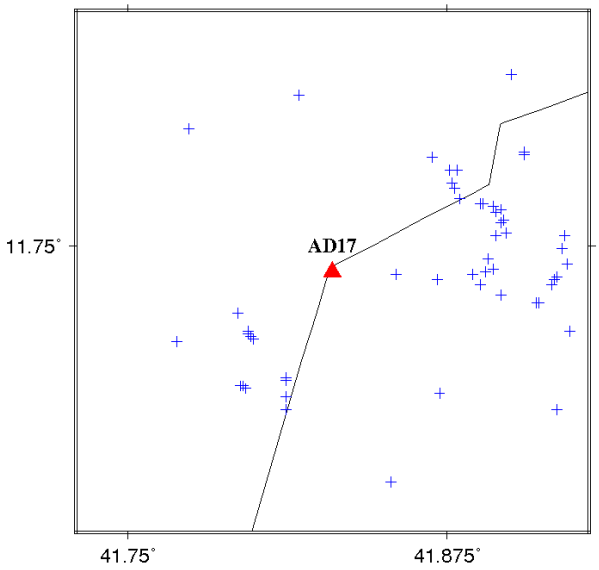

c)

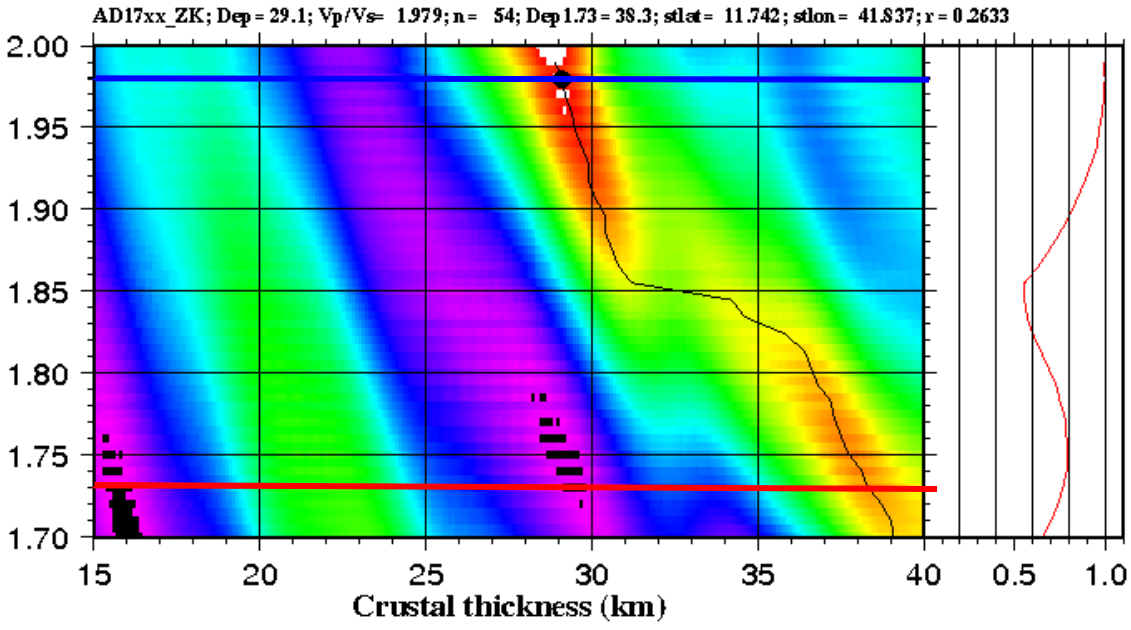

Figure 6.16. (Continued) (b) The distribution of ray-piercing points of the PmS phase for AD17. (c) H-k plots for station AD17. The red line shows the stacking amplitude for Φ=1.73. The blue line was obtained using the optimal Φ.

AD18: The station is located at 11.91°N and 41.79°E with elevation of 452 m and represents an A quality station. A total of 119 receiver functions have been stacked. There is a clear positive phase at ~ 1.5 s in the back-azimuth of 20° (Figure 6.17.a). The peak becomes weaker between the ranges of 70°-100° with the arrival times from 2.5 s to 3 s. The back-azimuth range of 130°-190° shows a strong arrival of PmS phase that is observed at 3 s to 4 s after the direct P-wave. Most of the events originated from east and northeast with few events back azimuth coverage from the southwest (Figure 6.17.b). From the H-k plot, a well defined peak can be observed which is marked by the black dot (Figure 6.17.c). The resulting optimal Moho depth is 31.99±0.26 km, the corresponding V_p/V_s is 1.916±0.019 and the resulting R value is 0.103±0.011.

AD19: The station is located at 12.05°N and 41.93°E with elevation of 435 m and represents a B quality station. A total of 60 receiver functions have been stacked. The amplitude of PmS phase is weak between the ranges of 210°-250° with the arrival times from about 3 s to 4 s (Figure 6.18.a). The ray-piercing points are mainly distributed in the east and northeast and some are in the southwest directions (Figure 6.18.b). From the H-k plot, a well defined peak can be observed which is marked by the black dot (Figure 6.18.c). The resulting optimal Moho depth is 30.52±0.26 km and the resulting R value is 0.068±0.014.

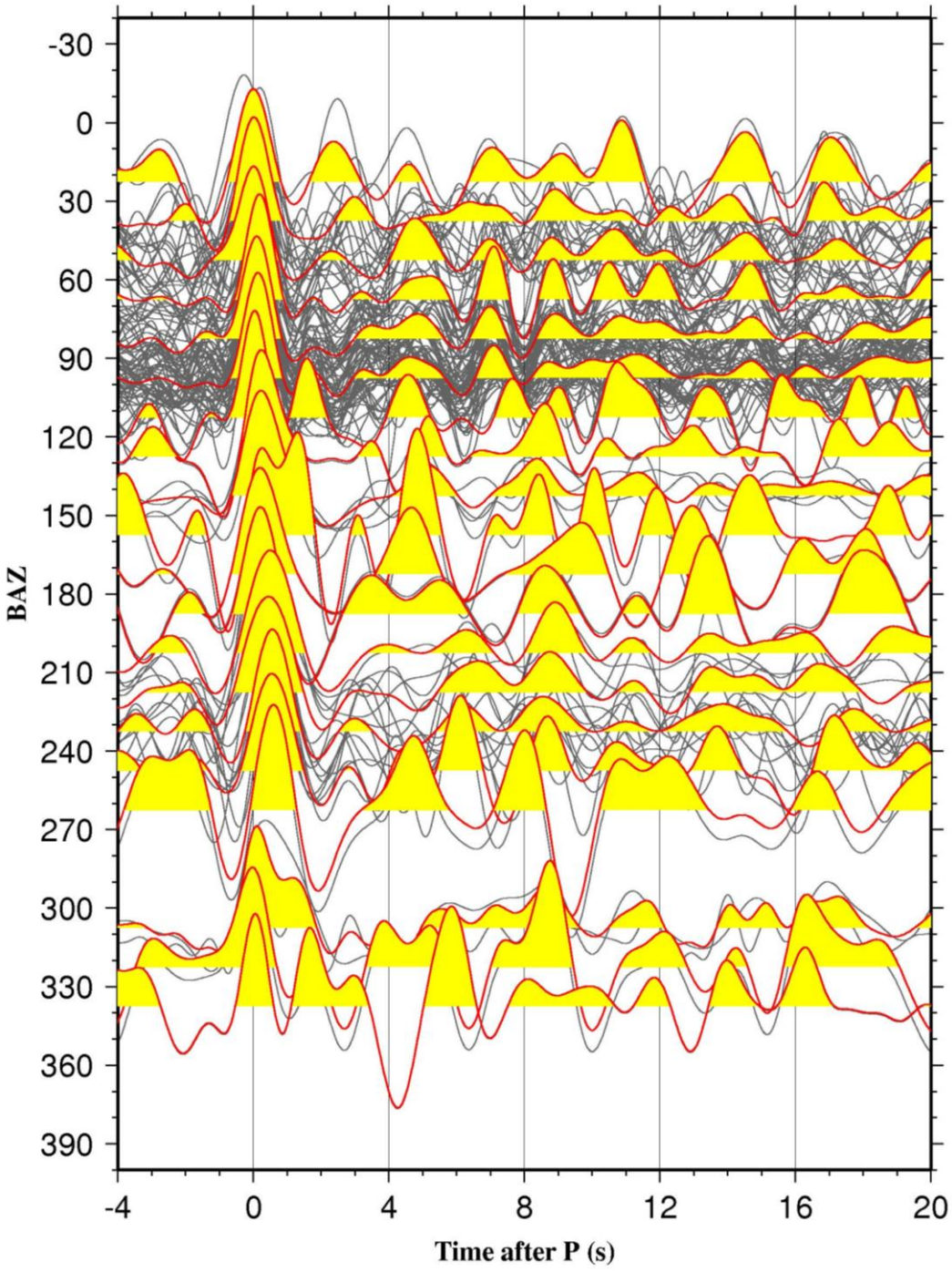

Figure 6.17. (a) Radial receiver functions plotted against the back-azimuth (BAZ) for AD18. Gray thin lines are individual RFs, and red thick lines are stacked RFs in 15° azimuthal bins.

b)

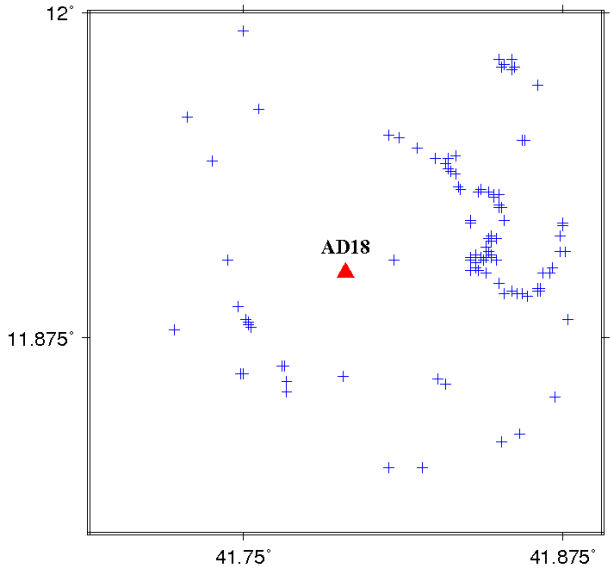

c)

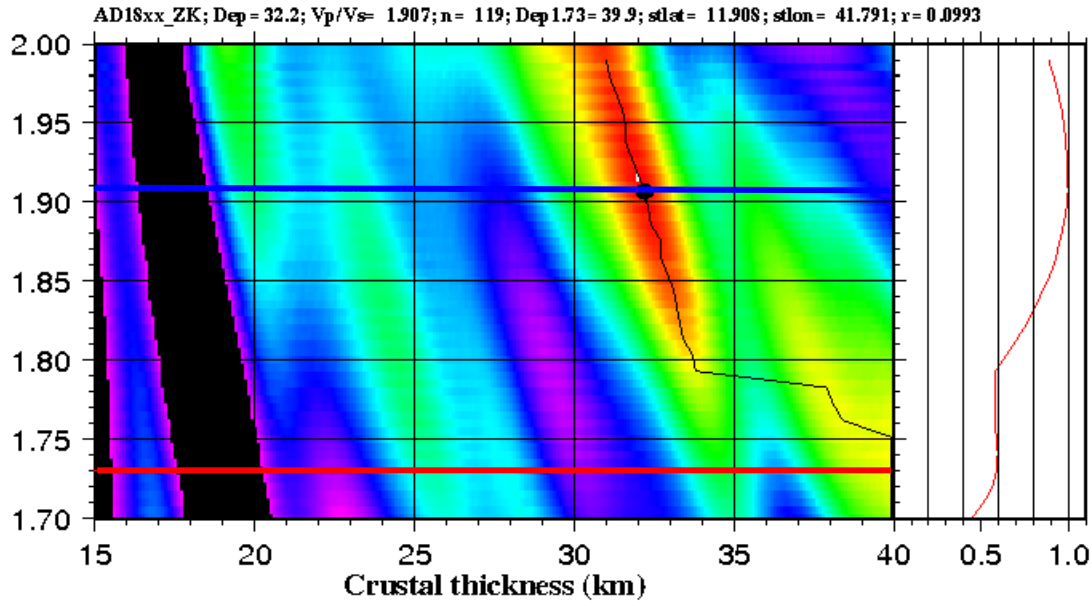

Figure 6.17. (Continued) (b) The distribution of ray-piercing points of the PmS phase for AD18. (c) H-k plots for station AD18. The red line shows the stacking amplitude for Φ=1.73. The blue line was obtained using the optimal Φ.

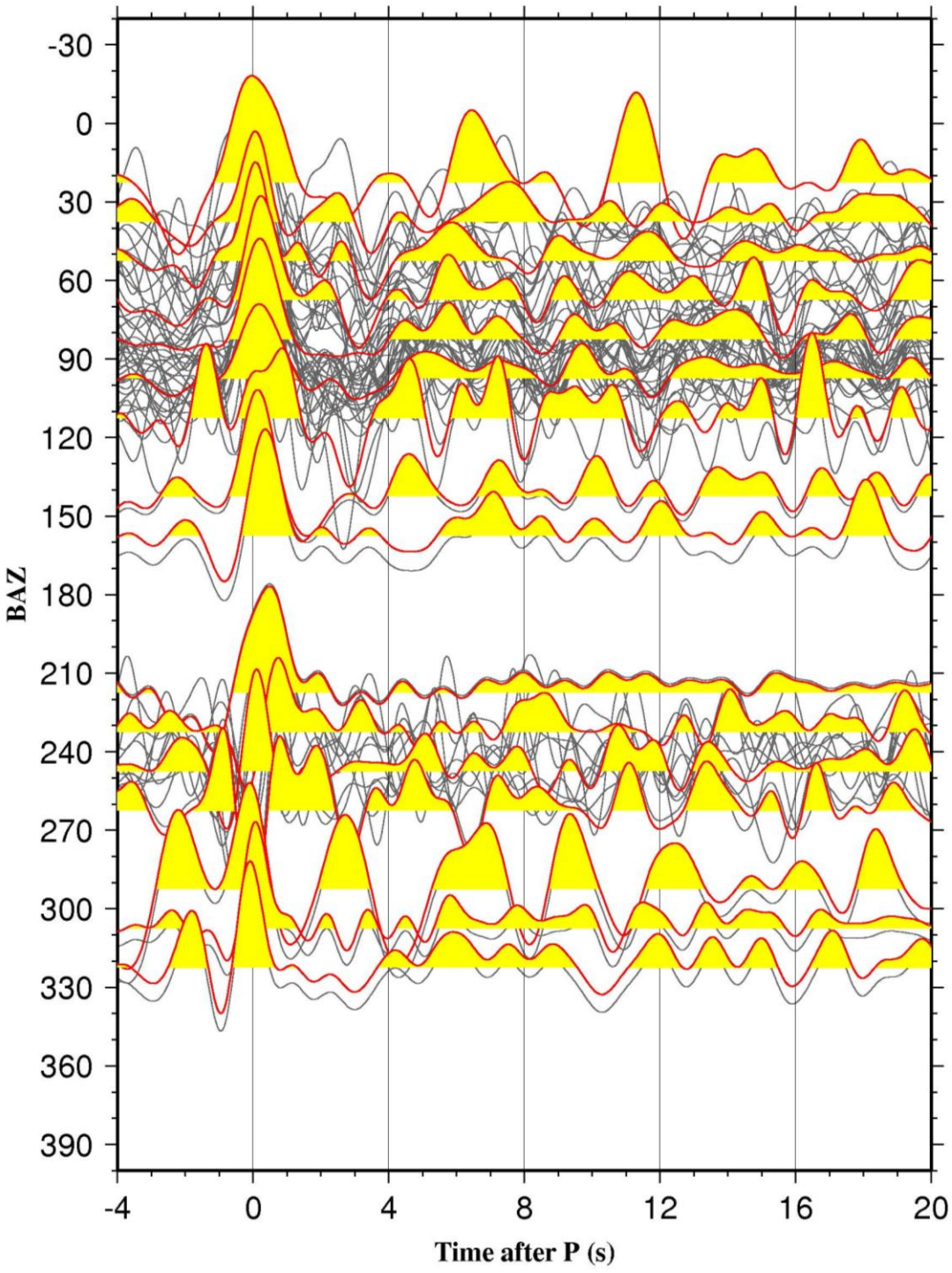

Figure 6.18. (a) Radial receiver functions plotted against the back-azimuth (BAZ) for AD19. Gray thin lines are individual RFs, and red thick lines are stacked RFs in 15° azimuthal bins.

b)

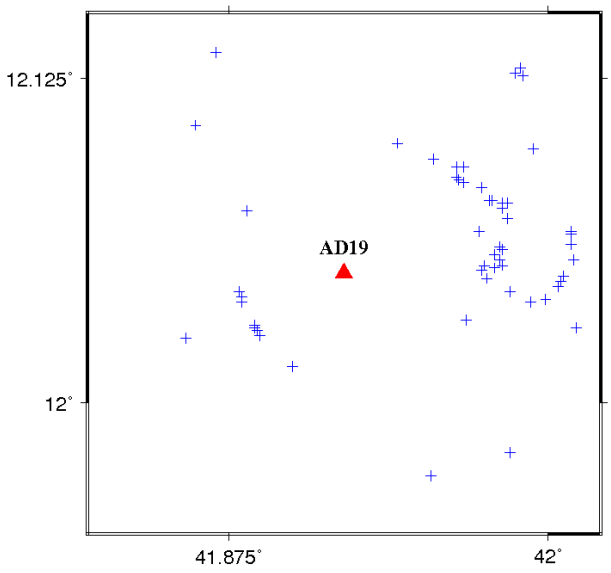

c)

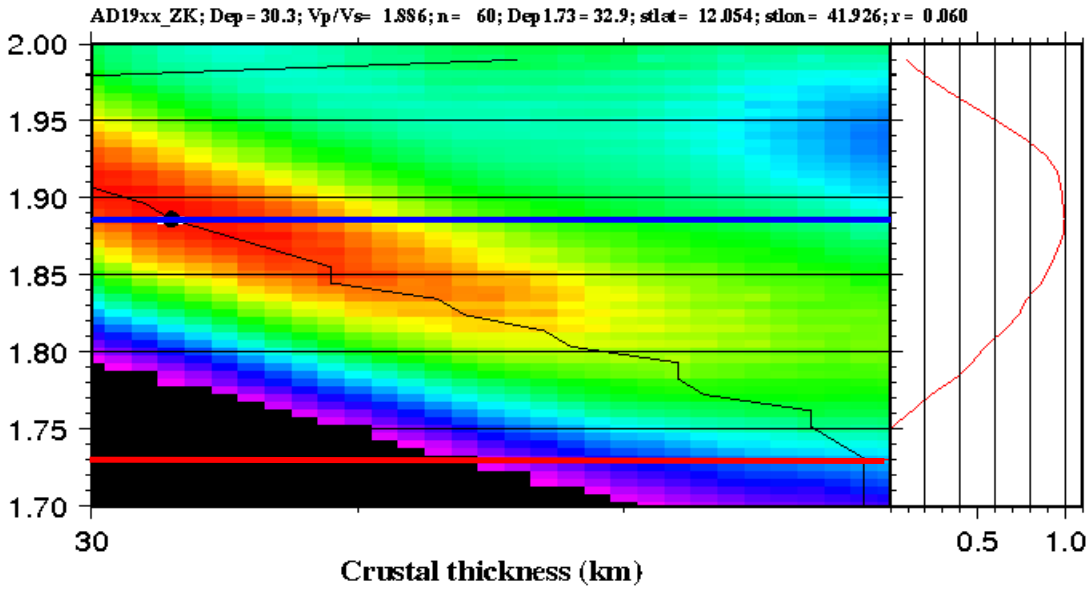

Figure 6.18. (Continued) (b) The distribution of ray-piercing points of the PmS phase for AD19. (c) H-k plots for station AD19. The red line shows the stacking amplitude for Φ=1.73. The blue line was obtained using the optimal Φ.

6.4 GRAVITY MODELING

From the observed Bouguer gravity anomaly data, Mickus [2011] created a two-dimensional gravity model (Figure 6.19). The resulting gravity model shows a 24-28 km thickness of the lower crustal layer beneath Tendaho Graben (TG). His gravity model uses 3.05 g/cm^3 density of the lower crust, which is slightly higher than the lower crustal density in the IASP91 earth model [Kennett and Engdahl, 1991]. The gravity minimum occurs over the area of maximum elevation, while values of Bouguer anomalies increase towards the TG. For example, the gravity pattern increases from a minimum of some -82 mGal to about -50 mGal in the TG, whereas values reach -56 mGal in the DG. The gravity anomaly varies between -50 to -63 mGal at the Tendaho and the Dobi grabens. The complete Bouguer anomalies map has revealed a distinct high in the TG sector and a low in the southeastern sector where elevation is higher and the crust is thicker than others. The main results suggest that the active magmatic areas (i.e. Tendaho Graben) are characterized by higher gravity anomalies and the areas having thicker crust (i.e. AD02) are described by lower gravity anomalies. The results also show the existence of a mafic upper crustal layer beneath the TG. Overall, the results indicate that gravity anomaly and crustal thickness are inversely related.

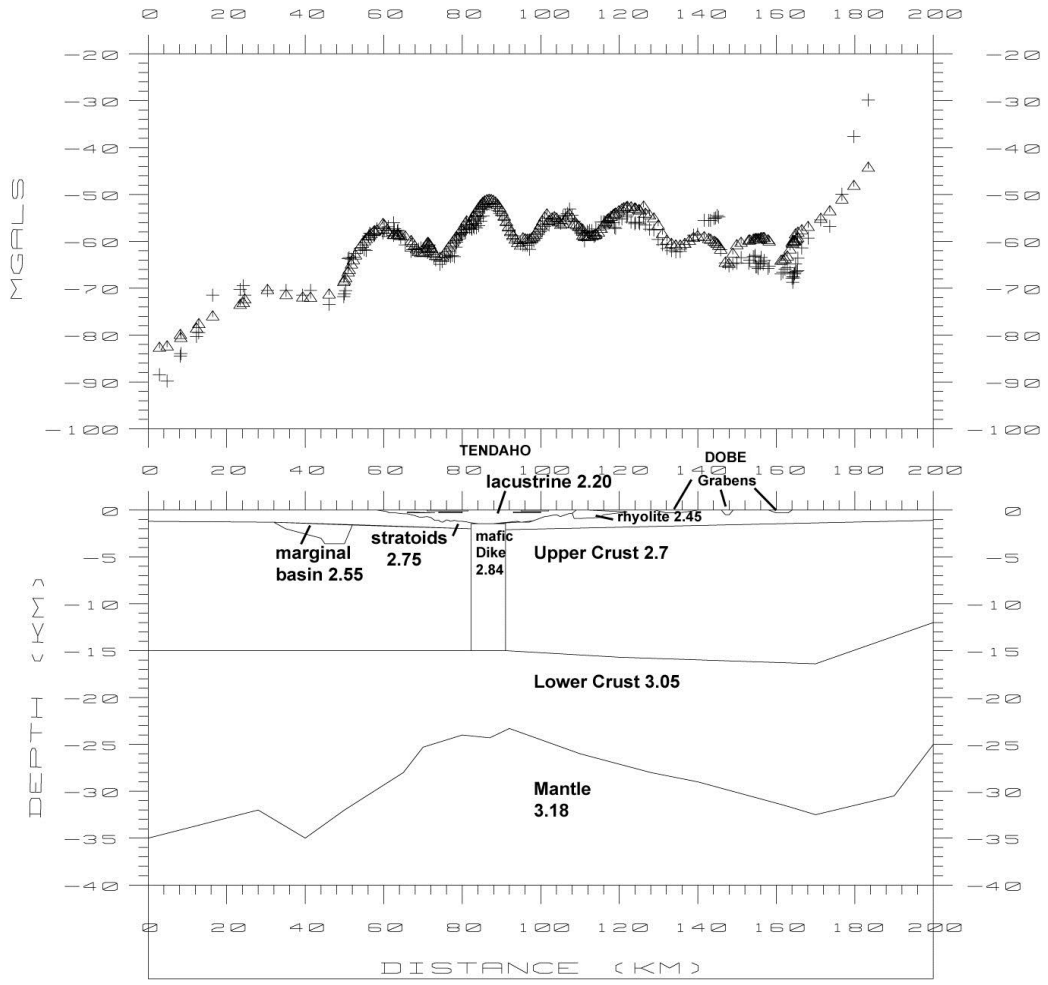

Figure 6.19. Bouguer Anomalies Model for the Afar Depression [after Mickus, 2011]

6.5 RECEIVER FUNCTION MIGRATION

Generally, migration techniques have been applied in reflection seismology to produce considerable image quality and work best in areas with dense data coverage [Stolt, 178; Berkhnout, 1982; Claerbout, 1992; Gray and May, 1994; Chen et al., 2005; Wilson and Aster, 2005; Wilson et al., 2005]. The techniques are used to reduce receiver functions deconvlution instability and aimed to map the true subsurface origin [Abers, 1998; Eaton et al., 2002, Wilson and Aster, 2005]. Kirchhoff coda migration method is frequently used for imaging the crust and the upper mantle structure [Revenaugh, 1995]. However, the method can not deal with lateral velocity variations; it only uses a constant velocity of each depth interval [Cehn et al., 2005]. Wilson and Aster [2005] suggested that the depth of the migrated receiver functions depend on the velocity model. Figure 6.20 shows a cross section of the migrated receiver function. The main feature of the migrated image shows well observed PmS converted phases along the profile. Overall, PmS phases generated at the Moho occur at the range of 24-34 km depth across the entire study area. The study observed that the crust beneath AD11 is thinner compared to those observed at AD15 and AD16.

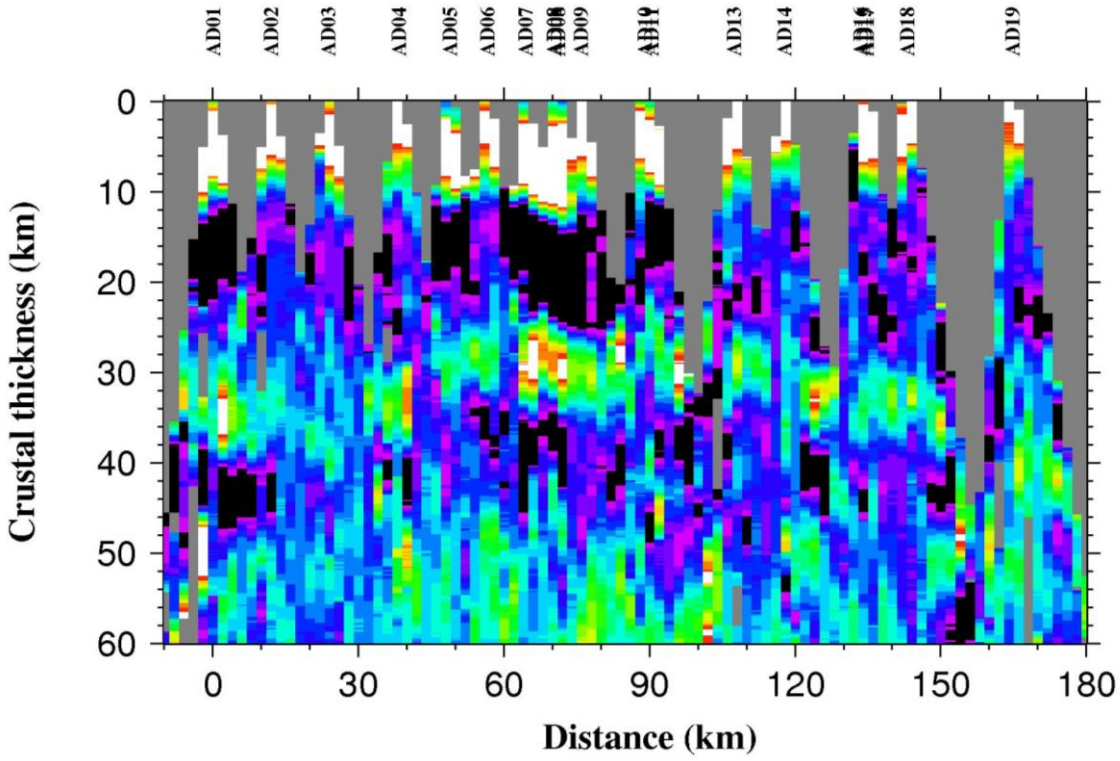

Figure 6.20. Receiver function migration for the Afar Depression

6.6 SUMMARY OF RESULTS

The results of this study are consistent with a good number of previous determinations of crustal characteristics. Previous seismic refraction surveys revealed a crust with a thickness ranging from 14-30 km [Ruegg and Lepine, 1973; Berckhemer et al., 1975; Prodehl and Mechie, 1991; Prodehl et al., 1997]. Dugda et al. [2005] stacked receiver functions at TEND seismic station and concluded that the average crustal thickness is 25 km. They also reported a high crustal Poisson's ratio of 0.36. Once more, Dugda and Nyblade [2006] characterized the crust beneath Afar by a fairly uniform thickness varying between the ranges of 20-25 km. Their method of receiver function analysis verified a high Poisson's ratio throughout most of the crust which is an indication of a mafic composition. They interpreted the presence of new igneous rock in the crust as a part of the extensional process in the region. To observe the crustal characteristics, the study plots elevation, H, V_p/V_s, and R values in a NE-striking band (Figure 6.21). The observed crustal parameters go well with the high elevation. Crustal thickness beneath the Dobi Graben varies between 29.04 km (AD17) and 32 km (AD18), and Poisson's ratios for the crust vary between 0.300 (AD19) and 0.329 (AD17). Beneath the Tendaho Graben, the Moho depths vary between 23.49 km (AD08) and 27.40 (AD09) km, and Poisson's ratios vary between 0.292 (AD03) and 0.348 (AD08). Many previous studies have proposed that the thinned crust beneath Afar region is caused by the high temperature in the mantle [Searle and Gouin, 1971; Ruegg, 1975; Makris and Ginzberg, 1987; Knox et al., 1999]. Those observations are in general agreement with our

results that show that the average crustal thickness (Figure 6.22) is 28.56±0.28 km, Φ values (Figure 6.23) for the entire study range from 1.844 to 2.071 with an average of 1.94±0.017, and the Poisson's ratio ranging from 0.29 to 0.34. Our crustal thickness, Poisson's ratio, and the amplitude of the converted Moho Sharpness (Figure 6.24) are summarized in Table 6. The Poisson's ratio of 0.310 we obtained is also consistent with the estimations collected by Ruegg (1975) of 0.28 to 0.33, Zandt and Ammon [1995] of 0.29, and Dugda and Nyblade (2006) of 0.30.

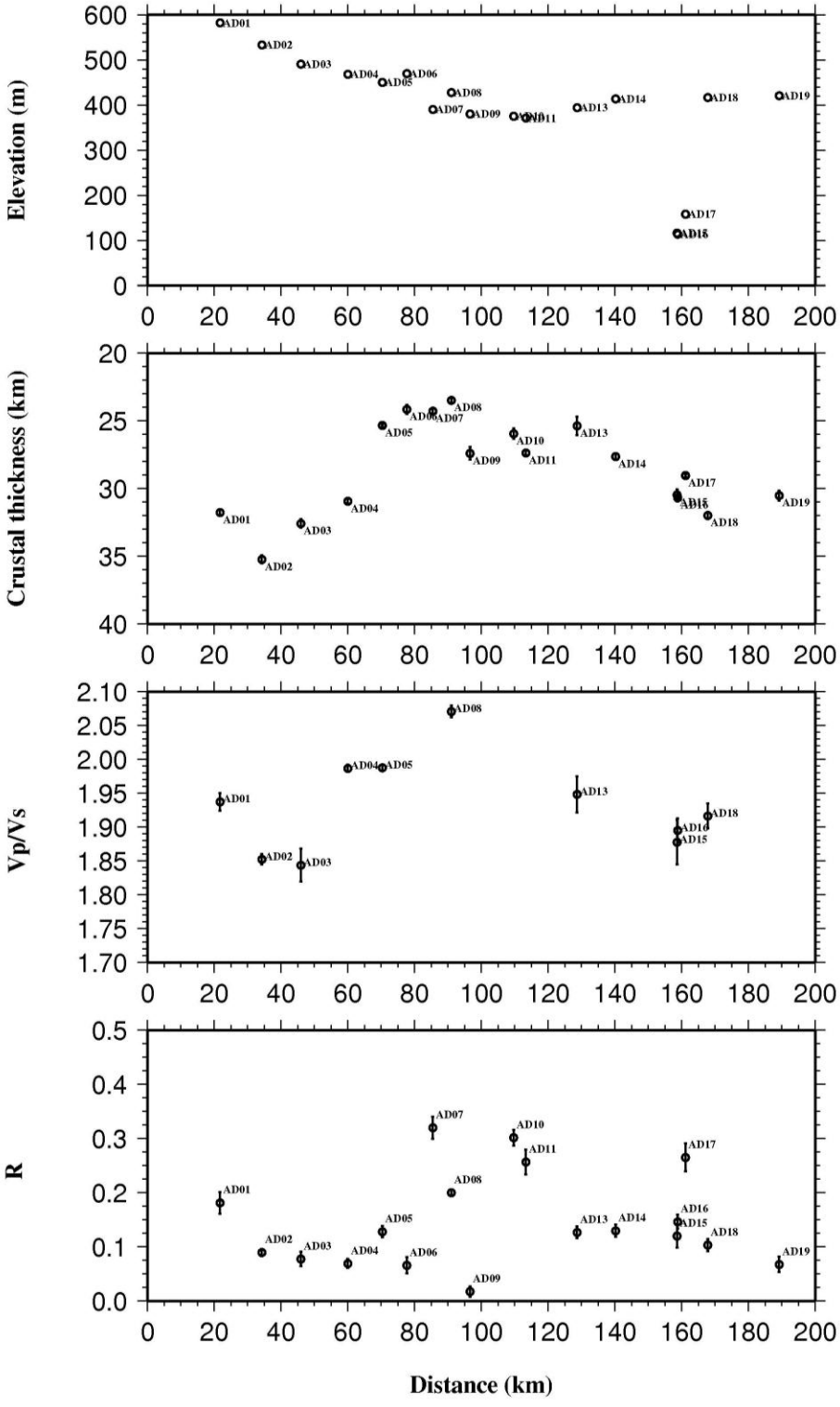

Figure 6.21. Cross-section plots for elevation, H, V_p/V_s, and R for the Afar Depression.

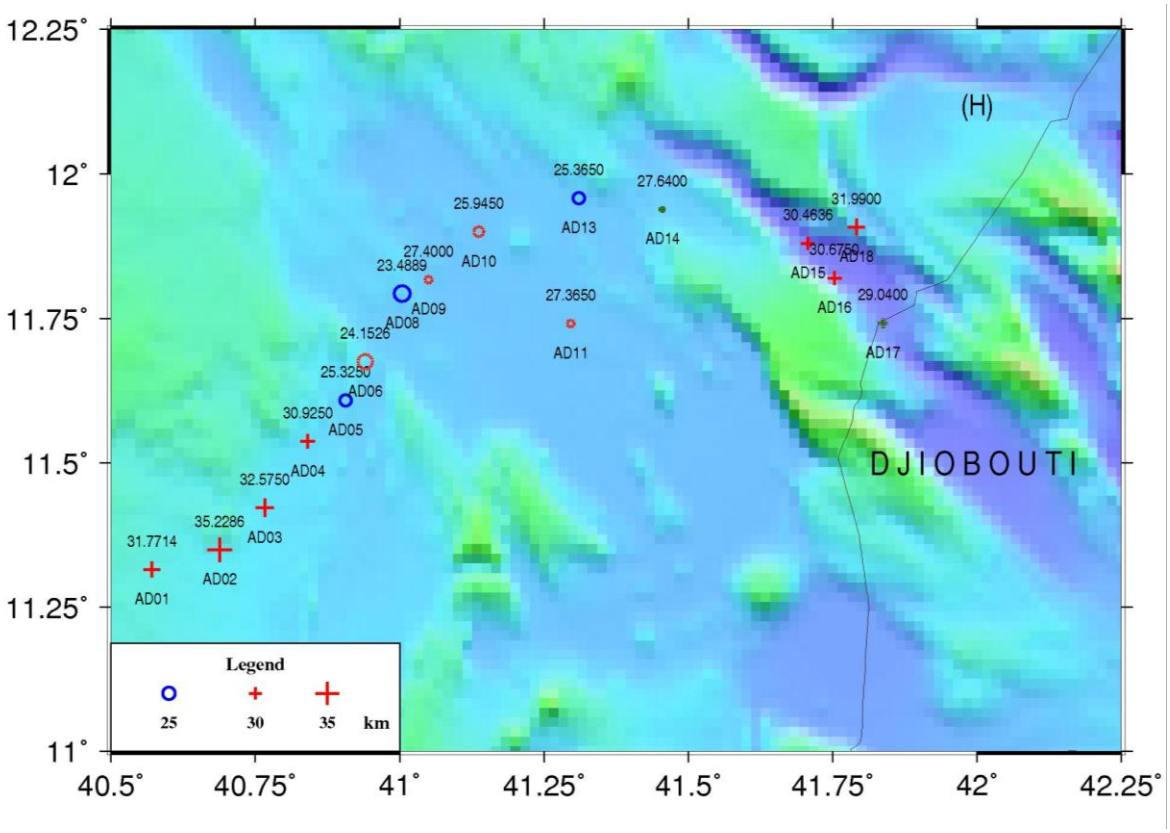

Figure 6.22. Resulting crustal thickness (H) for the Afar Depression. Circles represent stations with a smaller thickness and pluses represent stations with a larger thickness.

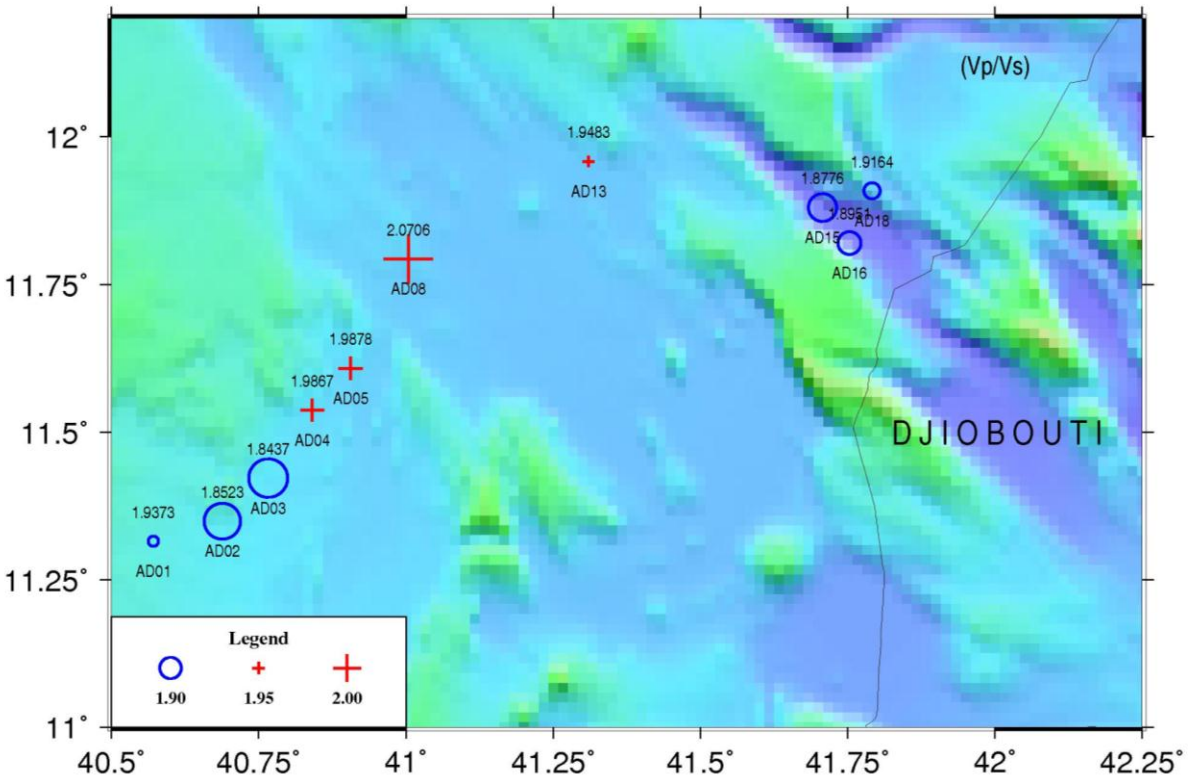

Figure 6.23. Resulting crustal V_p/V_s (Φ) for category A stations for the Afar Depression. Circles represent stations with a smaller V_p/V_s and pluses represent stations with a larger V_p/V_s.

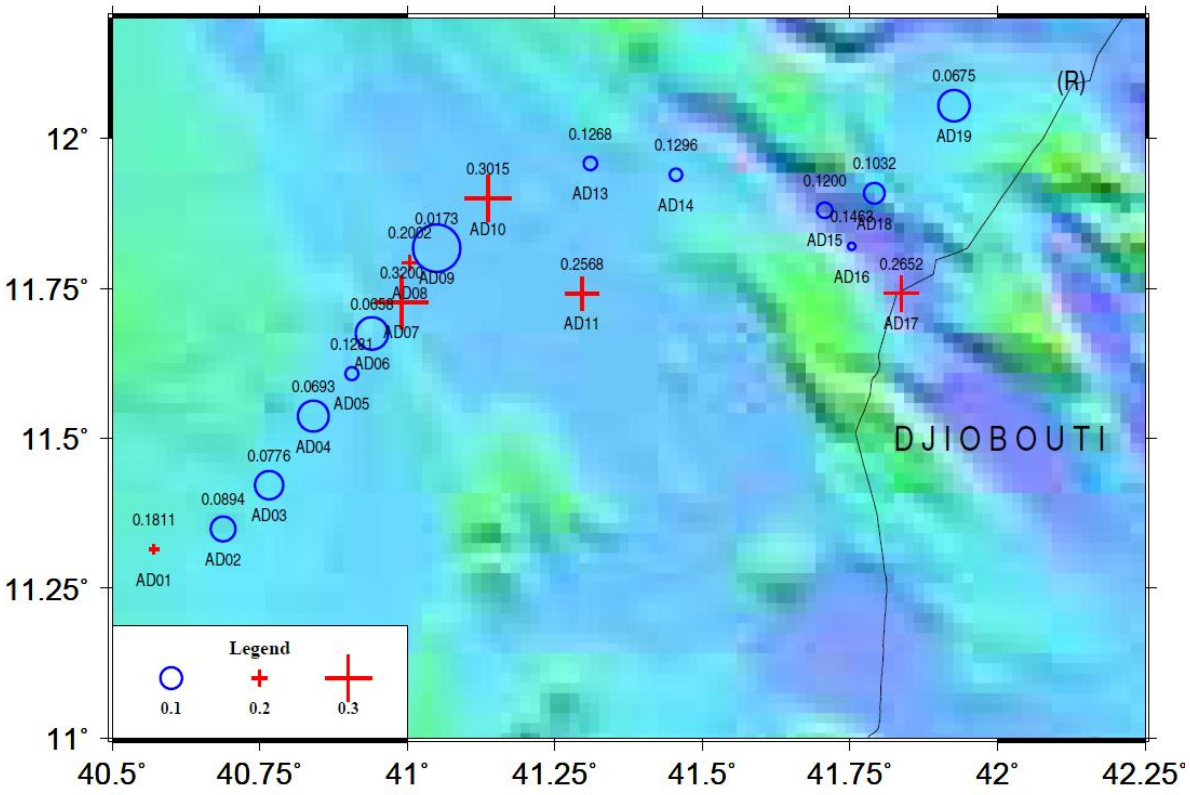

Figure 6.24. Resulting ratio (R) of the stacking amplitude corresponding to the optimal pair of (H, Φ) over that of direct P-wave on the radial component for the Afar Depression. R is calculated for all the stations. Circles represent stations with a smaller R and pluses represent stations with a larger R.

7. DISCUSSION

7.1 CRUSTAL COMPOSITION

Previous petrological studies suggested that the upper continental crust is mostly felsic in composition [Christensen and Mooney, 1995]. The estimations of V_p/V_s conducted in this study were used to constrain the lower crustal composition. Seismological observations and studies of lower crustal rocks have offered valuable information of the lower crustal components [Farmer et al., 1989; Holbrook et al., 1992; Percival et al., 1992; Rudnick, 1992]. The composition of the crust can be examined on the basis of mineral physics experiments that have suggested that felsic minerals have a V_p/V_s value of 1.76 or smaller, intermediate minerals have a V_p/V_s between 1.76 and 1.81, and mafic minerals have V_p/V_s values that is larger than 1.81 [Tarkov and Vavakin, 1982; Christensen, 1996; Chevrot and van der Hilst, 2000].

The determination of Poisson's ratio, the elastic deformation parameter, is crucial for understanding the nature of the Earth's crust. In general, the ratio is an indicator of lower crust composition and depends on both temperature and pressure [Christensen, 1996]. For seismic analyses, Poisson's ratio is calculated using the formula $\sigma=0.5[1-1/(\Phi^2-1)]$, where $\Phi=V_p/V_S$ [Tarkov and Vavakin, 1982; Christensen, 1996; Chevrot and van der Hilst, 2000]. It ranges from 0.05 to 0.20 for extremely tough materials and reaches a value of 0.5 for fluids having no shear strength [Gretener, 2003]. Moreover, low values of Poisson's ratio are typical found in high strength rocks such as basalt and quartzite [Engelmark, 2000]. The ratio

decreases by 0.2% at temperatures in the range of 0^{o} to 400^{o} for olivine and increases by 0.8% to 11% for other varieties of olivine [Christensen, 1996]. The study uses Poisson's ratio as a general indicator of bulk crustal composition. Granitic rocks have a Poisson's ratio of about 0.24, whereas intermediate composition rocks (e.g., diorite) have values of around 0.27, and mafic rocks (e.g., gabbro) about 0.30 [Tarkov and Vavakin, 1982; Christensen, 1996]. For an oceanic crust, Poisson's ratio can reach as high as 0.32 [Bratt and Solomon, 1984]. A Poisson's ratio higher than 0.30 is uncommon in continental areas and frequently indicates the existence of partial melt within continental settings [Watabane, 1993; Owens and Zandt, 1997].

Based on the earlier classifications, the study indicates that the crust layer is composed mainly of mafic material and the rock layer to be more brittle. In a global study, Zandt and Ammon [1995] concluded that the crust of ancient shields is characterized by a relatively high Poisson's ratio (0.29), which is indicative of mafic material in the lowermost crust. The results from our study, as well as those of Berckhemer et al. [1975], Makris and Ginzburg [1987], Tiberi et al. [2005] and Stuart et al. [2006], all point to the existence of diking and intrusion. Stuart et al. [2006] demonstrated that V_p/V_s ratio increases to larger than 2.0. (Poisson's ratio, $\sigma > 0.33$) and is an indication of partial melt. The amount of mafic material in the crust, which is a significant parameter, relies on mafic intrusion and/or underplating [Lachenbruch and Sass, 1978; Klemperer et al., 1986; Thompson and McCarthy, 1986]. The high Φ is an indication of a crust with an average mafic

composition that is more brittle than an "ordinary" continental crust. We suggest that mafic addition is a dominant process in the modification of crustal composition in the Afar Depression.

7.2 SPATIAL VARIATION OF V_P/V_S OBSERVATIONS

The H-k technique provides an estimate of average crustal V_p/V_s which can be directly converted into Poisson's ratio. The Φ distribution is remarkably large throughout the area. Rooney et al. [2005] proposed that the occurrence of the high V_p/V_s ratios require partial melt in the crust. The observed Φ values in this study seem to have a clear relationship with the crustal thickness (i.e. thinner crust corresponds to larger (V_p/V_s) (Figure 7.1). For instance, stations of thicker crusts like AD02 (35.23 km) and AD03 (32.58 km) show small values of Φ, where it is 1.852 for AD02 and 1.844 for AD03. On the other hand, the thinnest crust (at AD08) has the largest Φ. The crust beneath the center of the Tendaho Graben, where V_p/V_s is the highest, is thin and likely to be oceanic-type and it turns out to be continental-type away from the center where the values of V_p/V_s is less than the center of the TG. The crustal V_p/V_s increases dramatically as large as 2.071 in the Tendaho Graben, which corresponds to an increase of Poisson's ratio from 0.298 to 0.348, suggesting a more mafic crust beneath it. The mean values of V_p/V_s in SW of TG and the TG are considerably larger than those in the DG. For that reason, it is likely that magma source exist in the crust which led to rises the values of σ.

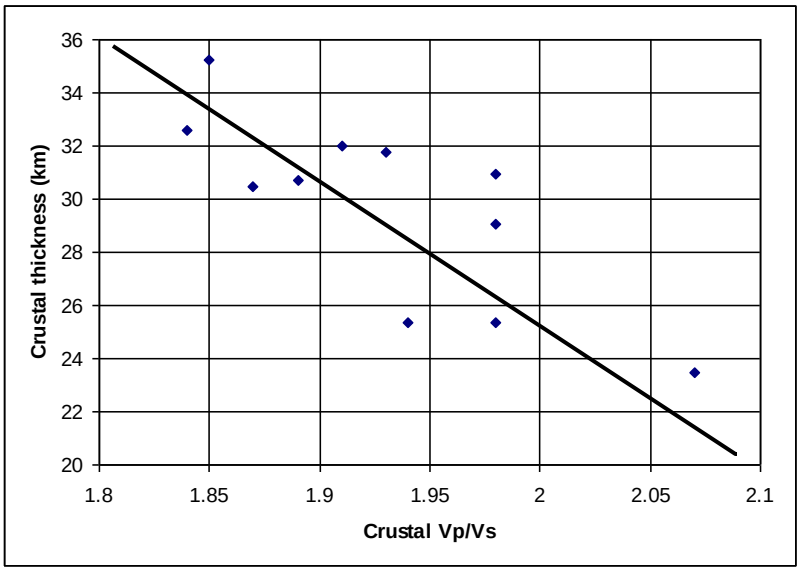

Figure 7.1 The relationship between the resulting crustal thickness (H) and V_p/V_s for the Afar Depression

7.3 CRUSTAL THICKNESS VARIATIONS ACROSS THE ARRAY

The crustal thicknesses determined from receiver function analysis in this study show an average of 28.56±0.28 km. Crustal thickness beneath the Dobi Graben varies between 27.64 km (AD14) and 32 km (AD18), while beneath the Tendaho Graben the Moho depths vary between 23.49 km (AD08) and 27.40 km (AD09) (Table 7.1). The TG has the thinnest and most mafic crust which is also revealed by gravity and magnetic data. Previous studies have proposed that the thinned crust beneath the Afar region is associated with the presence of the mantle plume [Searle and Gouin, 1971; Ruegg, 1975; Makris and Ginzberg, 1987; Knox et al., 1999]. Our estimations of H, based on the receiver functions and the gravity data, are in agreement with previous studies. The resulting crustal thicknesses show that

the TG stations have thinner crust comparing with those in SW of TG and the DG. Dugda et al. [2005] stacked 48 receiver functions to measured H at TEND station near AD08. They concluded that the average crustal thickness is 25 km with V_p/V_S mean of 2.12. Their results are consistent with our resulting crustal thickness (23.49±0.17 km) and V_p/V_s value (2.071±0.009) at AD08. Our observations concerning the variations of crustal thickness follow the trends of northeast thinning of the crust between (AD04-AD08). The greatest crustal thickness is found beneath station AD02 (~ 35.23 km) where the elevation is the second highest one (~ 523 m). The second thicker crust is at AD03 (~ 32.58 km) where the elevation is 488 m above sea level. The observed crustal thickness results show that at elevations higher than 480 m, the resulting crustal thickness become larger than 30 km. Most of those stations are located in the SW of TG.

Table 7.1 The resulting crustal thickness (H), V_p/V_s, and Poisson's ratio (σ) for the three divisions for the Afar Depression

	Station	Lat. North	Long. East	Elev. (m)	H (km)	H STD	Φ	Φ STD	R	R STD	Poisson's ratio	Quality
SW of TG	AD01	11.32	40.571	580	31.77	0.19	1.937	0.013	0.181	0.019	0.318	A
	AD02	11.35	40.688	523	35.23	0.29	1.852	0.007	0.089	0.006	0.294	A
	AD03	11.42	40.766	488	32.58	0.33	1.844	0.024	0.078	0.013	0.292	A
	AD04	11.54	40.841	483	30.93	0.15	1.987	0.005	0.069	0.009	0.330	A
	AD05	11.61	40.906	451	25.33	0.11	1.988	0.004	0.128	0.01	0.331	A
	Mean				**31.17**	**0.214**	**1.922**	**0.0106**	**0.109**	**0.0114**	**0.313**	
TG	AD06	11.68	40.94	460	24.15	0.33	1.921	0.041	0.066	0.015	0.314	B
	AD07	11.73	40.99	395	24.29	0.21	1.93	0.01	0.32	0.021	0.317	B
	AD08	11.78	41.028	391	23.49	0.17	2.071	0.009	0.2	0.005	0.348	A
	AD09	11.82	41.05	385	27.4	0.47	1.945	0.042	0.017	0.009	0.320	B
	AD10	11.8	41.137	370	25.95	0.37	1.866	0.015	0.302	0.015	0.298	B
	AD11	11.74	41.296	370	27.37	0.15	1.964	0.01	0.257	0.023	0.325	B
	AD13	11.96	41.31	352	25.37	0.68	1.948	0.027	0.127	0.011	0.321	A
	Mean				**25.43**	**0.34**	**1.949**	**0.022**	**0.184**	**0.0141**	**0.320**	
DG	AD14	11.94	41.455	422	27.64	0.25	1.984	0.009	0.13	0.011	0.330	B
	AD15	11.88	41.707	88	30.46	0.4	1.878	0.033	0.12	0.021	0.302	A
	AD16	11.82	41.753	118	30.68	0.28	1.895	0.018	0.146	0.013	0.307	A
	AD17	11.74	41.837	150	29.04	0.12	1.981	0.006	0.265	0.026	0.329	A
	AD18	11.91	41.791	452	31.99	0.26	1.916	0.019	0.103	0.011	0.313	A
	AD19	12.05	41.926	435	30.52	0.36	1.87	0.016	0.068	0.014	0.300	B
	Mean				**30.05**	**0.278**	**1.921**	**0.0168**	**0.139**	**0.016**	**0.313**	

7.4 MOHO SHARPNESS

The sharpness of the Moho is associated with the thickness of the transition layer between the crust and the mantle. Analysis of refracted seismic arrivals suggested that the transition layer is not more than ½ km thick in stable areas [Nakamura and Howell, 1964]. Within active regions, the transition is most likely less sharp [Green and Fallon, 1998]. A clear observation of PmS and its multiples reflect a sharp Moho. Overall, The Afar depression has smaller-than-normal (~ 0.14±0.014) stacking amplitude of the P-to-S converted phases beneath most stations. However, the values are slightly higher in the TG stations than others, having an average of 0.184.

7.5 EVOLUTION OF THE CRUST

Several studies have confirmed that magmatic processes in the Afar Depression continue to the present day [Tadesse et al., 2003; Keri et al., 2005; Ayele et al., 2007; Brazier et al., 2008; Keri et al., 2009]. However, the nature of Afar crust has been a subject of debate among scholars [McKenzie et al., 1970; Barberi and Varet, 1975, 1977; Vellutini, 1990; Cochran, 1981; Kazmin and Byakov, 2000]. Mohr (1978) suggested that the early Afar crust represents an oceanic-type except that it was remodeled by mantle plume. He also noted that the crustal thickening depends on the extreme magmatism found in the region. Dudga and Nyblade [2006] suggested that the Afar lithosphere is composed of new igneous rock associated with dike injection. A recent detailed geochemical and isotopic study conducted by Teklay et al. [2010] suggested that the lower crust beneath Afar contains Neoproterozoic mafic igneous rocks.

Our estimates of the crustal structure are in good agreement with the results of previous studies in the region [Berckhemer et al., 1975; Prodehl and Mechie, 1991; Prodehl, et al., 1997; Mammo, 2004]. Dugda et al. [2005] revealed, using receiver function analysis from seismic data, that the crust beneath Afar is just about 25 km thick. They also reported, from a temporary broadband station located at Tendaho area, a high crustal Poisson's ratio of 0.36. Moreover, Dugda and Nyblade [2006] characterized the crust beneath Afar by fairly uniform thickness varying between 20-25 km. Their method of receiver function analysis verified a high Poisson's ratio throughout most of the crust and is an indication of a mafic composition. They interpreted the presence of new igneous rock in the crust as a part of the extensional process in the region.

The crustal thickness determined from the method of receiver function analysis in this study shows an average of 28.56±0.28 km. The crustal thickness varies from 23.49±0.17 km (AD08) to 35.23±0.29 km (AD02). At most of the stations, it is possible to identify the depth to Moho which is sampled by P-to-S conversions (PmS) and by later reverberations. We observed that the crustal thicknesses beneath stations southwest of the TG (AD01-AD05) are thicker than those in the other two areas with having an average of 31.17 km. The crustal thickness measurements beneath the DG and adjacent horsts (AD14-AD19) have, to some extent, similar average value of H (30.05 km). However, the maximum amount of thinning was observed at the center of the TG (AD06-AD13). The V_p/V_s distribution is, in fact, high all over the study area. Stations AD04, AD05, AD08, AD14 and

AD17 have high values of V_p/V_s, with the highest in the entire study area at AD08 (2.07). The distribution of V_p/V_s for the TG shows that the values are the highest in the center of the graben as well as the percentage amount of diking which indicate that the center of the graben has the highest heat source comparing to the areas away from it. The following formula was used to determine the percentage amount of diking *(B)* and was based on the average values of V_p/V_s for continental crust (1.78) and oceanic crust (2.1):

$$B = \frac{(\phi - 1.78)}{0.32} \quad , \qquad where\ \phi\ is\ the\ resulting\ V_p / V_s \tag{5}$$

Figure (7.2) shows a cross-section plot for the calculated percentage of diking for A stations in the Afar Depression. The results show that the area of maximum diking is located at the center of the Tendaho Graben. While, stations located in the Dobi Graben ranging from 30-60 percentage of diking.

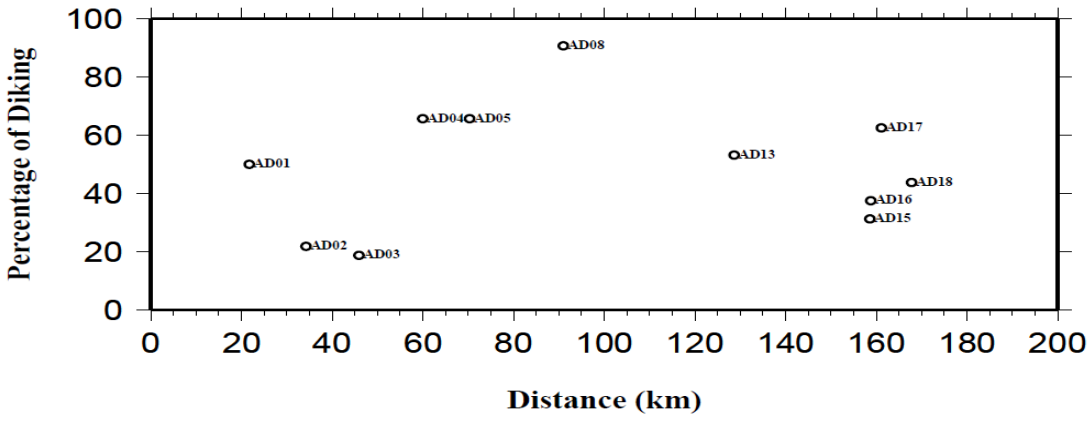

Figure 7.2 The calculated percentage of diking for A stations in the Afar Depression

Based on our observations, it is likely that diking plays an important role on the resulting parameters of H, V_p/V_s, and σ. For example, the

resulting crustal thickness show that it is the thinnest at the center of the TG and it becomes thicker moving away from it. Moreover, the highest V_p/V_s value is found beneath AD08 which indicate that presence of heat source is associated with the presence of diking. It is reasonable to hypothesize that the high Φ and low H values observed in the TG are due to the high amount of diking intruding the crust and is likely to be considered as an oceanic-type and the amount of diking decreases moving away from the centre of the TG and the crust becomes progressively more continental. In addition, the presence of extensive dikes could also explain the smaller-than-normal overall stacking amplitude of the P-to-S converted phases beneath most stations due to the decreased velocity contrast areas. Our results suggest that diking is more likely the source which causes the elevation of Φ values and the thinning of the crust beneath the center of the Tendaho Graben.

The highly observed values of Φ beneath most of the stations in this study are supported by the result of Mohr [1989] who argued that 65% of Afar Depression lithosphere has been injected with mafic dikes. As we have noted, the highest value of V_p/V_s was found beneath the center of the TG and is associated with the existence of high amount of diking. Therefore, this research summarizes that magma rising in form of vertical dikes influenced the study area which caused deformation and depression, and disturbed the crust mantle boundary. Consequently, thinner crust has been formed beneath the Afar Depression relative to the surrounding area. Therefore, the rising diking in the center of the TG disturb the Moho boundary and makes it less sharp.

8. CONCLUSIONS

The Afar Depression is characterized by a crustal thickness of 28.56±0.28 km, high crustal Poisson's ratio of 0.32, and smaller-than-normal overall (≈0.14±0.014) stacking amplitude of the P-to-S converted phases beneath most stations. The observed Φ values in this study seem to have a clear relationship with the crustal thickness (i.e. smaller H corresponds to large V_p/V_s). The high Poisson's ratios throughout the study area and the smaller-than-normal R measurements indicate that the crust is more mafic in composition than a typical continental crust, probably due to extensive intrusion of mafic dikes into the crust. Our results suggest that the crust beneath the entire study area is significantly thinned and extensively intruded by mafic dikes, representing a transitional stage between continental and ocean crust. The Tendaho Graben has the thinnest and most mafic crust, which is also supported by the observed Bouguer anomaly data that suggest that the active magmatic areas (i.e. Tendaho Graben) are characterized by higher gravity anomalies while the thicker crusts (i.e. AD02) have small and negative anomalies.

BIBLIOGRAPHY

Abbate, E., P. Passerini, L. Zan (1995). Strike-slip faults in a rift area: a transect in the Afar Triangle, East Africa. *Tectonophysics*, 241, 67–97.

Abebe, B, V. Acocoella, T. Korme, and D. Ayalew (2007). Quaternary faulting and volcanism in the Main Ethiopian Rift. *Journal of African Earth Sciences*. Volume 48, Issues 2-3, June 2007, Pages 115-124.

Abers, G. A. (1998), Array measurements of phases used in receiver function calculations: Importance of scattering, Bull. Seismol. Soc. Am., 88, 313 – 318.

Acocella, V. (2010). Coupling volcanism and tectonics along divergent plate boundaries: Collapsed rifts from central Afar, Ethiopia. *GSA Bulletin*; September/October 2010; v. 122; no. 9/10; p. 1717–1728; doi: 10.1130/B30105.1.

Acocella, V. and T. Korme (2002). Holocene extension direction along the Main Ethiopian Rift, East Africa. *Terra Nova*, Volume 14, Issue 3, pages 191–197, June 2002.

Acton, G.D., A. Tessema, M. Jackson, R. Bilham (2000). The tectonic and geomagnetic significance of paleomagnetic observations from volcanic rocks from central Afar, Africa. *Earth and Planetary Science Letters* 180, 225–241.

Acton, G.D., S. Stein, and J.F. Engeln (1991). Block rotation and continental extension in Afar: A comparison to oceanic microplate systems: *Tectonics*, v. 10, p. 501– 526, doi: 10.1029/90TC01792.

Al-Damegh, K., E. Sandvol, and M. Barazangi (2005). Crustal structure of the Arabian plate: New constraints from the analysis of teleseismic receiver functions, *Earth and Planet. Sci. Lett*., 231, 177-196.

Ali, S. (2001). Geochemistry of the Tendaho geothermal field, Ethiopia. Stanford Geothermal Workshop. Stanford Geothermal Program.

Ammon, C., G. Randall, and G. Zandt (1990). On the non-uniqueness of receiver function inversions, *J. Geophys.* Res., 95, 15, 303–15, 318.

Anderson, D. L. (2005). Scoring hotspots: The plume and plate paradigms. Geological Society of America. Speical Paper 388.

Aquater (1996). Tendaho geothermal project, final report. MME, EIGS - *Government of Italy, Ministry of Foreign Affairs*, San Lorenzo in Campo.

Audin, L., X. Quidelleur, E. Coulié, V. Courtillot, S. Gilder, I. Manighetti, P.Y. Gillot, P. Tapponnier, and T. Kidane (2004). Paleomagnetism and K-Ar and 40Ar/39Ar ages in the Ali Sabieh area (Republic of Djibouti and Ethiopia): Constraints on the mechanism of Aden ridge propagation into southeastern Afar during the last 10 Myr: *Geophysical Journal International*, v. 158, p. 327–345, doi: 10.1111/j.1365-246X.2004.02286.x.

Barberi, F., J. Varet (1977). Volcanism of Afar: small-scale plate tectonics implication. *Geological Society of America Bulletin* 88, 1251–1266.

Barberi, F., G. Ferrara, R. Santacroce, and J. Varet (1975). Structural evolution of the Afar triple junction, in Pilger , A., and Rosler, A., eds., Afar Depression of Ethiopia: *Stuttgart*, v. 1, p. 39–54.

Barberi, F., S. Borsi, G. Ferrarea, G. Marinelli, R. Santcroce, H. Tazief, J. Varet (1972). Evolution of the Danakil Depression (Afar Ethiopia) in light of radiometric age determination. *Journal of Geology* 80, 720–729.

Behn, M.D. and P.B. Kelemen (2006). Stability of arc lower crust: Insights from the Talkeetna arc section, south central Alaska, and the seismic structure of modern arcs. *J. Geophy. Res.* 111(B11207), doi:10.1029/2006JB004327.

Benoit, M., A. A. Nyblade, and J.C. VanDecar (2006). Upper mantle P-wave speed variations beneath Ethiopia and the origin of the Afar hotspot. *Geology*; May 2006; v. 34; no. 5; p. 329–332; doi: 10.1130/G22281.1.

Berckhemer, H., B. Baier, H. Bartelsen, A. Behle, H. Burkhardt, H. Gebrande, J. Makris, H. Menzel, H. Miller, R. Vees (1975). Deep seismic soundings in the Afar region and on the highland of Ethiopia. In: Pilger, A., Rosler, A. (Eds.), Afar Depression of Ethiopia, Proceedings of an International Symposium on the Afar Region and Rift Related Problems, Bad Bergzabren, Germany, 1974, vol. 1. E. *Schweizerbart_sche Verlagsbuchhandlung*, Stuttgart, Germany, pp. 89–107.

Beyene, A. and M. Abdelsalam (2005). Tectonics of the Afar Depression: A review and synthesis. *Journal of African Earth Sciences*, 41–59.

Beyene, M. and M. Abdelsalam (2002). The importance of studying mesoscopic structure for understanding extensional tectonic regimes: examples from the Afar Depression, Ethiopia. *South-Central Section (37th) and Southeastern Section (52nd)*, GSA Joint Annual Meeting (March 12–14, 2003).

Bilham, R., R. Bendick, K. Larson, P. Mohr, J. Braun, S. Tesfaye, and L. Asfaw (1999). Secular and tidal strain across the Main Ethiopian Rift. *Geophysical Research Letters,* 26, 2789–2792.

Boccaletti, M., R. Mazzuoli, M. Bonini, T. Trua, B. Abebe (1999). Plio-Quaternary volcanotectonic activity in the northern sector of the Main Ethiopian Rift; relationships with oblique rifting. *Journal of African Earth Sciences* 29, 679–698.

Bonini, M., G. Corti, F. Innocenti, P. Manetti, F. Mazzarini, T. Abebe, Z. Pecskay (2005). The evolution of the Main Ethiopian Rift in the frame of Afar and Kenya rifts propagation. *Tectonics*, 24, TC1007. doi:10.1029/2004TC001680.

Bratt, S. R., and S. C. Solomon (1984), Compressional and shear wave structure of the East Pacific Rise at 11°26′N: Constraints from three component ocean bottom seismometer data, *J. Geophys. Res.*, 89, 6095–6110, doi:10.1029/JB089iB07p06095.

Brazier, R. A., Q. Miao, A. A. Nyblade, A. Ayele, and C. A. Langston (2008). Local magnitude scale for the Ethiopian Plateau, *Bull. Seismol. Soc. Am.*, 98, 2341–2348, doi:10.1785/0120070266.

Burdick, L. J. and C. A. Langston (1977). "Modeling crustal structure through the use of converted phases in teleseismic body waveforms." *Bull. Seism. Soc. Am.* 67: 677-692.

Casey, M., C.J. Ebinger, D. Keir, R. Gloaguen, F. Mohamad (2006). Strain accommodation in transitional rifts: extension by magma intrusion and faulting in Ethiopian rift magmatic segments. In: Yirgu, G., Ebinger, C.J., Maguire, P.K.H. (Eds.), The Afar Volcanic Province within the East African Rift System*: Geol. Soc. Spec. Publ.,* 259, pp. 143–163.

Chernet, T., W.K. Hart, J.L. Aronson, R.C. Walter (1998). New age constraints on the timing of volcanism and tectonism in the northern Main Ethiopian Rift-southern Afar transition zone (Ethiopia). *Journal of Volcanology and Geothermal Research* 80, 267–280.

Chevrot, S., and R. D. Van der Hilst (2003). On the effects of a dipping axis of symmetry on shear wave splitting measurements, *Geophysical Journal International,* v. 152, p. 497-505.

Christensen, N. I. (1996). Poisson‘s ratio and crustal seismology, *J. Geophys. Res*., 101, 3139– 3156.

Christensen, N. I., and W. D. Mooney (1995). Seismic velocity structure and composition of the continental crust: A global review. *J. Geophys. Res.*, 100, 9761-9788.

Christiansen, T. B., H. Schaefer, M. Schoenfeld (1975). Geology of southern and central Afar, Ethiopia. In: Pilger, A., Rosler, A. (Eds.), Afar Depression of Ethiopia, Proceedings of an International Symposium on the Afar Region and Rift Related Problems, Bad Bergzabren, Germany, 1974, vol. 1. E. *Schweizerbartsche Verlagsbuchhandlung,* Stuttgart, Germany, pp. 259–277.

Chu, D., R.G. Gordon (1998). Current plate motions across the Red Sea. *Geophysical Journal International* 135, 313–328.

Clouser, R.H. & C.A. Langston (1995). Modeling P-Rg conversions from isolated topographic features near the NORESS Array, *Bull. seism. SOC. Am.*, 85, 859-873.

CNR-CNRS-Afar team (1973). Geology of northern Afar (Ethiopia). *Revue de Geographie Pysique et de Geologie Dynamique* 2, 343– 390.

Cochran, J.R. (1981). Pre-sea floor spreading development of the Gulf of Aden. *Oceanologica Acta Supplement* 4, 155–165.

Collet, B., H. Taud, J.F. Parrot, F. Bonavia, J. Chorowicz (2000). A new kinematic approach for the Danakil Block using a digital elevation model representation. *Tectonophysics* 316, 343–357.

Courtillot, V., J. Achache, F. Landre, N. Bonhommet, R. Montigny, G. Feraud (1984). Episodic spreading and rift propagation; new paleomagnetic and geochronologic data from the Afar nascent passive margin. *Journal of Geophysical Research* 89, 3315–3333.

Davidson, A. and D.C. Rex (1980). Age of volcanism and rifting in Southwestern Ethiopia. *Nature*, 283, pp. 657–658.

Dueker, K. G., and A.F. Sheehan (1998). Mantle discontinuity structure beneath the Colorado Rocky Mountains and High Plains, *J. Geophys. Res.* 103, 7153–7169.

Dugda, M., Nyblade, A. (2006). New constraints on crustal structure in eastern Afar from the analysis of receiver functions and surface wave dispersion in Djibouti. *The Geological Society of London*, 259, 239-251.

Dugda, M. T., A. A. Nyblade, J. Julia, C. A. Langston, C. J. Ammon, and S. Simiyu (2005), Crustal structure in Ethiopia and Kenya from receiver function analysis: Implications for rift development in eastern Africa, *J. Geophys. Res.,* 110, B01303, doi:10.1029/2004JB003065.

Eagles, G., R. Gloaguen, C. Ebinger (2002). Kinematics of the Danakil Microplate. *Earth and Planetary Science Letters* 203, 607– 620.

Eaton, D. W., J. Hope, and T. Bohlen (2002), An elastic Kirchhoff method for computing synthetic seismograms: Modeling the receiver-function response of an irregular Moho surface, Seismol. Res. Lett., 73(2), 232.

Ebinger, C.J., T. Yemane, D.J. Harding, S. Tesfaye, S. Kelley and D.C. Rex (2000). Rift deflection, migration, and propagation; linkage of the Ethiopian and Eastern rifts, Africa. *Geol. Soc. Am. Bull.,* 112, pp. 163–176.

Ebinger, C., T. Yemane, G. WoldeGabriel, J.L. Aronson and R.C. Walter (1993), Late Eocene–Recent volcanism and faulting in the southern main Ethiopian ift, *J. Geol. Soc. London*, 150 (1993), pp. 99–108.

Efron, B. and R. Tibshirani (1986). [Bootstrap Methods for Standard Errors, Confidence Intervals, and Other Measures of Statistical Accuracy]: Rejoinder. *Statist. Sci.*, Volume 1, Number 1, 77-77.

EIGS, Ethiopian Institute of Geological Surveys, Ministry of Mines and Energy, (1985). *Geological Map of the DireDawa Sheet* (NC37-12), scale 1:250,000.

Engelmark, F. (2002). Using converted waves to image reservoirs with low-impedance contrast. TLE, Vol. 21, June, 600-602.

Farmer, G.L., F. V. Perry, S. Semken, B. Crow, D. Curtis, and D. J. DePaolo 1989). Isotopic evidence on the structure and origin of subcontinetal lithospheric mantle in southern Nevada. *Journal of Geophysical Research*, v. 94, p. 7885-7898.

Gao, S. S., K. H. Liu, and C. Chen (2004). Significant crustal thinning beneath the Baikal rift zone: New constraints from receiver function analysis, *Geophysical Research Letters*, 31, L20610, doi:10.1029/2004GL020813.

Gao, S. S., P. G. Silver, K. H. Liu, and Kaapvaal Seismic Group (2002). Mantle discontinuities beneath Southern Africa, *Geophys. Res. Lett.*, 29(10), 1491, doi:10.1029/2001GL013834.

Gass, I.G. and Gibson, I.L. (1969). Structural evolution of the rift zones in the Middle East. *Nature*, 221, 926-930.

George, R. (1997). Thermal and tectonic controls on magmatism in the Ethiopian province, *Ph.D. thesis*, Open University.

George, R., N. Rogers and S. Kelley (1998). Earliest magmatism in Ethiopia: evidence for two mantle plumes in one flood basalt province, *Geology*, 26, pp. 923–926.

Gianelli, G., N. Mekuria, S. Battaglia, A. Chersicla, P. Garofalo, G. Ruggieri, M. Manganelli, Z. Gebregziabher (1998). Water–rock interaction and hydrothermal mineral equilibria in the Tendaho geothermal system. *Journal of Volcanology and Geothermal Research,* 86, 253–276.

Gibson, I. L., H. Tazieff, and J. Hepworth (1970). The Structure of Afar and the Northern Part of the Ethiopian Rift [and Discussion]. *Phil. Trans. R. Soc. Lond.* A 1970 267, 331-338. doi: 10.1098/rsta.1970.0039.

Gilbert, H. J., A. F. Sheehan, K. G. Dueker, and P. Molnar (2003). Receiver functions in the western United States, with implications for upper mantle structure and dynamics, *J. Geophys. Res.* 108, no. B5, 2229, doi 10.1029/2001JB001194.

Girdler, R. (1991). The Afro-Arabian Rift system: an overview. *Tectonophysics* 197, 139–153.

Gouin, P (1970). Seismic and gravity data from Afar in relation to surrounding areas. *Phil. Trans. Roy. Soc. Lond*. A. 267, 339-358.

Green, D. H. & T. J. Falloon (1998). Pyrolite: A Ringwood concept and its current expression. In: Jackson, I. (ed.) The Earth's Mantle: Composition, Structure and Evolution. Cambridge: *Cambridge University Press*, pp. 311-380.

Gresta, S., D. Patane, A. Daniel, L. Zan, A. Carletti, O. Befekadu (1997). Seismological evidence of active faulting in the Tendaho Rift (Afar Triangle, Ethiopia). *Pure Appl. Geophys*. 149, 357–374.

Greterner, P. (2003). Summary of the Poisson's Ratio Debate 1990-2003. CSEG Recorder, September, 2003.

Güralp Systems Limited (2009). CMG-3T, Triaxial Broadband Seismometer, Operator's guide. Güralp Systems Limited, 3 Midas House, Calleva Park, Aldermaston RG7 8EA, England. Issue N 2009-07-06

Hansen, S.E., A.A. Nyblade, J. Julia (2009). Estimates of crustal and lithospheric thickness in sub-Saharan Africa from S-wave receiver functions. *South African Journal of Geology*. 2009 . v. 112, pp. 229-240.

Hayward, N.J., C.J. Ebinger (1996). Variations in the along-axis segmentation of the Afar rift system. *Tectonics* 15, 244–257.

Hofmann, C., V. Courtillot, G. Feraud, P. Rouchett, G. Yirgu, E. Ketefo, and R. Pik (1997). Timing of the Ethiopian flood basalt event and implications for plume birth and global change. *Nature* 389, 838–841.

Holbrook, W. S., W. D. Mooney, and N. I. Christensen (1992). The seismic velocity structure of the deep continental crust, in Continental Lower Crust, edited by D. M. Fountain, R. Arculus, and R. W. Kay. pp. 1-44, *Elsevier*, New York.

Kazmin, V.G., A.F. Byakov (2000). Magmatism and crustal accretion in continental rifts. *Journal of African Earth Sciences* 30, 555–568.

Kearey, P., K. A. Klepeis, and F. J. Vine (2009). Global Tectonics - 3rd ed. ISBN: 978-1-4051-0777-8.

Keary, P. and F. Vine (1996). Global Tectonics, *Blackwell Science*.

Keir, D., I. D. Bastow, K. A. Whaler, E. Daly, D. G. Cornwell, and S. Hautot (2009a), Lower crustal earthquakes near the Ethiopian rift induced by magmatic processes, *Geochem. Geophys. Geosyst.*, 10, Q0AB02, doi:10.1029/2009GC002382.

Keir, D., C. J. Ebinger, G.W. Stuart, E. Daly, A. Ayele (2006). Strain accommodation by magmatism and faulting as rifting proceeds to breakup: seismicity of the northern Ethiopian rift. *J. Geophys. Res.*, 111 (B5), B05314. doi:10.1029/2005JB003748.

Kennett, B. L. N., and E. R. Engdahl (1991), Traveltimes for global earthquake location and phase identification, *Geophys. J. Int.*, 105, 429-465.

Keranen, K. and S.L. Klemperer (2008). Discontinuous and diachronous evolution of the Main Ethiopian Rift: Implications for development of continental rifts. *Earth and Planetary Science Letters,* Volume 265, Issues 1-2, 15 January 2008, Pages 96-111.

Kerrich, R. and and A. Polat. (2006). Archean greenstone-tonalite duality: Thermochemical mantle convection models or plate tectonics in the early Earth global dynamics? *Tectonophysics*. Volume 415, Issues 1-4, 27 March 2006, Pages 141-165.

Kidane, T., V. Courtillot, I. Manighetti, L. Audin, P. Lahitte, X. Quidelleur, P.Y. Gillot, Y. Gallet, J. Carlut , T. and Haile (2003). New paleomagnetic and geochronologic results from Ethiopian Afar: Block rotations linked to rift overlap and propagation and determination of a ~2 Ma reference pole for stable Africa: *Journal of Geophysical Research*, v. 108, p. 2102, doi: 10.1029/2001JB000645.

Klemperer, S.L., T.A. Hauge, E.C. Hauser, J.E. Oliver, and C.J. Potter (1986). The Moho in the northern Basin and Range province, Nevada along the 40°N seismic-reflection transect. *Geological Society of American Bulletin*, v. 97, p. 603-618.

Knox, K. P. (1999). Upper mantle seismic velocity structure of the Afar region, MSc thesis, *Penn State University*, PA.

Kusky, T. (2005). Encyclopedia of Earth Science. *Library of Congress Cataloging-in-Publication Data*. ISBN 0-8160-4973-4.

Lachenbruch, A. H., J. H. Sass, and S. P. Galanis, Jr. (1978). New heat flow results from southern California (abstract), Eos Trans. AGU, 59, 1051.

Lahitte, P., P.Y, Gillot, T. Kidane, V. Courtilllot, and B. Abebe (2003b). New age constraints on the timing of volcanism in central Afar, in the presence of propagating rifts: *Journal of Geophysical Research*, v. 108, p. 2123, doi: 10.1029/2001JB001689.

Langston, C. A. (1979). "Structure under Mount Rainier, Washington, inferred from teleseismic body waves." *Jour. Geophys. Res.* 84: 4749-4762.

Langston, C. A. (1977). "Corvallis, Oregon, crustal and upper mantle structure from teleseismic P and S waves." *Bull. Seism. Soc. Am*. 67: 713-724.

Laughton, A.S. (1966). The Gulf of Aden in relation to the red Sea and the Afar Depression of Ethiopia. *In: The World Rift System. Geological Survey of Canada*, Paper 66-14, 78-97.

Le Pichon, X., J. Francheteau (1978). A plate—tectonic analysis of the Red Sea—Gulf of Aden area. *Tectonophysics* 46, 369–406.

Lemma, Y., A. Hailu, M. Desissa, and U. Kalberkamp (2010). Integrated Geophysical Surveys to Characterize Tendaho Geothermal Field in North Eastern Ethiopia. *Proceedings World Geothermal Congress 2010*. Bali, Indonesia, 25-29 April 2010.

Liang-Ping, X., Z. Ju-Ming and S. Hui-wen (1985). Mathematical simulation of geotemperature and heat flow patterns. Journal of Geodynamics. Volume 4, Issues 1-4, December 1985, Pages 45-61.

Liu, K. H., S. S. Gao, Y. Gao, and J. Wu (2008). Significant seismic anisotropy beneath the southern Lhasa Terrane, Tibetan Plateau, *Geochemistry Geophysics Geosystems*, 10, Q02008 (19 pages), doi:10.1029/2008GC002227.

Liu, K. H., and S. S. Gao (2006). Mantle transition zone discontinuities beneath the Baikal rift and adjacent areas, *J. Geophys. Res.*, 111, B11301, doi:10.1029/2005JB004099.

Liu, K. H., S. S. Gao, P. G. Silver, and Y. Zhang (2003). Mantle layering across central South America, *J. Geophys. Res.*, 108(B11), 2510, doi:10.1029/2002JB002208.

Maguire, P. K. H., et al. (2006). Crustal structure of the northern Main Ethiopian rift from the EAGLE controlled-source survey: A snapshot of incipient lithospheric break-up, *Geol. Soc. Spec. Publ.*, 259, 269–292, doi:10.1144/GSL.SP.2006.259.01.21.

Makris, J., and A. Ginzburg (1987). The Afar Depression: Transition between continental rifting and sea floor spreading: *Tectonophysics*, v. 141, p. 199–214, doi: 10.1016/0040–1951(87)90186–7.

Makris. J., H. Menzel, J. Zimmermann, and P. Gouin (1975). Gravity field and crustal structure of north Ethiopia, in Pliger, A. and Rösler, A., eds., Afar depression of Ethiopia: Stuttgart, E. *Schweizerbart'sche Verlagsbuchhandlung*, p. 135-144.

Makris, J., H. Menzel, J. Zimmermann (1972). A preliminary interpretation of the gravity field of Afar, northeast Ethiopia, in Girdler, R. W., ed., East African rifts: *Tectonophysics*, v. 15, p. 31-39.

Mammo, Tilahun (2004). Mapping the Crust-Mantle Boundary Beneath Afar Depression. *Gondwana Research*, K 7, No. 3, pp. 855-861.

Manighetti, I., P. Tapponier, V. Courtillot, Y. Gallet, E. Jacques, P.Y. Gillot, (2001). Strain transfer between disconnected, propagating rifts in Afar. *Journal of Geophysical Research* 106, 13613-13665.

Mazzarini, F. (2007). Vent distribution and crustal thickness in stretched continental crust: The case of the Afar Depression (Ethiopia). *Geosphere*; June 2007; v. 3; no. 3; p. 152–162; doi: 10.1130/GES00070.1.

McCoy, F. W. and G. Heiken (2000). Volcanic Hazards and Disasters in Human Antiquity. *Published by the Geological Socity of America, Inc.* ISBN: 0-8137-2345-0.

McKenzie, D. P. and W. J. Morgan (1969). Evolution of triple junctions, *Nature* 224, pp. 125–133.

Mickus, Kevin (2011). Written communication. Missouri State University, Springfield, MO.

Mohr, P.A. (1972). Surface structure and plate tectonics of Afar. *Tectonophysics* 15, 3-18.

Moores, E. M. (1998). Ophiolites, the Sierra Nevada, "Cordilleria", and orogeny along the Pacific and Caribbean margins of North and South America: *International Geology Review*, v. 40, p. 40-54.

Morgan, P. (1983). Constraints on rift thermal processes from heat flow and uplift. Tectonophysics. Volume 94, Issues 1-4.

Nair, K. S., S. S. Gao, K. H. Liu, and P. G. Silver (2006). Southern African crustal evolution and composition from receiver function studies, *Journal of geophysical research*, 111, B02304, doi:10.1029/2005JB003802.

Nakamura, Y., and B. F. Howell, Jr. (1968). Maine seismic experiment: Frequency spectra of refracted arrivals and the nature of the Mohorovicic discontinuity, *Bull. Seismol. Soc. Am.*, 54, 9-18.

Niazi, M. (1968). Crustal thickness in the Central Saudi Arabian Peninsula *Geophys. J. R. astron. Soc*. 15, 545-547.

Owens, T. J., G. Zandt, et al. (1984). "Seismic evidence for an ancient rift beneath the Cumberland Plateau, Tennessee; a detailed analysis of broadband teleseismic P waveforms." *Journal of Geophysical Research*. B. 89(9): 7783-7795.

Padovani, E. And J. Carter (1977). Aspects of the deep crustal evolution beneath south central Mexico. In The Earth's Crust (ed. J. G. Heacock). *American Geophysical Union*, Washington, DC, pp. 19-55.

Paul, A., D. Hatzfeld, A. Kaviani, M. Tatar, and C. Pequegnat (2010). Seismic imaging of the lithospheric structure of the Zagros mountain belt (Iran). *Geological Society of London*, Special Publications, 330, 5-18.

Percival, J.A., J.K. Mortensen, R.A. Stern, K.D. Card, N.J. Bégin (1992). Giant granulite terrenes of northeastern Superior Province—the Ashuanipi complex and Minto Block. Can*. J. Earth Sci.* 29, 2287–2308.

Phinney, R. A. (1964). Structure of the Earth's crust from spectral behavior of long-period body waves, *J. Geophys. Res.* 69, no. 14, 2997–3017.

Pilger, A. and A. Rösler (1976). Afar Depression of Ethiopia. Stuttgart: E. Schweizerbart'sche Verlagsbuchhandlung, *Science Publishers*.

Poorta, J. and O. Polyansky (2002). Heat transport by groundwater flow during the Baikal rift evolution. Tectonophysics. Volume 351, Issues 1-2, 28 June 2002, Pages 75-89.

Press, W. H., S. A. Teukolsky, W. T. Vetterling, and B. P. Flannery (1992). Numerical Recipes in FORTRAN, 2nd ed., *Cambridge Univ. Press*, New York.

Prodehl, C., K. Fuchs, J. Mechie (1997). Seismic-refraction studies of the Afro-Arabian Rift system—a brief review. *Tectonophysics* 278, 1–13.

Prodehl, C., and J. Mechie (1991). Crustal thinning in relationships to the evolution of the Afro-Arabian rift system—A review of seismic refraction data: Tectonophysics, v. 198, p. 311–327, doi: 10.1016/0040– 1951(91)90158-O.

George, R. M. and N.W. Rogers (2002). Plume dynamics beneath the African Plate inferred from the geochemistry of the Tertiary basalts of southern Ethiopia. *Contributions to Mineralogy and Petrology*, 144, pp. 286–304.

George, R., N. Rogers and S. Kelley (1998). Earliest magmatism in Ethiopia: evidence for two mantle plumes in one flood basalt province, *Geology*, 26, pp. 923–926.

Ramesh, D. S., R. Kind, and X. Yuan (2002). Receiver function analysis of the North American crust and upper mantle, *Geophys. J. Int.* 150, 91–108.

Redfield, T.F., W.H. Wheeler, and M. Often (2003). A kinematic model for the development of the Afar Depression and its paleogeographic implications: *Earth and Planetary Science Letters*, v. 216, p. 383–398, doi: 10.1016/S0012–821X(03)00488–6.

Roberts, D.G. (1969). Structural evolution of the rift zones in the Middle East. *Nature*, 223, 55-57.

Rooke, N. C., J.-M. Gaulier, and F. Jestin (1999). Constraints on Moho depth and crsutal thickness in the Liguro-Provencal basin from a 3D gravity inversion: geodynamic implications. Geological Society, London, Special Publications, 156, 37-61.

Rooney, T., T. Furman, G. Yirgu, and D. Ayalew (2005), Structure of the Ethiopian lithosphere: Xenolith evidence in the Main Ethiopian Rift, *Geochem. Cosmochim. Acta*, 69(15), 3889–3910, doi:10.1016/j.gca.2005.03.043.

Rouby, D., T. Souriot, J.P. Brun, P.R. Cobbod (1996). Displacements, strains, and rotations within the Afar Depression (Djibouti) from restoration in map view. *Tectonics* 15, 952–965.

Rudnick, R. L., and D. M. Fountain (1995). Nature and Composition of the Continental Crust: A Lower Crustal Perspective, *Reviews of Geophysics*, 33, 3, 267-309.

Rudnick, R.L. and I. Jackson (1995). Measured and calculated elastic wave speeds in partially equilibrated mafic granulite xenoliths: implications for the properties of an underplated lower continental crust, *Journal of Geophysical Research*, 100, 10211–10218.

Rudnick, R.L. (1992). Xenoliths-samples of the lower continental crust., In: D. M. Fountain, R. Arculus, and R. W. Kay (Editors), Continental Crust, *Elsevier*, London, 269–316.

Ruegg, J. C. (1975). Main results about the crustal and upper mantle structure of the Djibouti region (T.F.A.I), in Pilger., A., and Rösler, A., eds., Afar depression of Ethiopia: Stuttgart, E. *Schweizerbart'sche Verlagsbuchhandlung*, p. 120-134.

Ruegg, J. C., and J. C. Lepine (1973). Aperçu sur quelques études géophysiques effectuées en Afar: Rev. *Géographie Phys. et Géologies Dynam.*, v. 15, p. 414-415.

Searle, R. C. (1975). The dispersion of surface waves across southern Afar, in Afar Depression of Ethiopia, edited by A. Pilger and A. Rosler, pp. 113-120, E. *Schweizerbart*, Stuttgart, Germany.

Sengor, A.M.C. (2001). Elevation as indicator of mantle-plume activity. *Geological Society of America,* 352, 183–225.

Sengor, A.M.C. and K. Burke (1978). Relative timing of rifting and volcanism on earth and its tectonic implications. *Geophysical Research Letters* 5, 419–421.

Sheehan, A. F., G. A. Abers, C. H. Jones, and A. L. Lerner-Lam (1995). Crustal thickness variations across the Colorado Rocky Mountains from teleseismic receiver functions, *J. Geophys. Res.* 100, 20,391– 20,404.

Sheriff, R. E., and L. P. Geldart (1993). Exploration Seismology, 2nd ed., *Cambridge Univ. Press*, New York, 1993.

Sichler, B. (1980). La biellette Danakile; un modele pour levolution geodynamique de l'Afar Colloque rift dAsal. Reunion extraordinaire de la Societe Geologique de France. *Bulletin de la Societe Geologique de France* 22, 925–932.

Souriot, T., J.P Brun (1992). Faulting and block rotation in the Afar triangle, East Africa; the Danakil ''crank-arm'' model. *Geology* 20, 911–914.

Stern, R.J. (1994). Arc assembly and continental collision in the Neoproterozoic East African Orogen—implication for the consolidation of Gondwanaland. *Annual Review Earth Planetary Science* 22, 319–351.

Storey, Michael; J. J. Mahoney, A. D. Saunders, R. A. Duncan, S. P. Kelley, M. F. Coffin (1995). Timing of hot spot-related volcanism and the breakup of Madagascar and India. *Science* 267, 852−855.

Tadesse, S., J-P. Milesi, Y. and Deschamps (2003). Geology and mineral potential of Ethiopia: a note on geology and mineral map of Ethiopia: *Journal of African Earth Sciences*, 36, 273–313.

Tapponier, P., R. Armino, I. Manighetti, V. Courtillot (1990). Bookshelf faulting and horizontal block rotations between overlapping rifts in southern Afar. *Geophysical Research Letters* 17, 1-4.

Tarkov, A., and V. Vavakin (1982). Poisson's ratio behavior in various crystalline rocks: Application to the study of the Earth's interior, *Phys. Earth Planet. Inter*., 29, 24– 29.

Tefera, M., T. Chernet, W. Haro (1996). Explanation of the Geological Map of Ethiopia. *Ethiopian Institute of Geological Surveys*, Addis Ababa, vol. 3, p. 79.

Teklay, M., E. Scherer, K. Mezger, and L. Danyushevsky (2010). Geochemical characteristics and Sr–Nd–Hf isotope compositions of mantle xenoliths and host basalts from Assab, Eritrea: implications for the composition and thermal structure of the lithosphere beneath the Afar Depression. *Contrib Mineral Petrol* (2010) 159:731–751.

Tesfaye, S., M. Rowan, K. Mueller, B. Trudgill, and D. Harding (2008). Relay and accommodation zones in the Dobe and Hanle grabens, central Afar, Ethiopia and Djibouti. *Journal of the Geological Society, London*, Vol. 165, 2008, pp. 535–547. Printed in Great Britain.

Thompson, G. A., and J. McCarthy (1986). Geophysical evidence for igneous inflation of the crust in highly extended terrenes [abs.]: EOS (*American Geophysical Union Transactions*), v. 67, p. 1184.

Tiberi, C., C. Ebinger, V. Ballu, G. Stuart, and B. Oluma (2005). Inverse models of gravity data from the Red Sea–Aden–East African rifts triple junction zone: *Geophysical Journal International*, v. 163, p. 775–787, doi: 10.1111/j.1365–246X.2005.02736.x.

Varet, J. (1978). Geology of Central and Southern Afar (Ethiopia and Djibouti Republic) *F. Gasse for Chapter IV on Sedimentary Formation*. Eds. CNRS, France, Paris, p. 118.

Vellutini, P. (1990). The Manda-Inakir Rift, Republic of Djibouti: a comparison with the Asal Rift and its geodynamic interpretation. *Tectonophysics* 172, 141–153.

Vinnik, L. (1977). Detection of waves converted from P to SV in the mantle, *Phys. Earth Planet. Inter*., 15, 39–45.

Watanabe, T. (1993). Effectsa of water and melt on seismic velocities and their applications to characterization of seismic reflectors. *Geophys. Res. Lett.* 20 24, pp. 2933–2936.

Wilson, D. and R. Aster (2005). Seismic imaging of the crust and upper mantle using regularized joint receiver functions, frequency–wave number filtering, and multimode Kirchhoff migration. *Journal of Geophysical Research*, v. 110, B05305, doi:10.1029/2004JB003430.

Wilson, D., R. Aster, J. Ni, J., S. Grand, M. West, W. Gao, W. Baldridge, and S. Semken (2005). Imaging the seismic structure of the crust and upper mantle beneath the Great Plains, Rio Grande Rift, and Colorado Plateau using receiver functions, *J. Geophys. Res.* 110**,** B05306, doi 10.1029/2004JB003492.

Windley, B. F. (1995). The Evolving Continents. 3rd edition, New York, *Wiley*, 526 p.

Woldegabriel, G., J. L. Aronson, and R. C. Walter. (1990). Geology, geochronology, and rift basin development in the central sector of the Main Ethiopia Rift. *Geological Society of America Bulletin*, v. 102, p. 439-458.

Woldetinsae, G., and H.-J Gotze (2005). Gravity field and isostatic state of Ethiopia and its adjacent areas: *Journal of African Earth Sciences*, v. 41, p. 103–117, doi: 10.1016/j.jafrearsci.2005.02.004.

Wolfenden, E., C. Ebinger, G. Yirgu, P. R. Renne, and S. P. Kelley (2005). Evolution of a volcanic rifted margin; southern Red Sea, Ethiopia, *Geological Society of America Bulletin*, 117, 7 – 8, 846– 864.

Wolfenden, E., C. Ebinger, G. Yirgu, A. Deino, D. Ayalew (2004). Evolution of the northern Main Ethiopian rift: Birth of a triple junction. *Earth and Planetary Science Letters*, v. 224, 213 – 228.

Yuan, X., G. Asch, K. Bataille, G. Rock, M. Bohm, H. Echtler, R. Kind, O. Oncken, and I. Wolbern (2002). Deep seismic images of the Southern Andes, in Kay, S.M., and Ramous, V.A., eds., Evolution of an Andean margin: A tectonic and magmatic view from the Andes to the Neuquén Basin (35-39 S lat): Geological Society of America Special Paper 407, p. 61-72, doi: 10.1130/2006.2407(03).

Zandt, G., H. Gilbert, T. J. Owens, M. Ducea, J. Saleeby, and C.H. Jones, C.H. (2004). Active foundering of a continental arc root beneath the southern Sierra Nevada in California. *Nature* 431, 41-46.

Zhu, L. P. And H. Kanamori (2000). Moho depth variation in southern California from teleseismic receiver functions, *J. Geophys. Res.*, 105, 2969– 2980.

VITA

Sattam Abdulkareem Almadani, was born on May 23, 1977 in Taif, located in western Saudi Arabia. He received his BS degree in marine physics from King Abdulaziz University (KAU) in Jeddah in 1999. He completed his MS in marine physics at KAU in 2003. He worked as an HR administrator for Unilever for almost three years, and then moved to Siemens and where he worked as a recruiter specialist for eight months. In 2007, Sattam joined Missouri University of Science and Technology to pursue his PhD degree in geology and geophysics. His research interests involve studying crustal structure and composition using receiver functions analysis.